Module-level Health Monitoring of Solar PV Plants using LoRa Wireless Sensor Networks

by

Joseph E. Shuda

Thesis presented in partial fulfilment of the requirements for the degree of Master of Engineering (E&E) in the Faculty of Engineering at Stellenbosch University

Supervisor: Dr. Arnold J. Rix
Co-supervisor: Prof. Marthinus. J. Booysen

April 2019

Stellenbosch University https://scholar.sun.ac.za

Declaration

I have read and understand the Stellenbosch University Policy on Plagiarism and the definitions of plagiarism and self-plagiarism contained in the Policy [Plagiarism: The use of the ideas or material of others without acknowledgement, or the re-use of one's own previously evaluated or published material without acknowledgement or indication thereof (self-plagiarism or textrecycling)].

I also understand that direct translations are plagiarism, unless accompanied by an appropriate acknowledgement of the source. I also know that verbatim copy that has not been explicitly indicated as such, is plagiarism.

I know that plagiarism is a punishable offence and may be referred to the University's Central Disciplinary Committee (CDC) who has the authority to expel me for such an offence.

I know that plagiarism is harmful for the academic environment and that it has a negative impact on any profession.

Accordingly all quotations and contributions from any source whatsoever (including the internet) have been cited fully (acknowledged); further, all verbatim copies have been expressly indicated as such (e.g. through quotation marks) and the sources are cited fully.

I declare that, except where a source has been cited, the work contained in this assignment is my own work and that I have not previously (in its entirety or in part) submitted it for grading in this module/assignment or another module/assignment.

April 2019

Signature
Joseph Eduan Shuda

Date

Stellenbosch University https://scholar.sun.ac.za

Abstract

Module-level Health Monitoring of Solar PV Plants using LoRa Wireless Sensor Networks

J. E. Shuda

Department of Electrical and Electronic Engineering,
University of Stellenbosch,
Private Bag X1, Matieland 7602, South Africa.

Thesis: MEng (E&E)

April 2019

The monitoring of PV plants is a crucial aspect in ensuring smooth operation and optimum efficiency. Early detection of faults or inefficiencies can greatly reduce downtime and increase overall plant efficiency. Faults include temporary and permanent soiling, shadowing, anomalous ageing and critical electrical or mechanical faults. Many solar installations are located at remote locations; faults often go unnoticed and unattended to for long periods. A remote module-level monitoring system can detect inefficiencies and faults when and where they occur.

A wireless module-level monitoring system that measures electrical and environmental quantities related to PV module performance is proposed in this work. Although various wireless module-level sensor approaches exist, the sheer size of a typical solar PV plant presents challenges for the wireless technologies presented in these approaches. Different wireless technologies such as Bluetooth, Zigbee, Wi-Fi, GSM, Sigfox and LoRa were evaluated for the proposed monitoring system. LoRa was chosen as the wireless technology due to its long range and low power consumption.

A number of sensor nodes and a gateway was designed, built and tested. Each sensor node is capable of measuring voltage, current, irradiance, ambient temperature, module temperature, orientation and tampering detection. Initial field tests that were carried out indicate that the sensor nodes measure with adequate accuracy to evaluate PV module performance in detail. The developed monitoring system consisting of fifteen sensor nodes, a gateway and a remote GUI application was tested on a operational PV plant. Shading and soiling field scenarios, as well as a shading experiment proved that the module-level monitoring system is capable of detecting faults and inefficiencies within a PV plant.

Results that were obtained indicate the following: sensor nodes are modular, self-powered and low maintenance. The wireless technology used to transmit measurement data from the sensor nodes to a central gateway is capable of operating on a small, medium or large PV plant. The monitoring system is also capable of remote detection and reporting via the GUI application.

Stellenbosch University https://scholar.sun.ac.za

Uittreksel

Module-vlak Gesondheid Monitering van Fotovoltaïese Son Aanlegte deur gebruik te maak van LoRa Draadlose Sensor Netwerke

("Module-level Health Monitoring of Solar PV Plants using LoRa Wireless Sensor Networks")

J. E. Shuda

Departement Eletriese en Elektroniese Ingenieurswese,
Universiteit van Stellenbosch,
Privaatsak X1, Matieland 7602, Suid Afrika.

Tesis: MIng (E&E)

April 2019

Die monitering van FV (Fotovoltaïese)-eenhede of modules is noodsaaklik vir die instandhouding en optimale funksie daarvan, veral waar daar verskeie modules in 'n afgeleë aanleg gekoppel is. Vroeë opsporing van foute en probleme dra by tot die optimale funksionering van 'n FV aanleg, en is belangrik om aftyd te beperk. Probleemareas sluit in: tydelike en permanente besoedeling van die oppervlakte van die module, ongewensde skadu blootstelling, abnormale veroudering van panele, sowel as kritieke elektriese of meganiese foute. Daar is deesdae meer en meer van hierdie aanlêe wat in afgeleë gebiede opgerig word, 'n toedrag van sake wat beteken dat foute en probleme dikwels vir lang periodes van tyd onopgemerk en verwaarloos bly. 'n Afstandsmoniteringsmodule (AMM) sal in sulke gevalle wenslik wees om probleme en foute op te spoor en tyd-effektiewe instandhouding toe te laat.

Hierdie studie en tesis stel 'n draadlose (radio-afhanklike), veeldoelige moniteringsisteem wat elektriese en omgewingsfaktore ontleed, voor. Die doel hiervan is om die optimale funksie van sulke panele en groeperings van panele te verseker. Alhoewel daar reeds sulke moniteringsisteme bestaan, is daar bepaalde uitdagings en praktiese probleemareas vir radio-afhanklike monitering betrokke - veral by groter aanlêe. In hierdie studie is verskillende radio-afhanklike tegnologieë ondersoek en evalueer vir die AMM: oa Bluetooth, Zigbee, Wi-Fi,GSM, Sigfox, en LoRa. LoRa was uiteindelik gekies as gevolg van die effektiwiteit oor langer afstande, asook die lae kragverbruik.

Verskeie sensor-modules asook 'n toegangspoort (portaal) is ontwerp, gebou en getoets. Die sensors was almal in staat om die volgende te meet: potensiaalverskil (volt), stroom, straling (sonskerpte), omgewingstemperatuur, module-temperatuur, oriëntasie en versteuring agv meganiese of kriminele faktore. Gedurende die beginfase was praktiese toetsing daarop gerig om vas te stel dat die modules voldoende akkurate data genereer, om sodoende die funksie van FV-eenhede deeglik en in detail te ontleed. Uiteindelik is 'n AMM ontwerp, gebou en getoets wat uit 15 sensor nodes, 'n toegangspoort en 'n afgeleë Grafiese Gebrui-

Stellenbosch University https://scholar.sun.ac.za

kerskoppelvlak bestaan het. Die modules is in 'n bestaande, werkende FV-aanleg ontplooi. Hier is ongewensde skaduwee-gevalle asook besoedeling van die FV-eenhede ondersoek, terwyl verdere skaduwee-situasies eksperimenteel toegepas is. Die inligting uit hierdie scenario's verkry, het bewys dat die AMM effektief en akkuraat probleemareas en foute uitwys.

Resultate uit hierdie studie bewys die volgende: die ontwerpte en geboude sensor nodes is nie net modulêr nie, maar vereis min instandhouding en gebruik ook min krag. Die radiotegnologie wat gebruik was om data van die sensor-modules na die toegangspoort te stuur, is geskik om diens te doen in klein-, medium- en groot FV-aanlêe. Die moniteringsisteem is dus effektief om afstandsmonitering te doen en hierdie data via 'n toegangsportaal na 'n Grafiese Koppelvlak te stuur, vanwaar die nodige instandhouding dan geïnisieer kan word.

Stellenbosch University https://scholar.sun.ac.za

Acknowledgements

I would like to thank the following people and organizations for their invaluable support over the past two years:

- My supervisor and co-supervisor, Dr AJ Rix and Prof MJ Booysen for their leadership, guidance and assistance throughout the course of the research. Thank you for providing me with the opportunity to conduct the research.
- For the financial assistance of Scatec Solar towards this research.
- My parents, Annemie and Kennith who supported me until the end and gave me the encouragement to carry on and to always stay positive.
- The entire Media Lab, it was great sharing the lab with you, thank you for all your laughter, friendships and continuous support.
- Mr Johan Arendse for providing a helping hand in the soldering of PCBs.
- Mr Wynand van Eeden for assisting me with creating CNC PCBs.
- Mr Wessel Croukamp for assisting me in assembling various sensor nodes.
- The Department of Electrical and Electronic Engineering for providing me with the necessary skills to conduct my research.
- My friends and family for their encouragement and emotional support.

Stellenbosch University https://scholar.sun.ac.za

Contents

Stellenbosch University https://scholar.sun.ac.za

Stellenbosch University https://scholar.sun.ac.za

Stellenbosch University https://scholar.sun.ac.za

List of Figures

Stellenbosch University https://scholar.sun.ac.za

Stellenbosch University https://scholar.sun.ac.za

Stellenbosch University https://scholar.sun.ac.za

Stellenbosch University https://scholar.sun.ac.za

List of Tables

Stellenbosch University https://scholar.sun.ac.za

Nomenclature

Symbols and Variables

γ	Wavelength	[m]
f	Frequency	[Hz]
c	Speed of Light	[m/s]
Gtx	Transmitter Antenna Gain	[dB]
Grx	Receiver Antenna Gain	[dB]
η	Efficiency	[%]
G	Irradiance	[W/m^2]
A_C	Collector Area	[m^2]
α_{MP}	Maximum Power Temperature Coefficient	[%/°C]
P_{MP}	Maximum Power Output at STC	[W]

Subscripts

N	Number of items
tx	Transmitter
rx	Receiver
STC	Standard Test Conditions
MP	Maximum Power
th	Threshold

Abbreviations

PV	Photovoltaic
SEIA	Solar Energy Industries Association
O&M	Operation and Maintenance
UV	Ultra Violet
EMC	Electromagnetic Compatibility

Stellenbosch University https://scholar.sun.ac.za

NTC Negative Temperature Coefficient

GUI Graphical User Interface

WSN Wireless Sensor Network

PLC Power-Line Communication

ADC Analog-to-Digital Converter

IC Integrated Circuit

LDR Light Dependent Resistor

TOA Time On Air

FSPL Free Space Path Loss

PR Public Relations

BLE Bluetooth Low Energy

ISM Industrial, Scientific and Medical

MNO Mobile Network Operator

LPWAN Low-Power Wide-Area Network

UNB Ultra Narrow Band

BPSK Binary Phase Shift Keying

FSK Frequency Shift Keying

SNR Signal-to-Noise-Ratio

STC Standard Test Conditions

PCB Printed Circuit Board

I/O Input/Output

LDO Low Drop Out

GHI Global Horizontal Irradiance

POA Plane of Array

SMPS Switch Mode Power Supply

PLA Poly-Lactic Acid

SBC Single Board Computer

GPIO General Purpose Input Output

CRC Cyclic Redundancy Check

CSV Comma Separated Values

MPPT Maximum Power Point Tracker

Stellenbosch University https://scholar.sun.ac.za

Chapter 1

Introduction

One of the challenges in the twenty-first century is providing energy to humanity in a safe, clean and sustainable way. PV (Photovoltaic) sources are currently one of the industry's leading solutions because of their high energy density, supply security and sustainability. In the last decade, solar PV installations in the United States has experienced a compound annual growth rate of more than 60% and a drop in cost of more than 60% according to the SEIA (Solar Energy Industries Association) [1] as presented in Figure 1.1.

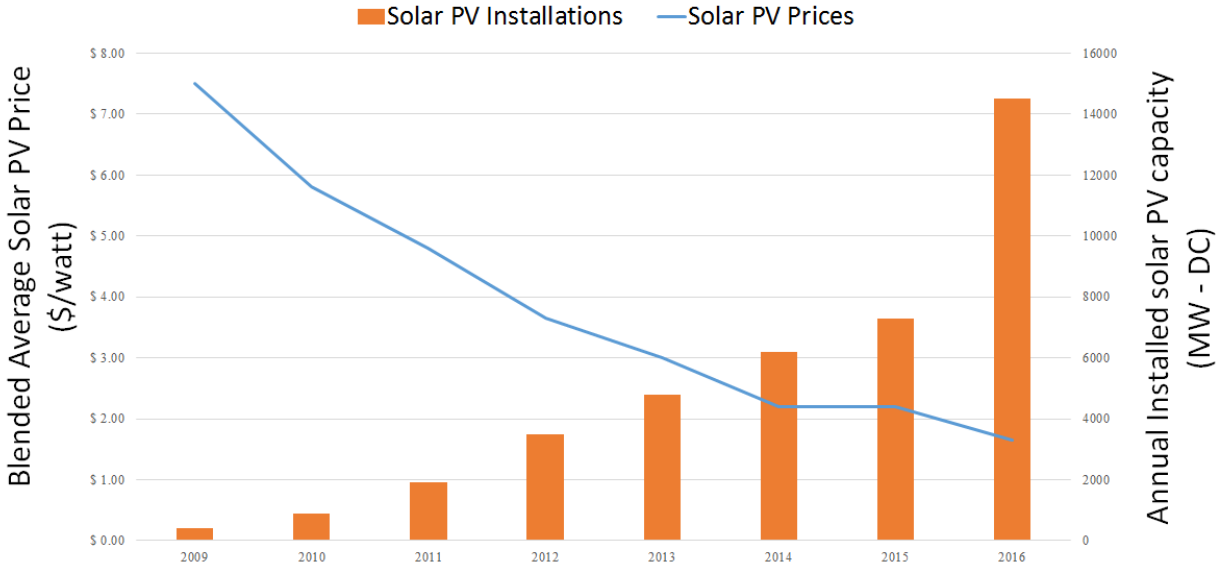

Figure 1.1: Annual Solar PV Installations and Blended Average PV Prices from 2009 to 2016 in the United States adapted from [1].

Optimisation of solar resources is a fundamental aspect in ensuring optimal performance of solar resources. Optimisation in the Solar PV field with regards to larger solar installations include accurate initial sizing of solar panel arrays. This step is done by design engineers when solar installations are planned. A second and important optimisation is to ensure continuous performance of solar panels throughout their lifetime. This entails ensuring that solar modules perform at their maximum efficiency and to quickly and effectively detect any signs that solar modules are not performing at an optimum level.

Stellenbosch University https://scholar.sun.ac.za

1.1 Problem Statement

Many solar PV installations are located at remote locations. When faults occur within an array the faults often go unnoticed and unattended to for long periods. When technicians are eventually sent to rectify the faults, they have to spend a lot of time to determine the location of the faults manually. A remote monitoring system that measures at a module or string level can detect inefficiencies and faults right when they occur and it can give better insights as to where the fault occurred.

Faults that occur on PV modules include shadowing, dust collection, mismatches, anomalous ageing and other electrical faults or deterioration. Detecting these faults is crucial in ensuring that a PV plant performs at its optimal level. Detecting and locating critical faults quickly is important in ensuring minimum downtime.

One of the biggest concerns in creating a viable remote monitoring system for PV installations is the sheer size of most PV installations. The cost of installing a monitoring system with individual sensors that are wired to one another would be expensive due to the high cost of cables and the installation costs associated with the cables. Existing module level monitoring systems are either wired sensors or the sensors are limited on the communication range that can be achieved from the sensor to the home base.

There is a need for a long range wireless module-level monitoring system that measures electrical and environmental quantities related to PV module performance. Such a system can detect and locate faults and inefficiencies within a PV plant which ultimately optimises performance and reduces downtime. The location of faults also reduces O&M (Operation and Maintenance) costs by cutting down on time to locate a specific fault or inefficiency.

1.2 Research Objectives

The objectives that were set out to guide the research towards the deliverables necessary to address the problem statement are as follows:

1. Measurement: To develop a sensor that can measure electrical and environmental properties of a PV module that relates to module performance.
2. Data Collection: To develop a system that can collect and store measurement data from the requisite sensors.
3. Modelling: To develop a model that uses measured electrical and environmental data to detect inefficiencies and faults within a solar installation.
4. Data Visualization: To develop a tool for analysing and visualizing measurement data.
5. Remote Detection and Reporting: To develop the system in such a manner that performance data and faults can be viewed and are reported remotely.

1.3 Scope And Limitations

The system in question is merely a proof of concept. The scope of this study is restricted to the following:

- The system is designed in the context of South African conditions with the focus on areas that are feasible for solar PV installations (Sunny Regions)

Stellenbosch University https://scholar.sun.ac.za

- Waterproofing and UV (Ultra Violet) resistance of the sensor enclosure are not in the scope of this project although a waterproof enclosure was used for the developed sensors.
- Lighting protection of PV modules and the sensors that attach to the modules are not in the scope of this project.
- The influence and effect of EMC (Electromagnetic Compatibility) that is generated by inverters located on PV installations are not in the scope of this project.
- Different temperature measurement techniques and methods as well as mounting methods and the influence of these methods when measuring module backside temperature are not in the scope of this project.

1.4 Thesis Contribution

The contribution made by this thesis can be subdivided into multiple novel contributions. These contributions support the development of a module-level health monitoring system for PV plants using wireless sensor networks. The monitoring system consists of three main sub-systems: module level sensor nodes and a gateway, a database located on a cloud server and a GUI application. The sensor nodes measure module level electrical and environmental quantities that are required to evaluate module performance. These quantities include: voltage, current, ambient temperature, module backside temperature, irradiance and orientation. Measurement data is sent to a centrally located gateway via a long range, low power wireless communication network called LoRa. The gateway stores measurement data in a database located on a cloud server. A GUI application extracts measurement data, calculates certain quantities related to PV performance from the data and displays certain parameters such as health status, instantaneous power and historical data among other things. The GUI application can be operated from any PC with an Internet connection and displays 'live' plant data.

1.5 Thesis Structure

The thesis is structured as follows:

- **Chapter 2** presents a literature review that analyses and evaluates research-based and commercially available module level monitoring systems. The objectives, methods, results and shortages of these monitoring systems are discussed. Secondly material, methods and tools required to develop a module level remote monitoring system are discussed. This is divided into two main categories. The first category looks into theories and methods used for the physical measurement of electrical and environmental performance characteristics of a PV module. The second category investigates the transportation layer of the measured data. In this category wireless communication as a transport medium for measured data is assessed.
- **Chapter 3** describes the system design as well as the model used to determine efficiency and detect faults. Visual representations in the form of block diagrams that represent the system with all of its subcomponents and how these subcomponents interact with one another are also presented.

Stellenbosch University https://scholar.sun.ac.za

- **Chapter 4** presents the hardware design of three different sensor versions and a gateway. The different measurement techniques and components that make up each version are discussed. The design of various circuitry that make up the sensor nodes together with measurement results are also presented.
- **Chapter 5** describes the software implementation of each sensor unit as well as the entire system. How data is collected, sent , retrieved and stored are presented along with tools used to analyse and visualize the data.
- **Chapter 6** details results that were obtained from the monitoring system. These results include electrical and environmental measurement data, processed data and certain trends that were captured by analysing different data sets.
- **Chapter 7** concludes the study by evaluating the objectives that were set out in Section 1.2. A critical evaluation of how the system met the various requirements is presented along with various problems that were encountered. Finally recommendations for future work regarding module level monitoring systems are presented based on conclusions that were drawn from the tests and results in Chapter 6.

Stellenbosch University https://scholar.sun.ac.za

Chapter 2

Theoretical Overview and Background Study

2.1 Chapter overview

In this chapter a literature review that analyses and evaluates research-based and commercially available module level monitoring systems are presented. The objectives, methods, results and shortages of these monitoring systems are discussed. Material, methods and tools required to develop a module level remote monitoring system are also presented. Theories and methods used for the physical measurement of electrical and environmental performance characteristics of a PV module as well as the transportation layer to send and receive measurement data are analysed.

2.2 Research-Based Module Level Monitoring Systems

There have been several research-based approaches to develop sensors that measure individual PV modules. Four cases are presented and evaluated in this section. Three commercially available module level monitoring systems are presented and evaluated in Section 2.3. A summary of the key factors for each of the module level monitoring systems is presented in Table 2.1 on Page 15.

Case 1: In [2] Ranhotigamage et al. propose a low-cost WSN (Wireless Sensor Network) that monitored individual PV modules. The main objective was to build a low cost system intended for domestic purposes, that measures the maximum power point of PV modules along with other performance parameters.

The system proposed in [2] consisted of a voltage sensor, a current sensor, an irradiance sensor, an ambient temperature sensor and a electronically controllable load. The sensors in [2] are controlled by a microcontroller and the measurement data was sent to a coordinator using Zigbee communication. In [2] four wireless sensor nodes were built and tested.

Voltage measurements are conducted with voltage divider arrangements to bring the input voltage to a measurable voltage that falls within the microcontroller analog input voltage specifications. Current in [2] is measured by means of a shunt resistor. The current produces a voltage over the shunt resistor which is amplified and then sampled by the microcontroller. Irradiance in [2] is measured by means of a photodiode. A resistor is placed in parallel with the photodiode which allows the photodiode to generate current that is linear with the amount of light that the photodiode is exposed to. The current is then converted to

Stellenbosch University https://scholar.sun.ac.za

a voltage by means of a operational amplifier after-which the voltage is sampled by the microcontroller.

Ambient temperature measurements in [2] are done with a NTC (Negative Temperature Coefficient) thermistor. The thermistor is placed in series with a resistor and a reference voltage is supplied to the thermistor. The voltage across the resistor is fed to the analog to digital converter of the microcontroller. The temperature is calculated by calculating the thermistor resistance which is then converted to a temperature reading using the Steinhart-Hart equation.

After each measurement has been made by sensors in [2] the data is sent to the coordinator which sends the data to a PC via a USB to serial cable. The data is then stored into a database and a text file. Graphs of data for different sensors can be viewed. Figure 2.1 depicts performance data that one of the sensors in [2] captured in the form of a graph.

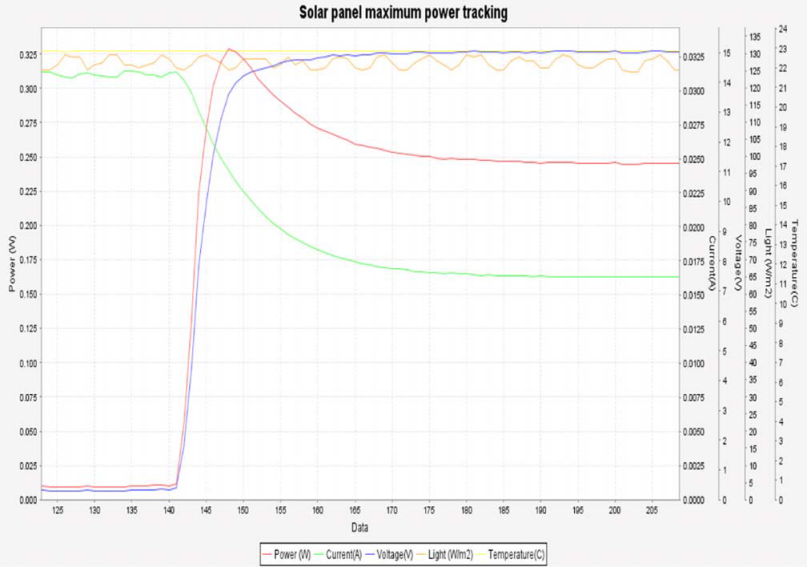

Figure 2.1: Measured characteristics of voltage, power, temperature, and light irradiance over time [2].

In [2] there is no indication of how each sensor is powered and considering the circuitry used either an external power source or the PV module itself was used to power the wireless sensors. In [2] there is no fault detection mechanism that actively monitors measurement data to detect any faults. A downside to the system proposed in [2] is that a PC is required at the coordinator to store data, there is no cloud connection for remote access or remote monitoring. Another downside to the system is that the wireless communication (Zigbee) has a limited range. A breakdown of different wireless communication technologies is presented in Section 2.5.

Case 2: Another module-level monitoring system was developed in [3] by Syafii et al. The main objective in [3] was to develop a measurement system that can provide real-time weather condition and electricity consumption information of individual PV modules within a PV plant to the users. The system developed in [3] comprises of a sensor unit and a home base. The sensor unit measures temperature, humidity, irradiance, voltage and current.

Temperature and humidity measurements in [3] are made with a DHT22 sensor. Irradiance measurements are mare made with a OPT101 photodiode. Voltage measurements are made with a simple voltage divider circuit and current is measured by a ACS712 Hall-effect sensor.

Stellenbosch University https://scholar.sun.ac.za

The system developed in [3] uses Zigbee wireless communication to send data from the sensor node to the home base. The home base consists of a receiving node that sends the measurement data via RS232 serial port communication to a PC. The PC then stores the data

The sensor node in [3] uses an Arduino Mega as microcontroller and is fitted with a DS1307 Real Time Clock to provide accurate time and date data. Results presented in [3] show that data was successfully sent from a sensor node on the 4th floor to the 2nd floor of a department building with a 3-4 second delay. Figure 2.2 illustrates voltage, current and power measurements captured over an hour. Figure 2.3 shows power measurements that were captured over the duration of three days.

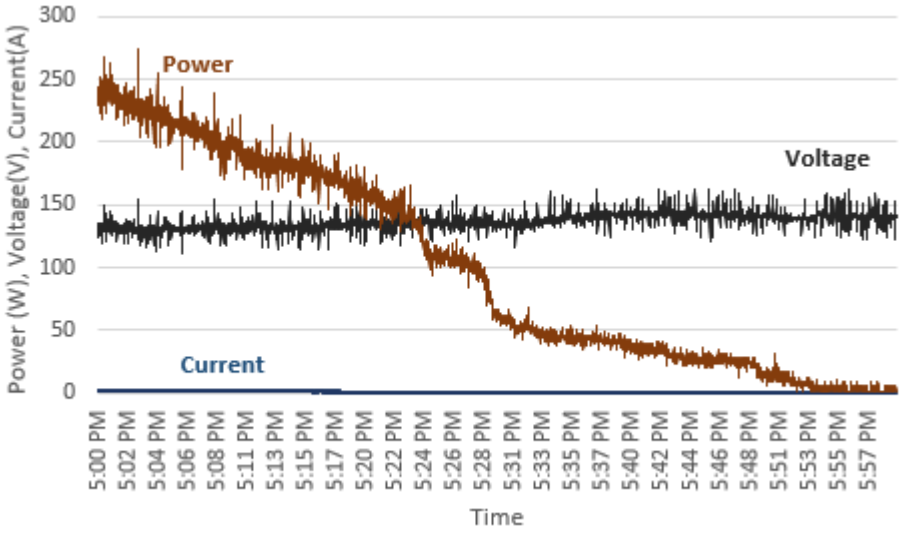

Figure 2.2: Recorded Current, Voltage and Power data of a single PV module for one hour [3].

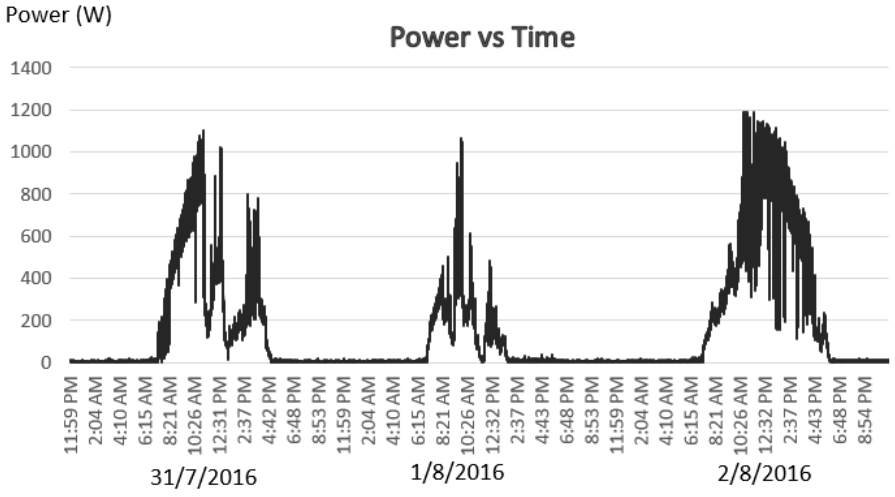

Figure 2.3: Recorded Power data of a single PV module for three consecutive days [3].

In [3] the only way that data can be viewed in real-time is by looking at incoming data that is displayed on the PC screen. There is no indication of live graphs or any form of data analysis to inform the used of any faults in the PV installation. The sensor node in [3] is

Stellenbosch University https://scholar.sun.ac.za

powered by an external power source which makes it impractical for deployment on a PV plant. The wireless communication used has a limited range and there is no indication of remote reporting capabilities by the monitoring system.

Case 3: In [4] Rashidi et al. introduced a solar PV performance monitoring system by utilizing a wireless Zigbee microcontroller. The objective of the monitoring system is to monitor the performance of an array to detect non-ideal operating conditions. The system proposed consists of a low-cost, small form factor sensor unit that is capable of measuring voltage and current for an array of PV modules. The system also consists of a back end embedded program that stores data and a front end GUI (Graphical User Interface). A block diagram of system proposed in [4] can be seen in Figure 2.4.

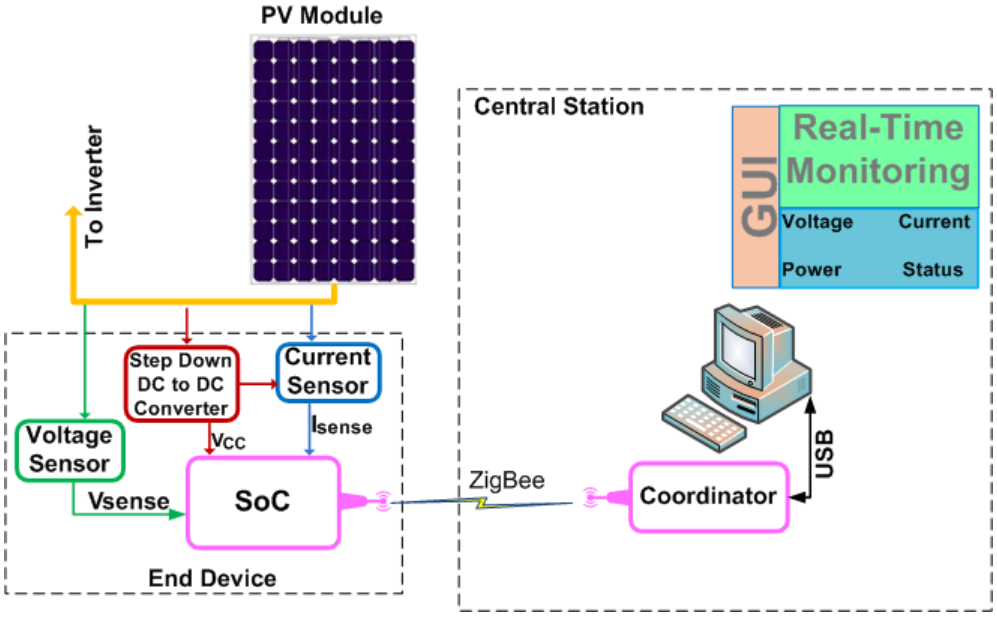

Figure 2.4: PV module performance monitoring system block diagram [4].

The sensor nodes developed in [4] are powered by the PV module that is being measured via a DC to DC converter. Current is measured by means of a shunt resistor and voltage is measured with a resistor divider circuit which is sampled by a microcontroller. The network topology used in [4] is a star topology. A coordinator and two sensor nodes were developed. The coordinator consists of a Zigbee enabled microcontroller which sends measurement data to a host computer via a USB connection. After measurement data is received the data is displayed in the form of graphs on a GUI developed in LabView. Voltage, current and power for two PV modules under partial shading can be seen in Figure 2.5.

Stellenbosch University https://scholar.sun.ac.za

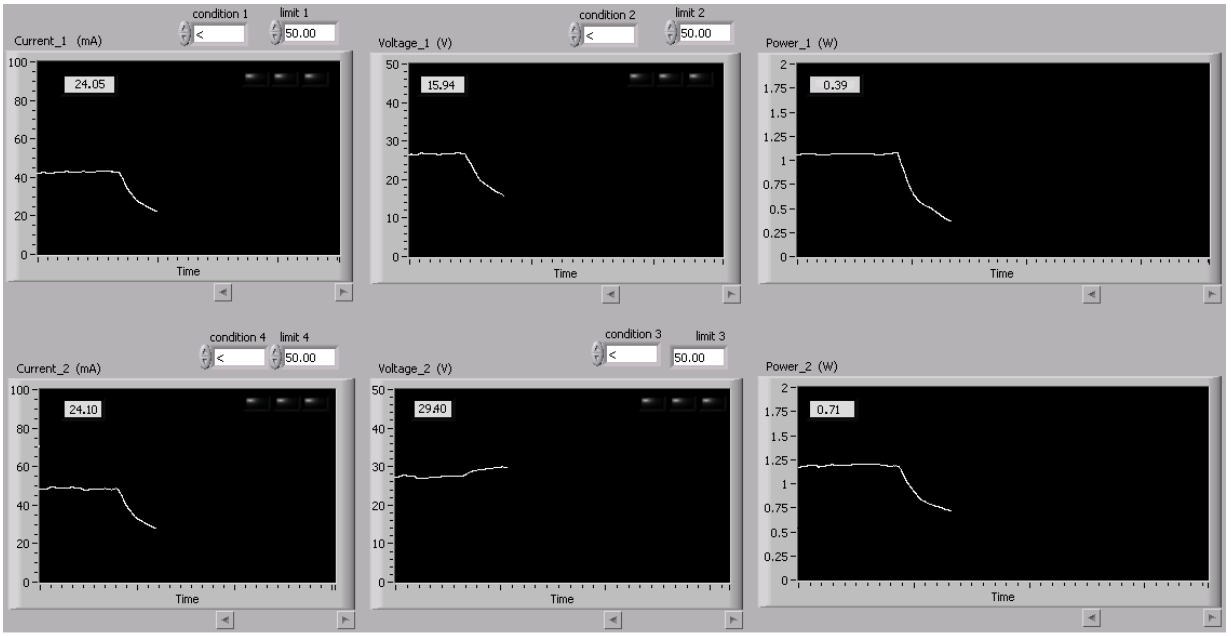

Figure 2.5: Voltage, current and power for two PV modules under partial shadow [4].

The performance monitoring system developed in [4] measures module voltage and current. No other parameters relating to module performance are measured. The system measured two individual modules and there is no proof of an entire array being measured. There is no indication of remote monitoring capabilities or any data analysing methods or tools to detect non-ideal operating conditions or faults. The sensor nodes are powered from the modules being measured making those modules less efficient and no measurement data is captured or sent when the sun is not shining. The wireless technology used has a limited range which makes it impractical for deployment on a large PV installation.

Case 4: In [5] and [6] Ando et al. developed a module-level smart monitoring system. The smart monitoring system consists of low-cost smart sensors that measure voltage, current, irradiance, temperature and inertial events. The main objective of the system is to detect the causes of efficiency losses. The system is based on a WSN with sensor nodes installed on individual PV modules.

Individual sensors send measurement data to a service centre where dedicated paradigms continuously calculate the efficiency and possible causes of efficiency losses for each PV module. The estimation of efficiency losses is based on the continuous comparison between the measured efficiency of each PV module and the nominal efficiency for the given operating conditions. The three main causes of inefficiency that the system developed in [5] and [6] tries to identify are spot and periodic shading, soiling and anomalous ageing. The methodological approach for the detection of the causes of efficiency losses for the system developed in [5] and [6] is shown in Figure 2.6.

The sensor nodes are equipped with SPV1020 DC-DC boost converters that does maximum power point tracking and provides current and voltage readings through SPI (Serial Peripheral Interface). Temperature measurements are made with a TMP36 analog temperature sensor. The temperature sensor is attached to the rear of the measured PV module to obtain the module backside (Tedlar) temperature. For irradiance measurements a low-cost photodiode was used. Each sensor node is powered by a battery that is charged by the

Stellenbosch University https://scholar.sun.ac.za

SPV1020 DC-DC converter. A schematization of the monitoring system developed in [5] and [6] is shown in Figure 2.7.

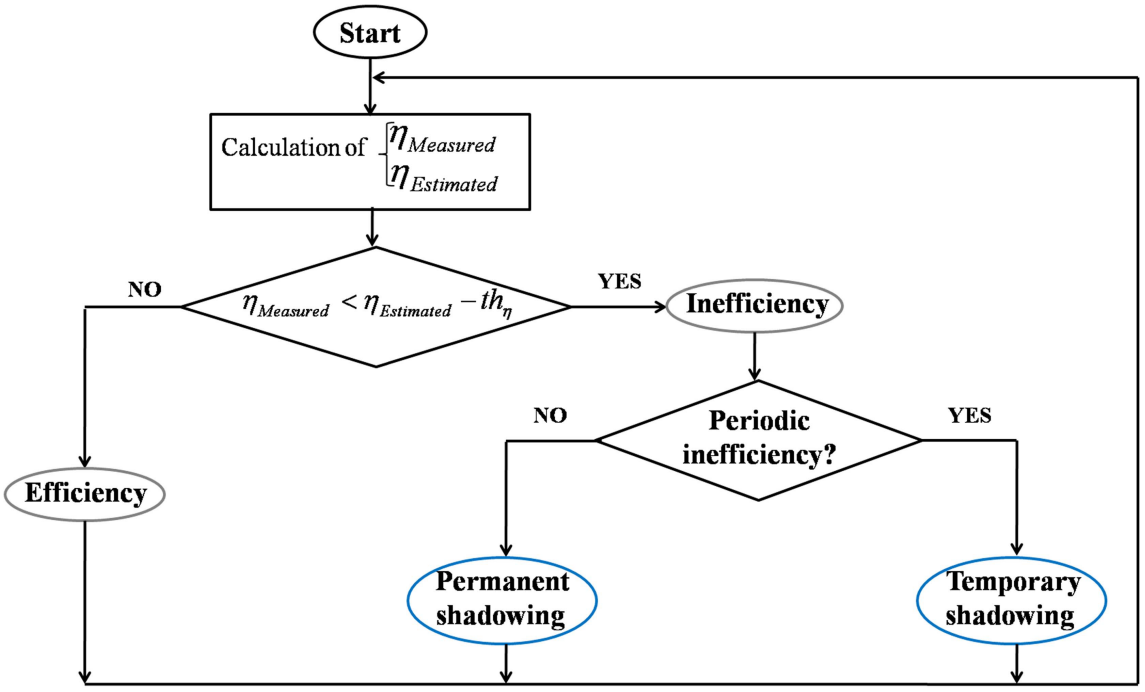

Figure 2.6: Methodological approach for the detection of the causes of efficiency losses [5].

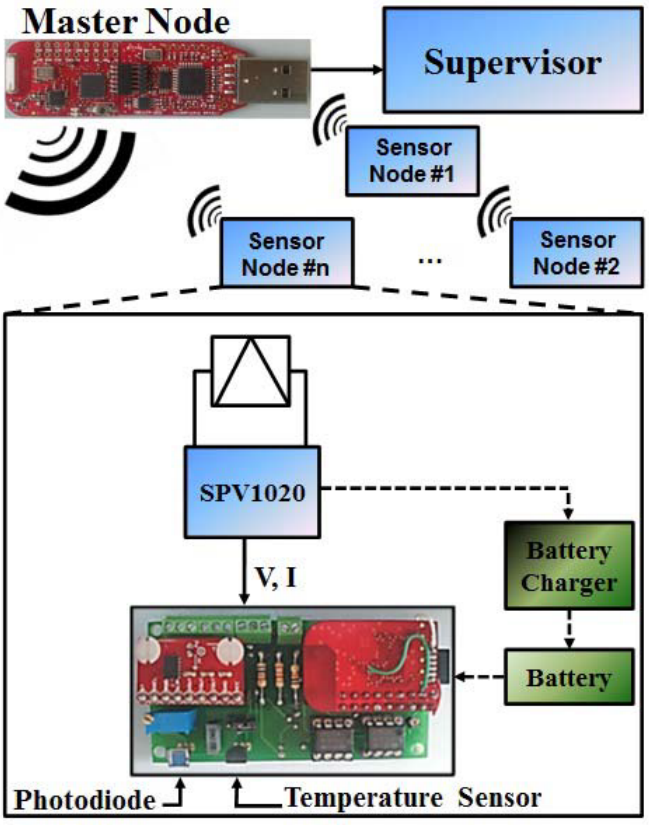

Figure 2.7: Schematization of the monitoring system used in [5].

Stellenbosch University https://scholar.sun.ac.za

Measurement data in [5] and [6] is sent via a 2.4 GHz wireless transceiver (similar to Zigbee) to a master node which sends the data via a USB connection to a supervisor (PC). The supervisor then displays measurement and analysed data as well as possible causes of efficiency losses on a LabVIEW GUI.

The monitoring system developed in [5] and [6] was tested on a single PV module. Several experiments were carried out to assess the performance of the diagnostic system in detecting the causes of inefficiency due to spot or periodic shading and soiling. Measurement and analysed data can be seen in Figure 2.8.

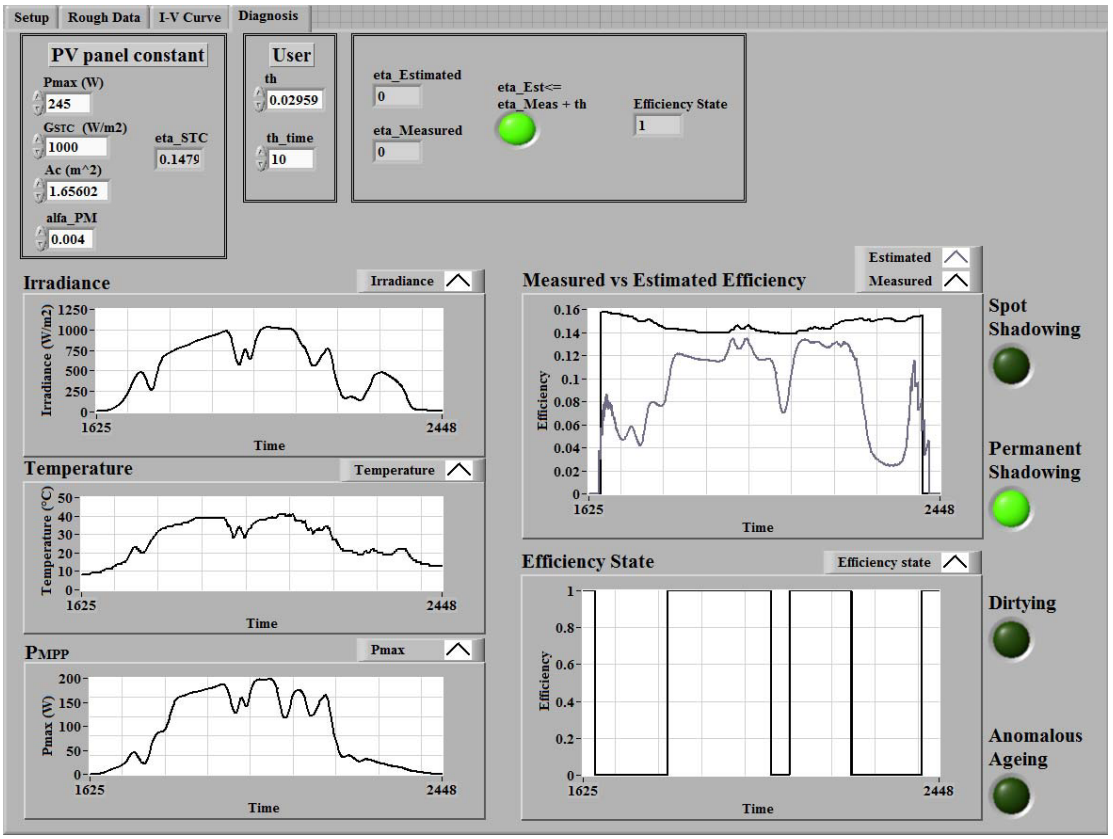

Figure 2.8: LabVIEW GUI that illustrates measurement results and causes of inefficiency [5].

The monitoring system that was developed in [5] and [6] was only tested on one PV module and there are no results that indicate how the system will function when more than one module would be. The monitoring system only displays measurement results on the supervisor (PC) and there is no indication of remote monitoring capabilities. The wireless technology used has a limited range and is not optimal for large PV installations. The sensor is powered by a battery that is charged by the PV module being measured which results in the PV module being less efficient.

2.3 Commercially Available Module Level Monitoring Systems

Case 5: The solar manufacturer Enphase developed a micro-inverter system that utilizes a micro-inverter behind each PV module in a solar installation [7]. Each of these inverters measures and sends the voltage and current of each module together with the ambient

Stellenbosch University https://scholar.sun.ac.za

temperature to a central receiver which sends the data to a website. On the website users can view the exact panel layout with performance data (live and historical) as well as any faults that occur. Figure 2.9 illustrates the web interface that displays performance data for individual modules and micro-inverters.

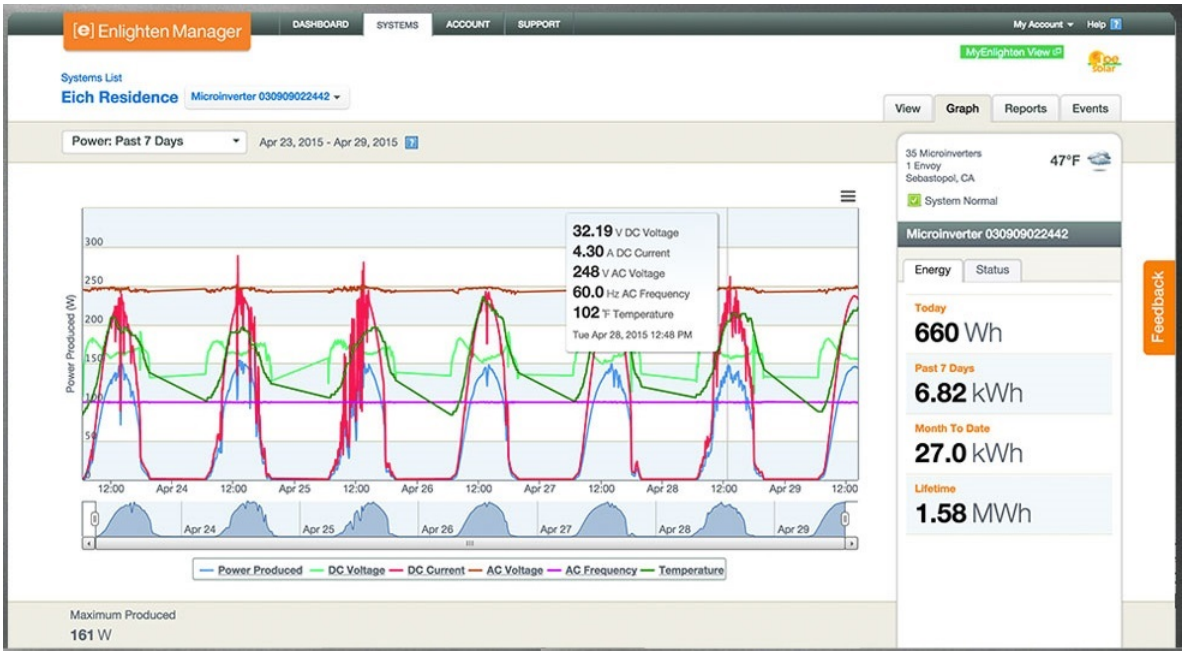

Figure 2.9: Enphase remote monitoring web application displaying micro-inverter performance measurements [7].

Measurement data is transferred from each micro-inverter to a central receiver over the AC power lines. This method of data transportation also referred to as PLC (Power-line communication). Micro inverters are more expensive than central or string inverters and are not optimal for larger PV installations [8]. The monitoring system is part of the micro-inverter and is thus not a plug-and-play monitoring solution. The monitoring system doesn't measure PV module temperature which is an important quantity in evaluating the performance of a PV module. The monitoring system is powered by the micro-inverter making it less efficient and no measurement data is captured when the sun is not shining.

Case 6: SolarEdge developed a power optimiser with module level monitoring capabilities [9]. The power optimiser is a DC-DC converter that does maximum power point tracking of each individual PV module. The power optimiser also monitors the performance of each module and sends the performance data to a monitoring platform. There are certain PV manufacturer brands that sell PV modules with the optimisers already installed within the module junction box. The power optimisers can also be attached to PV modules that do not have them pre-installed.

The power optimisers measure module voltage and current. Additional irradiance, ambient temperature, module temperature and wind velocity sensors can be added to the monitoring system. Measurement data (live and historical) can be viewed on an website or on a mobile application. Faults within a PV installation are also shown on the website or mobile application. The web based interface on which measurement data can be viewed is shown in Figure 2.10. The layout of the solar installation and the energy produced by each module are displayed.

Stellenbosch University https://scholar.sun.ac.za

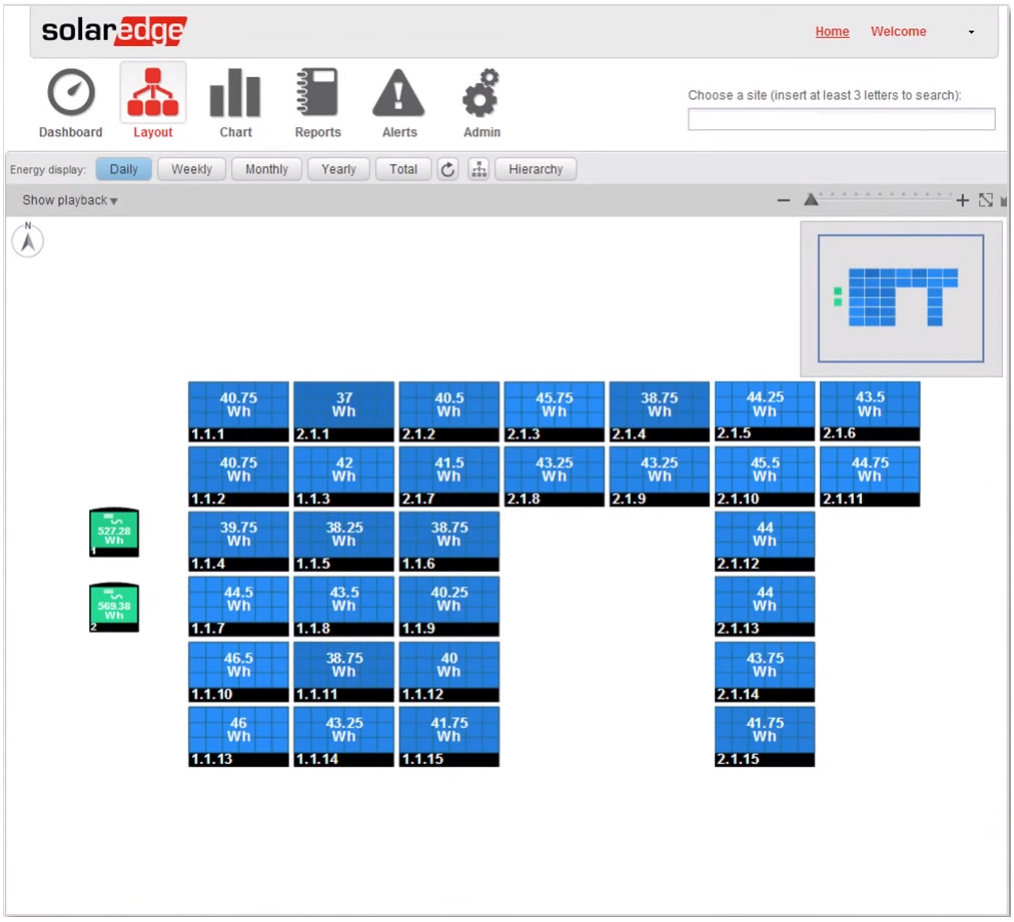

Figure 2.10: SolarEdge remote monitoring web application displaying energy produced by individual modules [9].

There is no information on how measurement data is transferred from the power optimisers to the inverters. The monitoring system forms part of the power optimisers and cannot be used separately. The power optimisers are powered by the PV modules being measured making the PV modules less efficient and no measurement data is captured when the sun is not shining.

Case 7: Tigo Energy developed range of smart modules that attach to a base plate on PV modules [10]. One of the smart modules is designed to monitor the performance of each PV module. The smart module measures module voltage and current. Measurement data is sent via a Zigbee mesh network to a gateway which sends the data to a data logger via RS-485 interface. The data logger then sends the measurement data to a cloud platform. The data (live and historical) as well as any fault that occur can be viewed on a website or via a mobile application. Figure 2.11 shows an example of the web interface that displays live and historical data of a specific solar installation. The interface illustrates the layout of each panel together with the power of each PV module and the position of the sun at that given moment.

Stellenbosch University https://scholar.sun.ac.za

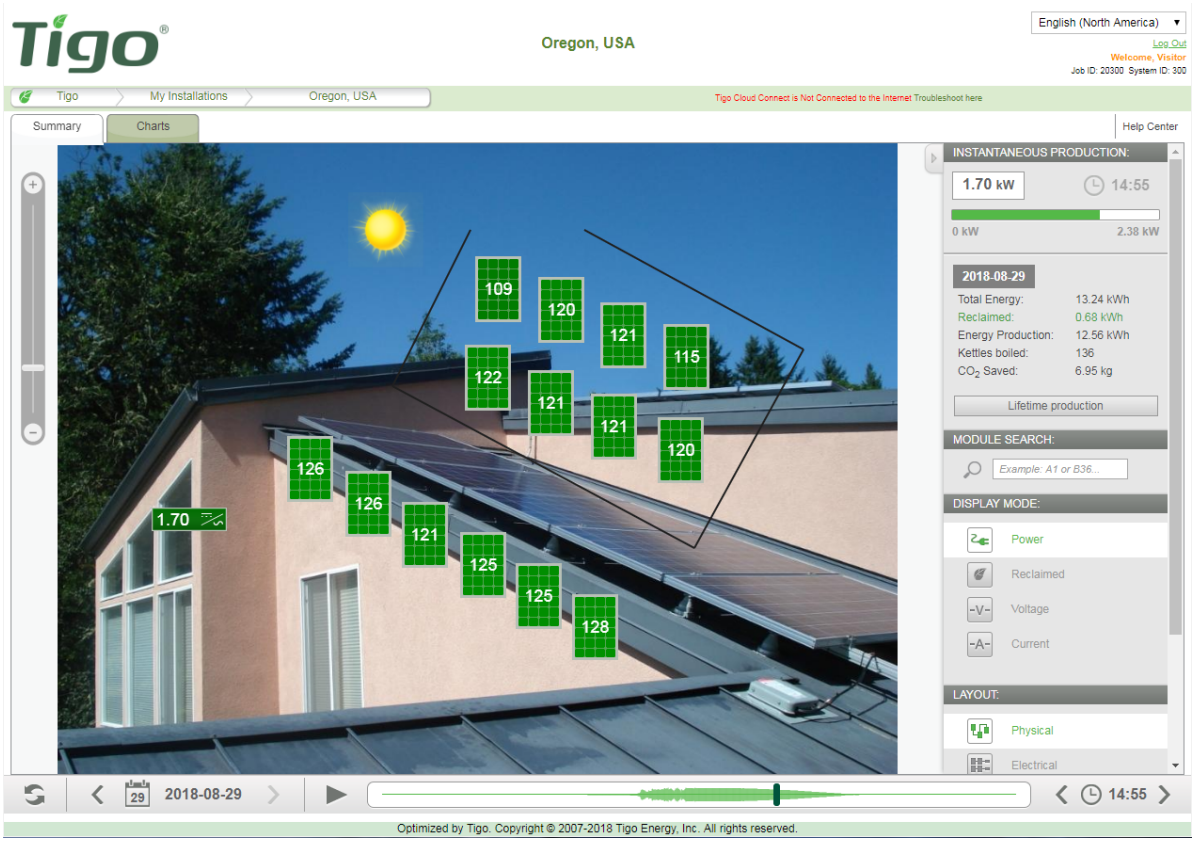

Figure 2.11: Tigo Energy remote monitoring web application displaying individual module power [10].

The smart monitoring system is capable of remote detection and diagnostic of performance issues. The smart monitoring module is a functional cover that pairs with an integrated modular junction box base. These junction boxes are either pre-installed or can be retrofit/add-on. The smart modules have a range of 10 metres and a maximum range of 70 metres from the farthest smart module to the gateway when other smart modules are present (mesh network). The smart module with monitoring capabilities only measures module current and voltage. No other performance parameters such as module temperature or irradiance are measured. The monitoring modules are powered by the PV modules being measured making the modules less efficient and no data is captured when the sun is not shining.

Table 2.1 provides a summary of different research-based and commercially available module-level monitoring systems.

Stellenbosch University https://scholar.sun.ac.za

Table 2.1: Summary of Module Level Monitoring Systems

Description	**Electrical Measurements**	**Environmental Measurements**	**Data Transfer Method**	**Range Sensor to Base**	**Fault Detection**	**Remote Monitoring**
Field Trials and Performance Monitoring of Distributed Solar Panels [2]	Voltage, Current	Irradiance, Ambient Temperature	Wireless (Zigbee)	Short (70 m)	No	No
Real-Time Measurement of Grid Connected Solar Panels [3]	Voltage, Current	Ambient Temperature, Humidity, Irradiance	Wireless (Zigbee)	Short (70 m)	No	No
Wireless Zigbee System For Performance Monitoring of PV Panels [4]	Voltage, Current	None	Wireless (Zigbee)	Short (70 m)	No	No
Smart Monitoring of PV Systems at Panel Level [5] & [6]	Voltage, Current	Module Backside Temperature, Irradiance, Inertial Events,	Wireless (2.4 GHz Transceivers, Similar to Zigbee)	Short (70 m)	Yes	No
Enphase Microinverter [7]	Voltage, Current	Ambient Temperature	Wired (Powerline communication)	Wired Communication	Yes	Yes
SolarEdge Power Optimiser [9]	Voltage, Current	None, Additional Sensors can be added	Not Specified	Not Specified	Yes	Yes
Tigo Smart Module [10]	Voltage, Current	None	Wireless (Zigbee)	Short (70 m)	Yes	Yes
Proposed Monitoring System	Voltage, Current	Ambient & Module Temperature, Irradiance, Orientation & Tampering	Wireless (LoRa)	Long (10 - 30 km)	Yes	Yes

Stellenbosch University https://scholar.sun.ac.za

2.4 PV Performance Measurement Methods and Theories

There are several models that can be used to estimate the electrical behaviour of a solar cell with respect to change in environmental parameters like temperature and irradiance. PV module modelling primarily involves the estimation of the non-linear current and voltage curves (I-V curves). There are currently two main circuit models used for these purposes: the single-diode model and the two-diode model [11]. These models represent the behaviour of a solar cell with an equivalent electrical circuit consisting of a current source, a single or double diode, and a couple of resistors. In [12] McFayden used MatLab Simulink to simulate the I-V and P-V curves for a Canadian Solar CS6P PV module using the double-diode model. The simulation results (I-V and P-V curves) obtained in [12] for different temperature and irradiance values is shown in Figure 2.12.

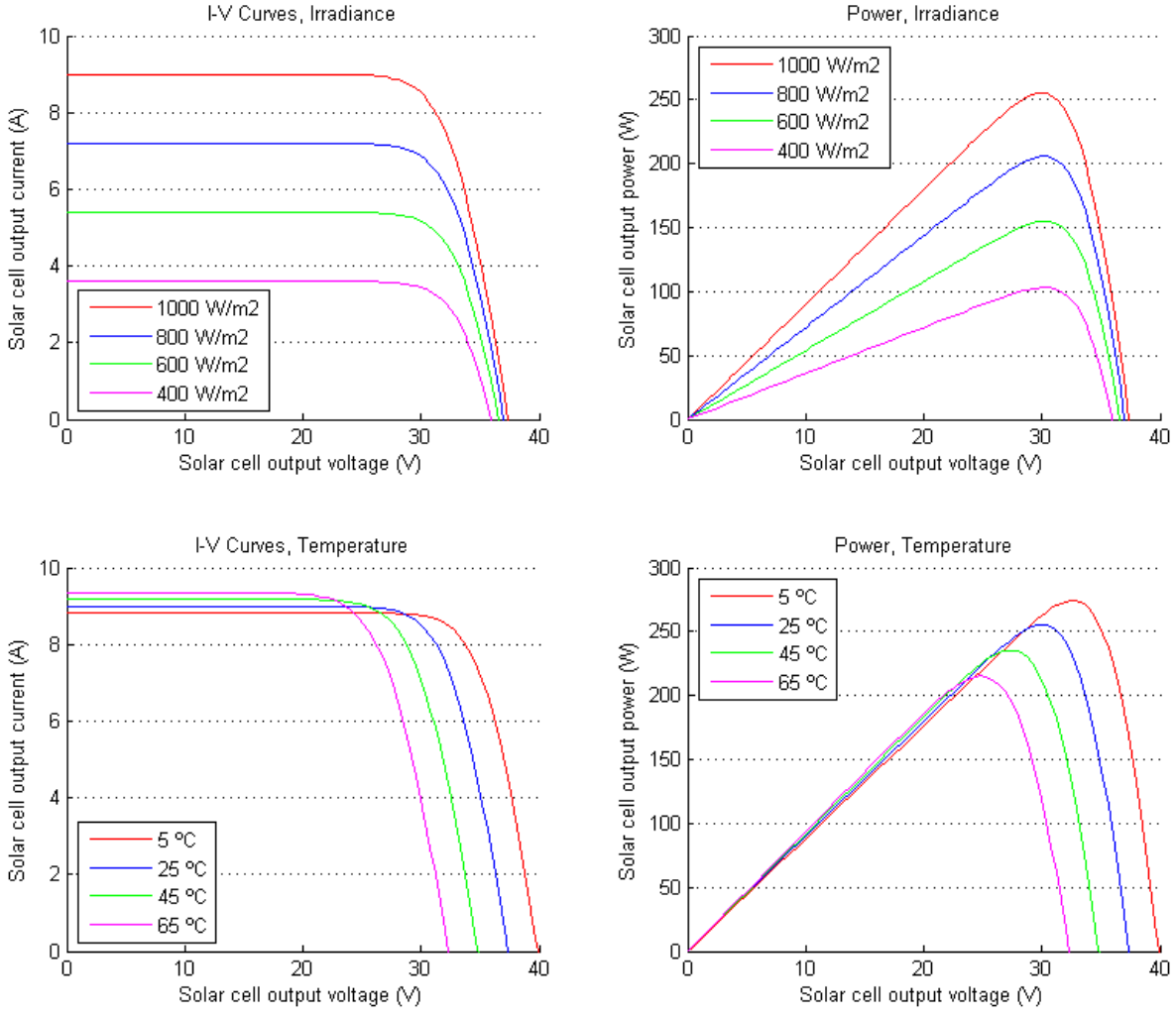

Figure 2.12: I-V an P-V curves obtained through MatLab Simulink simulations for a Canadian Solar CS6P PV module [12].

From Figure 2.12 it is evident that irradiance and temperature are the two quantities that directly influence the performance (current and voltage) of a PV module. An increase in cell temperature leads to an increase in cell current but a decrease in cell voltage and power. An increase in irradiance leads to a increase in current, voltage and power. The performance

Stellenbosch University https://scholar.sun.ac.za

of a PV module can thus be obtained by measuring the voltage, current, temperature and irradiance of that specific PV module.

2.4.1 DC Voltage Measurement Methods

Voltage is a potential difference and corresponds to the 'potential' or ability for electrons to flow around a circuit. Voltage measurement always requires a direct connection to the terminals that are being measured. Circuits with a voltage above 55 V are considered high voltage circuits which can produce a dangerous electrical shock [13]. There are currently three main types of solar panels that are used in the solar industry. They are Monocrystalline, Polycrystalline and Thin-Film [14]. Mono- and Polycrystalline modules with a Watt rating of 200 - 350 Watt have a open circuit voltage of 35 - 45 V. Thin-Film modules with a lower Watt rating typically have a open circuit voltage of 90 - 110 V.

2.4.1.1 Non-Isolated Voltage Measurement Methods

Non-isolated voltage measurement occurs when the input and output voltage are referenced to each other in some way, usually they share the same ground. This method is simple to implement but there are some over-voltage and safety issues that might occur when dealing with higher voltages.

Potential Divider A potential divider circuit is often used to measure voltage in devices such as multimeters. The input voltage is scaled by certain factor that falls within the voltage limits of the ADC (Analog-to-Digital Converter). Figure 2.13 illustrates an example of a potential divider circuit.

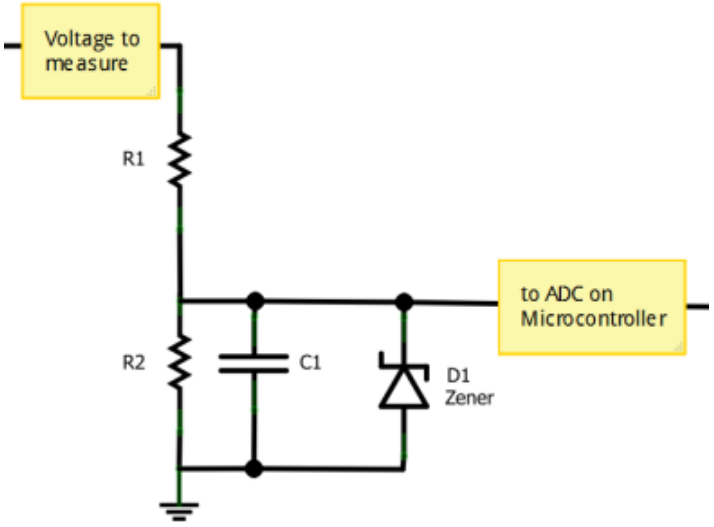

Figure 2.13: Potential Divider Circuit with Filtering and Over-Voltage Protection adapted from [13].

The output voltage that is measured by the ADC can be calculated as follow:

$$V_{out} = V_{in}\left(\frac{R2}{R1 + R2}\right) \tag{2.1}$$

Stellenbosch University https://scholar.sun.ac.za

Capacitor C1 is a filter capacitor. This capacitor removes any high frequency noise in the signal that is sampled by the ADC. Diode D1 is a zener diode that will break down when a voltage greater than the zener voltage (diode rating) is applied,limiting the voltage to the zener voltage. This is done to protect the any circuitry that is downstream of the zener diode such as the microcontroller.

2.4.1.2 Isolated Voltage Measurement Methods

When measuring voltages above 55 V it is advised to make use of isolated measurement techniques when measuring voltage [13]. 55 V is known as the voltage above which dangerous current can flow through the skin, hence anything above 55 V is potentially dangerous [13]. Isolated voltage measurement happens when the input voltage and output voltage are electrically isolated and thus not referenced to one another.

Hall-effect Sensor Hall-effect voltage measurement works by converting a voltage into a current by means of a resistor. Measuring current through a known resistance gives a voltage by using Ohm's law. A hall-effect sensor is a transducer that develops an output voltage (Hall Voltage) that is proportional to the applied magnetic field which is caused by flowing current [15]. Figure 2.14 depicts the working principle of a Hall-effect sensor. Hall-effect sensors are mainly used to measure current thus it requires a decent current signal (in the order of a few ampere) to generate a hall voltage. Hall-effect sensors can measure AC and DC current. When measuring a voltage of 50V by means of a hall-effect sensor that requires 1A, 50 Watt will be dissipated by the resistor which results in significant energy loss.

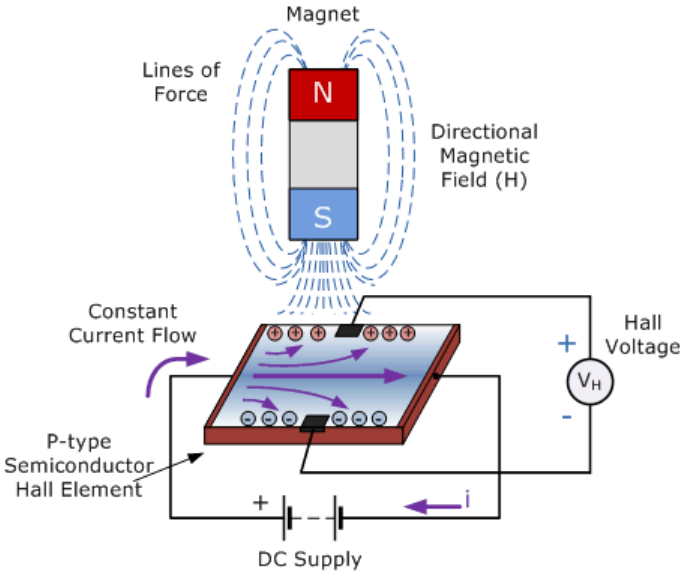

Figure 2.14: Hall-Effect Sensor Working Principle [15].

Isolation Amplifier An isolation amplifier is a type of IC (Integrated Circuit) which has two electrically isolated sides. The input voltage of the isolation amplifier is passed to the output via an optical connection thus providing electrical isolation. The output voltage is proportional to the input voltage. The advantages of using an isolation amplifier is isolated voltage measurement with a low input power. The downside to using an isolation amplifier is that an additional isolated supply voltage is required for the input side and that isolation amplifiers have a small input voltage range (in the mV range) because they are mostly used for current measurement through a shunt resistor [13].

Stellenbosch University https://scholar.sun.ac.za

Optocoupler An optocoupler also known as a opto-isolator or photo-coupler interconnects two separate electrical circuits by means of a light sensitive optical interface, thus providing electrical isolation. The basic design of an optocoupler consists of an LED and a light sensitive receiver which can be a photo-diode, photo-transistor, photo-resistor, photo-SCR or a photo-TRIAC. The basic operation of a optocoupler is a current that passes from the source signal through the input LED which transmits an infra-red light which has an intensity that is proportional to the electrical signal. The emitted light is picked up by the light sensitive receiver and converted back to a current or voltage based on the type of receiver [16]. The basic operating principle of a optocoupler using a photo-transistor can be seen in Figure 2.15.

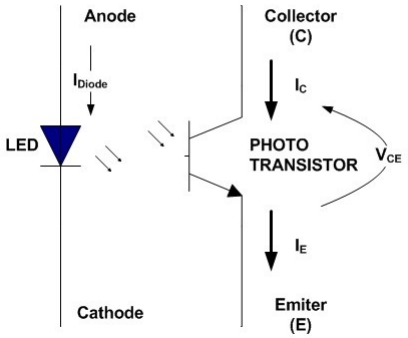

Figure 2.15: Basic Optocoupler Working Principle: Photo-Transistor [16].

Optocouplers are mainly used to isolate digital signals and not analog signals. This is due to the high non-linearity which is caused by an LED's non-linear time and temperature characteristics. Digital signals are either 'high' or 'low' and the non-linearity doesn't influence the measurement result. To make use of an optocoupler when measuring voltage, the analog voltage signal first has to be converted to a digital value which can then be isolated by the optocoupler and sent to a microcontroller for interpretation. The conversion from an analog voltage signal to a digital value is done by an ADC. Thus an ADC and an isolated power supply needs to be added to the 'high voltage' side together with the optocoupler (digital isolator) to provide an isolated voltage measurement.

Linear Optocoupler Another method in which optocouplers can be used to measure voltage is to use linear optocouplers. Linear optocouplers provide an output that is linearly proportional to the input. A linear optocoupler consists of one LED and two photo-diodes. The LED and the photo-diodes have to be connected to external Op-amps (operational amplifiers) which are used to ensure linearity by creating a feedback loop. An Op-amp is required on each side of isolation. Figure 2.16 illustrates a typical circuit used to create an output voltage which is linearly proportional to the input voltage using a linear optocoupler.

Stellenbosch University https://scholar.sun.ac.za

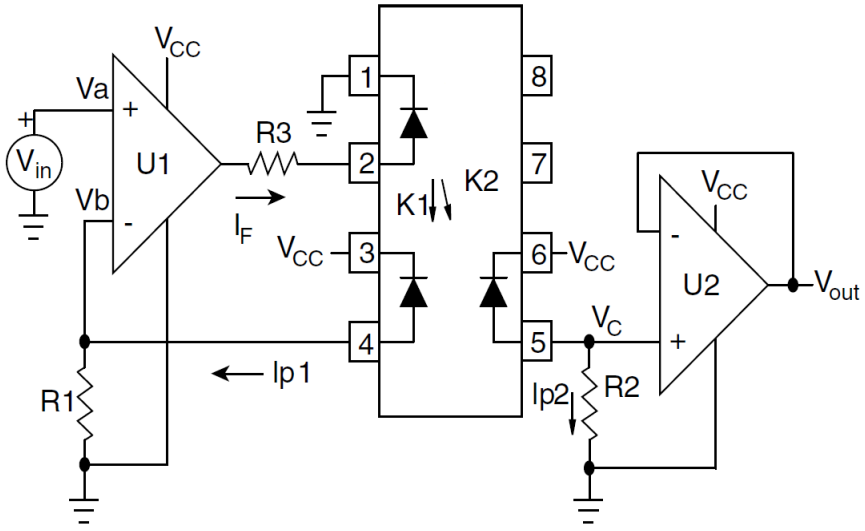

Figure 2.16: Linear Optocoupler Application Circuit [17].

The circuit makes use of a linear optocoupler, two single-supply Op-amps and three resistors. The circuit works as follow: When there is a sense voltage V_{in} the Op-amp will amplify the difference between V_a and V_b which in turn creates a voltage at the output of the Op-amp. This voltage together with R3 causes a current I_F to flow which drives the LED. This causes photocurrent I_{P1} which is connected in negative-feedback arrangement with the Op-amp to flow. I_{P1} is directly proportional to the feedback transfer gain K1 times the LED drive current I_F. I_{P1} together with R1 causes voltage V_b. This effectively means that the Op-amp will supply LED current I_F to force sufficient photocurrent I_{P1} to keep the node voltage V_b equal to V_a. The equation for V_{in} can be written as:

$$V_{in} = V_a = V_b = I_{P1}R1 = K1I_FR1 \tag{2.2}$$

The characteristic that makes a linear optocoupler linear is the fact that the 'high-side' and the 'low-side' photo-diodes have almost the exact same response to the LED [17]. The 'low-side' photo-diode is connected to a non-inverting voltage follower amplifier. The photo-diode load resistor R2 performs the current to voltage conversion. The equation for V_{out} can be written as:

$$V_{out} = V_c = I_{P2}R2 = K2I_FR2 \tag{2.3}$$

The overall transfer gain equation can be written as:

$$\frac{V_{out}}{V_{in}} = \frac{K2I_FR2}{K1I_FR1} = \frac{K2R2}{K1R1} \tag{2.4}$$

The overall transfer gain is completely independent of the LED forward current and thus not influenced by LED non-linearities. This method is called feed-back linearised current control [17].

Stellenbosch University https://scholar.sun.ac.za

2.4.2 DC Current Measurement Methods

2.4.2.1 Invasive Current Measurement Methods

There are two main methods of measuring DC current: invasive and non-invasive. Invasive methods are when something is placed in the actual current path, usually a resistor with a small value (called a shunt resistor). Current flowing through a small resistor causes a small voltage drop. This voltage can be measured using a ADC and converted back to a current using Ohm's law.

There are issues that arise when measuring current with a shunt resistor. The resistor value has to be low to avoid a high power loss. Power dissipated by a shunt resistor can be calculated as:

$$P_{shunt} = I^2 \cdot R_{shunt} \tag{2.5}$$

When using a small shunt value (0.01 milli-Ohm) the power dissipated is low, but the voltage that is produced across the shunt that needs to be sampled is low as well (0.1 mV for 10 A). This value can be amplified with a operational amplifier before being sampled, which introduces other issues such as offset and noise. When using a higher shunt value (1 Ohm), there is a lot of wasted energy (100 Watt for 10A). There is also no electrical isolation between the main circuit where the measurement current flows and the measurement circuitry when using the shunt resistor current measurement technique.

2.4.2.2 Non-Invasive Current Measurement Methods

Non-invasive current measurement methods are similar to isolated voltage measurement methods since there is no electrical connection between the measurement circuit and the circuit in which the measured current flows. The non-invasive current measurement method that is generally used in high current applications (1 - 20 A) is Hall-effect sensors. Hall-effect sensors are ideal for measuring PV module current because the measurement circuitry is electrically isolated from the the circuit where the measured current is flowing. Hall-effect sensors are discussed in Section 2.4.1.2.

2.4.3 Temperature Measurement Methods

There are many types of temperature measurement methods and sensors. These include thermocouples, resistive temperature measuring devices, infrared sensors, bimetallic devices, thermometers, change-of-state sensors and silicon diodes. When measuring temperatures relating to PV module performance the PV cell-temperature is required. This is difficult to obtain using a contact sensor since the temperature sensor needs to be physically (directly) attached to the solar cell. Although the cell temperature inside the module is typically higher than the module backside temperature, a good approximation can be obtained by attaching a temperature sensor to the backside of the PV module [5].

There are various of temperature sensing IC's that can be used to measure module backside temperature. These IC's are either analog or digital. Analog temperature sensors produce an output voltage that is proportional to the temperature. Digital sensors provide a temperature reading in a digital format, usually I^2C or SPI interface. The accuracy of these sensors vary and are directly proportional to the price of the sensor. By attaching a temperature sensing IC with a good accuracy (0.5% - 1%) to the backside of a PV module, adequate temperature measurements relating to PV module performance can be made [5].

Stellenbosch University https://scholar.sun.ac.za

2.4.4 Irradiance Measurement Methods

Irradiance measurements are usually done with sophisticated devices. A pyranometer measures global radiation and a pyrheliometer measures direct radiation. These devices measure irradiance with high accuracy and cover a wide spectral range. These devices are expensive and not suitable for attachment to a number of sensor nodes in a low-cost sensor network that measures individual PV modules.

A good estimation of irradiance can be obtained by measuring light intensity [2]. There are several of electronic components that can be used to convert light intensity to a certain electrical output signal. A LDR (Light Dependent Resistor) is a component that changes its electrical resistance value depending on the amount of light that the resistor is exposed to. A LDR has a long response time and the change in resistance is non-linear with the amount of light that the resistor is exposed to [5].

Another component that can be used to convert light intensity to an electrical signal is a photodiode. A photodiode converts light into an electrical current. This current is directly proportional to the amount of light that the photodiode is exposed to. The response time of a photodiode is fast and the current generated by a photodiode is linear with the amount of light that the photodiode is exposed to [18]. By using a low-cost photodiode a good estimation of irradiance relating to PV module performance can be made [19].

2.5 Wireless Technologies Assessment

When developing a monitoring system that consists of multiple sensors an important design choice is how measurement data is sent from the sensors to a central point where the data can be stored, viewed and analysed. There are two main methods of data transfer, wired and wireless.

There are many advantages that wireless technologies have over wired technologies for a monitoring system that consists of a number of sensor nodes that are spread out over a certain area. Establishing a wireless network is more cost-effective, as no cables between the sensors and the central gateway are required. Wireless networks are faster to deploy and are modular, meaning extra nodes can be be added to the network and nodes can be removed from the network without interfering with the rest of the network. A wireless network also has more mobility, sensor nodes can be moved around and attached to other PV modules without the need to install new cables.

There are several of wireless technologies that can be used to transfer measurement data in a WSN. There are a few key factors to investigate when evaluating different wireless technologies for a WSN. These include: range, power demands, data requirements, network topology and network security. The importance and weight of the different factors depend on the specific application in which the wireless technology is deployed.

Range For a WSN where monitoring devices (sensor nodes) are placed on various positions spread out across a solar installation, range is a key factor. Medium and large solar installations can cover areas of a few hundred square meters to thousands of square meters. Range is a crucial factor to ensure that sensor nodes can be placed anywhere on the solar installation without the need for additional routers and/or cables to transmit data to a central gateway.

Stellenbosch University https://scholar.sun.ac.za

Power Demands Each sensor node in the WSN needs power to take measurements and send measurement data to a central gateway. If the sensor node is powered only by the PV module that it measures, the sensor will not have any power when the sun is not shining. This approach will also lead to the module being less efficient since it has to supply some of its power to the sensor node. If the sensor node is powered by a battery and uses a lot of power the battery either has to be large or the battery has to be charged frequently. The ideal would be to have a sensor node that is compact, that doesn't influence the efficiency of the PV module, and that can last for a long period in the field. Taking these factors into consideration, it follows that power consumption of the wireless technology is of paramount importance.

Data Requirements The data being sent over the WSN are small packets of measurement data. Intervals at which data is sent will differ based on the level of measurement detail that is required. This may vary from a few seconds to a several number of minutes. Measurement data can be represented as a few bytes; thus the wireless technology doesn't need to have fast data rates.

Network Topology When considering network topology there are two topologies that are most commonly used in wireless technologies. They are star topology and mesh networking [20]. Star topology implies that all the nodes or end devices are connected to a central point or gateway. Mesh networking is where each node relays data from other nearby nodes to the desired node or gateway. When using a star topology network, each node has to be in range of a central gateway, which requires increased communication range and/or many gateways. However, the protocol is simple, since data is sent directly to the gateway and doesn't need to be routed along other nodes to the gateway. This also means that each node has a much shorter transmit time or TOA (Time On Air) because it only has to send its own data and not that of other nodes. Monitoring devices also use less power because they are not transmitting constantly. The number of devices that can connect to a single gateway in a star topology network is dependent on the wireless technology and application.

Mesh networks have more complicated protocols because data packets have to be routed between different nodes to reach the desired node or gateway. This topology has the benefit that nodes don't need the range required in a star topology, as long as there are other nodes placed between a node or end device and the desired node. Mesh nodes have a longer TOA because they are constantly routing data in the mesh network. Mesh networks are scalable and the network capacity can be increased by simply adding new nodes. Mesh networks have the additional benefit that they are self-healing: The network automatically finds the fastest and most reliable paths to send data, even if nodes are blocked or lose their signal. Figure 2.17 is a diagram showing the conceptual difference between a mesh and star network topologies. A star topology or a mesh network would be an adequate topology for a module level monitoring system based on the size and scale of the deployment.

Stellenbosch University https://scholar.sun.ac.za

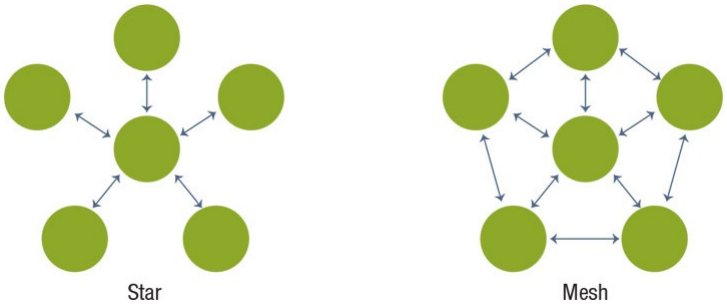

Figure 2.17: Diagram Showing the conceptual difference between Star and Mesh Network Topologies

Network Security Since no sensitive information is sent over the wireless network, security is not a main concern in the evaluation of different wireless technologies.

2.5.1 Wireless Technology Fundamentals

There are three competing requirements for wireless technologies namely: long range, high bandwidth (high speed) and low power consumption. The law of physics prevent a wireless technology from having all three, with two at most being possible [21].

The 'link budget' shown in Figure 2.18 describes how much power is lost between a transmitter and receiver when a radio wave is transmitted over a certain distance in free space.

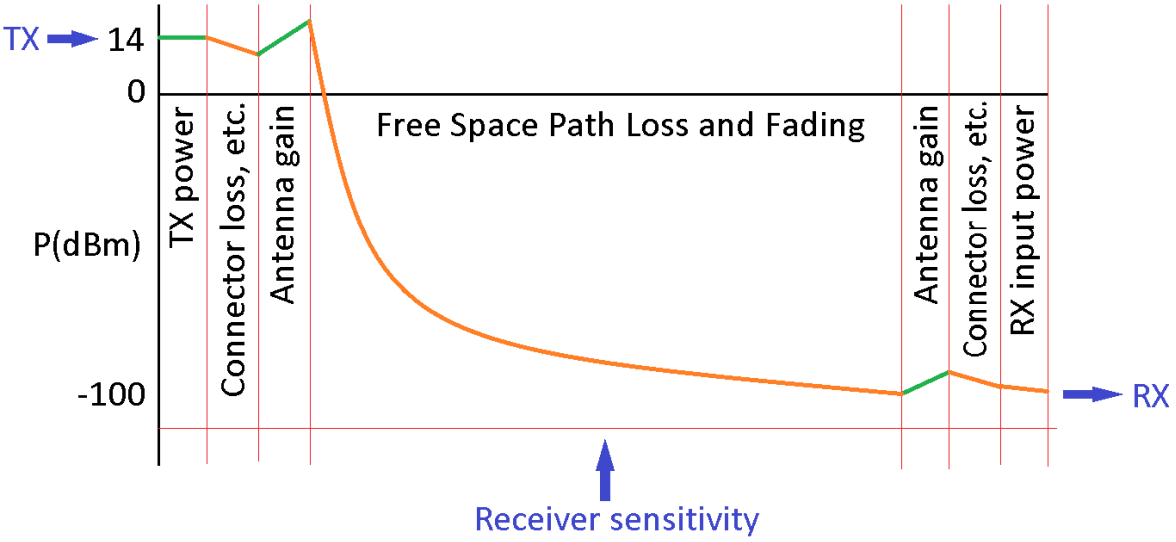

Figure 2.18: The Link Budget of a Transmitted Radio Wave adapted from [21].

In the case of a line-of-sight connection the FSPL (Free Space Path Loss) is where most of the transmitted power is lost. The free space propagation model is a simple representation of the power loss when a signal travels in free space. The FSPL as expressed in terms of wavelength and frequency [22]:

$$FSPL = \left(\frac{4\pi d}{\gamma}\right)^2 = \left(\frac{4\pi df}{c}\right)^2 \tag{2.6}$$

Where:

Stellenbosch University https://scholar.sun.ac.za

d = distance from the transmitter to the receiver (m)

γ = signal wavelength (m)

f = signal frequency (Hz)

c = speed of light (m/s)

Equation 2.6 can be written in terms of a direct loss in decibels, making it possible to calculate elements including expected signal. The equation in terms of decibels are:

$$FSPL(dB) = 20log(d) + 20log(f) + 32.44 \tag{2.7}$$

Where:

d = distance of the receiver from the transmitter (km)

f = signal frequency (MHz)

When adding the antenna gain and feeder losses the equation becomes:

$$FSPL(dB) = 20log(d) + 20log(f) + 32.44 - Gtx - Grx \tag{2.8}$$

Where:

Gtx = overall transmitter antenna gain including feeder losses (dB)

Grx = overall receiver antenna gain including feeder losses (dB)

From equation 2.6 it can be seen that the FSPL scales with the square of the distance and the square of the frequency. Higher frequency equals a higher bandwidth but a shorter range. Lower frequency equals a longer range but slower data rates. High power transmitted equals high power consumption.

There are many wireless technologies that can be used for WSNs that satisfy one or two of the competing requirements. Popular technologies with good market momentum in terms of big partnerships, deployments and PR (Public Relations) profiles that will be evaluated (and are available in South Africa) are Bluetooth, ZigBee, Wi-Fi, GSM, Sigfox and LoRa.

2.5.2 BLE

BLE (Bluetooth Low Energy) also known as Bluetooth Smart v4.0 or higher, is a short range communications technology that operates in the 2.4 GHz ISM (Industrial, Scientific and Medical) band. The ISM band is a licence free band with certain duty-cycle and transmit power limitations. BLE has a maximum range of 100 m and data rates of up to 1 Mbps (Megabits per second). BLE uses 10 - 500 mW when transmitting compared to the previous Bluetooth versions that use up to 1 Watt [23]. BLE is a point to point network although there have been attempts to create a mesh networking protocol. A maximum of 10 BLE devices can connect with another (or central) BLE device.

Stellenbosch University https://scholar.sun.ac.za

2.5.3 ZigBee

ZigBee is a wireless mesh networking technology based on the IEEE802.15.4 standard. Most ZigBee chipsets operate in the 2.4 GHz ISM band. ZigBee chipsets have a data rate of up to 250 kbps and uses as little as 1 mW when transmitting and receiving [24]. ZigBee mesh networks can support several hundreds of nodes. Typical Zigbee chipsets have a maximum outdoor range of 70 m although there are chipsets that claim to have a longer range in line-of-sight conditions.

2.5.4 Wi-Fi

Wi-Fi is a technology for wireless local area networking. It uses the IEEE 802.11a, 11b, 11g, 11n, 11ac and 11ad standards. Wi-Fi operates in the 2.4, 3.6, 5 and 60 GHz ISM bands. It has an indoor range of 50 m and an outdoor range of 150 m [25]. Wi-Fi has a data rate range of between 6 - 780 Mbps and 6.75 Gbps at 60 GHz. Wi-Fi is designed for high data rates required for multimedia contents as opposed to applications like sensor networks. Wi-Fi has a high-power consumption, it uses approximately 1 Watt when transmitting.

2.5.5 GSM

GSM has many standards like GPRS, EDGE, HSDPA and LTE or 2G - 5G. GSM operates on frequencies between 700 MHz and 2600 MHz and communications have a range of 10 km - 30 km, with data rates of 35 Kbps - 1 Gbps [26]. GSM operates in the licenced bands that are used by MNO (Mobile Network Operator) such as Vodacom, MTN and CellC in South Africa. To use GSM in South Africa each end device must be connected to a MNO's network. GSM uses between 1 and 5 Watt when transmitting [27].

2.5.6 LPWAN

LPWAN (Low-Power Wide-Area Network) is a wireless wide area network that is specialised for interconnecting devices with a low-bandwidth connectivity, focussing on range and power efficiency. A comparison of different wireless technologies in term of speed (bandwidth) and range is shown in Figure 2.19.

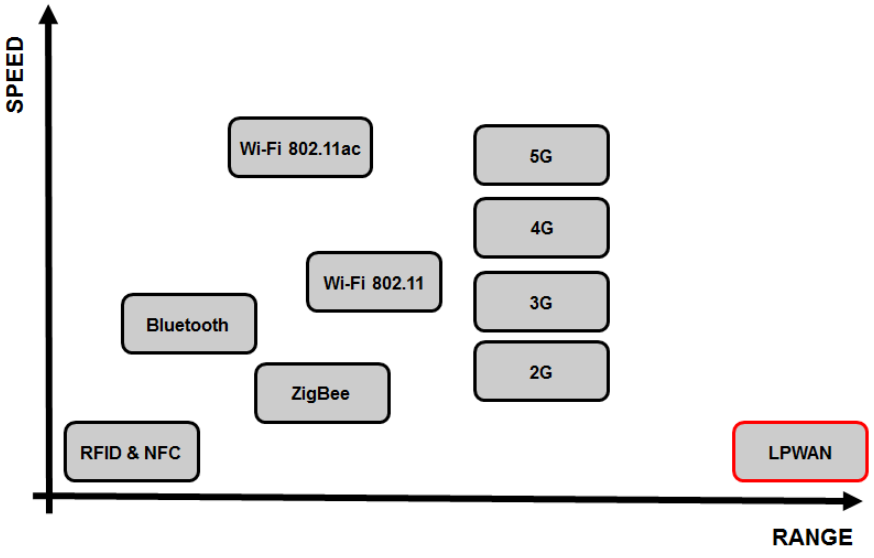

Figure 2.19: Comparison of Different Wireless Technologies in term of Speed and Range

Stellenbosch University https://scholar.sun.ac.za

There are many different LPWAN technologies but two technologies with good market momentum in terms of big partnerships, deployments and PR profiles that are available in South Africa are Sigfox and LoRa [28].

2.5.6.1 Sigfox

Sigfox makes use of UNB (Ultra Narrow Band) BPSK (Binary Phase Shift Keying) modulation to transmit data and has range of 20 - 50 km in suburban areas [26]. Sigfox has a data rate of 100 bps (bits per second) and a single gateway can handle thousands of nodes. Devices consume 160 mW when transmitting and each device transmits for a short period since Sigfox makes use of a star network topology with strict TOA regulations [28].

Sigfox uses a business model where Sigfox acts as a carrier and they sell subscription to their network, like that of cellular carriers. Sigfox operates in the 868 MHz ISM band in South Africa and subscription fees are much lower than those of cellular. The devices are cheap and use low amounts of power. Devices cost as little as $3 and subscription fees are around $1 per device per year [28].

The downside to Sigfox is that a single end device can send a maximum of 140 12-byte messages to a gateway per day [28]. That is one 12-byte message every 10 minutes. An end device can receive only two 8-byte messages from the gateway per day.

2.5.6.2 LoRa

LoRa is a wireless modulation technology; it is the physical layer to connect to other nodes or a gateway. LoRa uses a chirp-based spread spectrum modulation technique. It is robust to interference, multipath and fading due to its unique modulation scheme [29]. LoRa is low bandwidth and uses little power. It operates in the license-free ISM bands all around the world, 433 MHz and 868 MHz in South Africa. LoRa radio chipsets use less than 100 mW when transmitting [28].

Data rates for LoRa range from 300 bps to 5.5 kbps. There are two additional high-speed channels that make use of FSK (Frequency Shift Keying) modulation with rates of 11 kbps and 50 kbps [30]. LoRa supports bidirectional communication and a LoRa message can contain up to 250 bytes. LoRa modules have a range of 10 km - 30 km in suburban areas [30].

LoRa makes use of different spreading factors which set the modulation rate, thus also influencing the data rate. The spreading factors range from SF7 to SF12. SF7 is the fastest (5.5 kbps on 868 MHz) but doesn't have a long range whereas SF12 is the slowest (300 bps on 868 MHz) but it has a long range. Table 2.2 indicates the symbol rate, SNR limit, TOA and bit rate for the different spreading factors [30].

Table 2.2: LoRa Spreading Factors, Symbol Rate, SNR limit, TOA and Bit Rate.

Speading Factor	**Symbols /second**	**SNR limit**	**TOA (10-byte packet)**	**Bit Rate**
7	976	-7.5	56 ms	5469 bps
8	488	-10	103 ms	3125 bps
9	244	-12.5	205 ms	1758 bps
10	122	-15	371 ms	977 bps
11	61	-17.5	741 ms	537 bps
12	30	-20	1483 ms	293 bps

Stellenbosch University https://scholar.sun.ac.za

Figure 2.20 details a visual representation of the influence that different spreading factors have on range, energy, TOA and bit rate.

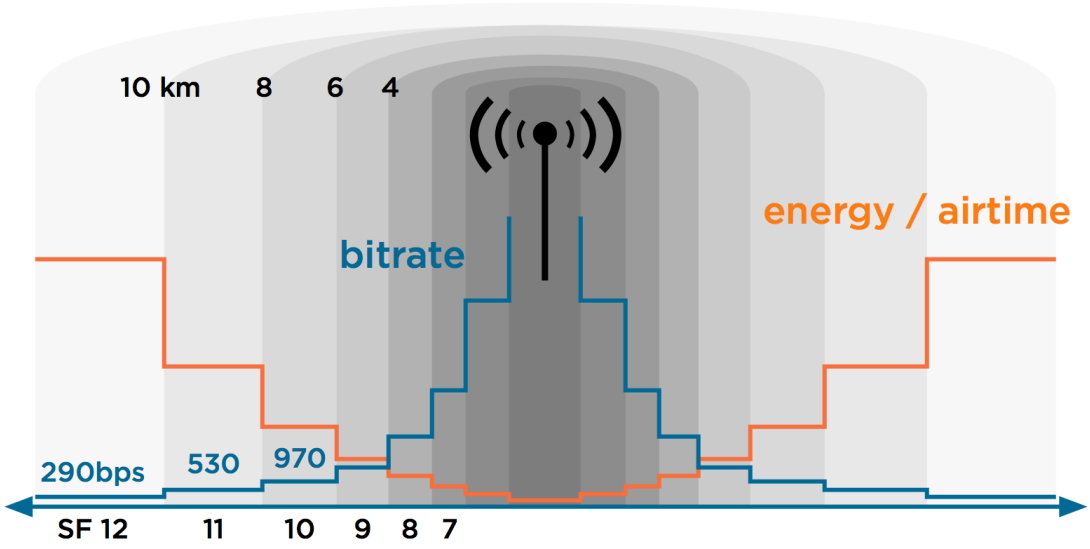

Figure 2.20: Influence of Spreading Factor on Range, Energy, TOA and Bit Rate.

LoRa chipsets can be programmed to operate in a point-to-point topology, a star topology or a mesh topology [31]. A private LoRa network can be created with two or more LoRa devices, or a LoRa device can be connected to a public LoRa network which is referred to as a LoRaWAN network. LoRaWAN networks send data received from LoRa devices to Internet connected applications through a network server.

A summary of the different wireless technologies that were evaluated in terms of operating frequency, range, data rates, power usage and network topology is presented in Table 2.3.

LoRa is an ideal wireless networking technology for a module level monitoring system which consists of a number of sensors that are deployed on a small, medium or large solar installation. LoRa is low-power, it has adequate data rates and has a good range. A private sensor network could be deployed with LoRa and a mesh or star topology could be implemented.

Table 2.3: Summary of Different Wireless Technologies in terms of Frequency, Range, Data Rates, Power Usage and Topology

Wireless Technology	**Operating Frequency**	**Range**	**Data Rate**	**Power Usage**	**Topology**
BLE	2.4 GHz	100 m	1 Mbps	10 - 500 mW	Point-to-Point
Zigbee	2.4 GHz	70 m	250 kbps	1 mW	Mesh
Wi-Fi	2.4, 3.6, 5 and 60 GHz	150 m	6 Mbps - 6.75 Gbps	1 W	Star
GSM	700 - 2600 MHz	10 - 30 km	35 Kbps - 1 Gbps	1 - 5 W	Star
Sigfox	868 MHz	20 - 50 km	100 bps	160 mW	Star
LoRa	433, 868 MHz	10 - 30 km	0.3 - 5.5 kbps	100 mW	Star, Mesh

Stellenbosch University https://scholar.sun.ac.za

Chapter 3

System Modeling and Design

3.1 Chapter overview

In this chapter the requirements for the proposed monitoring system are determined based on the research done in Chapter 2 and the objectives set out in Chapter 1. A theoretical model that evaluates the performance of a PV model is presented along with a functional diagram of the measurement system with all of its sub-components.

3.2 Functional Requirements

The requirements for the monitoring system were determined in order to fulfil the objectives given in Chapter 1. The decisions were based on the research done in Chapter 2. The monitoring system consists of sensor nodes, a gateway, a data storage facility (the cloud) and a GUI.

3.2.1 Measurement

The sensor nodes are required to measure electrical and environmental quantities that describe the performance of an individual PV module. These quantities are: voltage, current, module temperature and irradiance as set out in Section 2.4. The sensor nodes are not required to measure the closed circuit current, open circuit voltage or to draw the I-V curve of the module that is being measured. Taking these measurements would alter the normal behaviour of the PV module when operating in an active solar installation [6].

3.2.2 Data Collection

The sensor nodes are required to send measurement data to a central gateway via a wireless network. The wireless network is required to be low power, and to have an adequate range for operating on a small, medium or large solar PV installation. The gateway is required to store measurement data in a database that can be accessed remotely and immediately. Each data packet must have a date and time stamp.

3.2.3 Modelling

A model is required to evaluate the electrical and environmental measurement data for each PV module. The model must use electrical and environmental measurement data to calculate measured and expected efficiency. Based om a user defined threshold the model must be able to detect, and distinguish between, normally operating and faulty modules.

Stellenbosch University https://scholar.sun.ac.za

3.2.4 Data Visualization

A GUI is required to visualise measurement data. The GUI must be able to show a layout of the PV installation and where the various sensor nodes are located within the installation. The GUI is required to display measurement data such as temperature, voltage, current, power, irradiance and efficiency. The GUI is also required to show the health status of each module.

3.2.5 Remote Detecting and Reporting

The GUI that displays measurement data must be capable of running on any PC anywhere with an Internet connection. The GUI is required to report certain events that occur on the PV modules and/or sensor nodes to the user.

3.3 Fault Detection Model

The main purpose of the fault detection model is to detect when a PV module within a PV installation is not operating 'normally', thus detecting if there is a fault on a specific module. Methodologies for fault detection in PV systems can be classified into three main categories. These are: visual (delamination, soiling, and browning), thermal (hot spot) and electrical (current-voltage measurement). Visual and thermal approaches need frequent monitoring of the PV array to observe thermal hot spots or colour changes in modules. These approaches require thermal cameras and other sophisticated equipment. The monitoring system that is proposed will detect faults based electrical methods since it only requires the measurement of electrical and environmental parameters as set out in Section 2.4.

Faults on PV modules can be classified into three main categories: installation faults, changes in electrical properties and accidental events [5]. Installation faults include unsuitable orientation and inclination or physical damage such as cracks that occurred during the installation process. Changes in electrical properties include electrical contact deterioration, solder bond failures and electrochemical corrosion. Accidental faults include shading, dust collection (soiling), anomalous ageing and manufacturer mismatches.

The aim of the fault detection model is to detect when a fault on a PV module is present and to what extend the module is under-performing due to the fault. The fault detection model does not detect the cause of a specific fault.

3.3.1 Measured and Estimated Efficiency

The fault detection model works on the principle of measured and estimated efficiency. Faults cause efficiency losses within a PV module. Efficiency losses within a PV module can be detected by comparing the measured and estimated efficiency.

Measured efficiency is defined as the ratio/portion of energy in the form of sunlight that is converted into electricity. Measured efficiency is calculated as follow:

$$\eta_{Measured} = \frac{I_{Measured} \cdot V_{Measured}}{G \cdot A_C} \tag{3.1}$$

Where:

$I_{Measured}$ = Measured Module Current (A)

Stellenbosch University https://scholar.sun.ac.za

$V_{Measured}$ = Measured Module Voltage (V)

G = Measured Irradiance (W/m^2)

A_C = Area of the PV collector (m^2)

Estimated efficiency is the nominal panel efficiency as stated by the module manufacturer that is adapted for conditions other than the stated STC (Standard Test Conditions). Estimated efficiency is calculated as follow:

$$\eta_{Estimated} = \eta_{STC} \cdot (1 + \alpha_{MP} \cdot \Delta T) \tag{3.2}$$

Where:

η_{STC} = The Efficiency of the Specific Module at STC (%)

α_{MP} = Maximum Power Temperature Coefficient ($\%/°C$)

ΔT = Difference between STC Temperature and the Operating Temperature ($°C$)

The maximum power temperature coefficient is usually available in the PV module specifications. The maximum power temperature coefficient is used to estimate the effect of temperature on the power output on a PV module.

The efficiency of a PV module at STC can be calculated as follow:

$$\eta_{STC} = \frac{P_{MP}}{G_{STC} \cdot A_C} \tag{3.3}$$

Where:

P_{MP} = The Maximum Power Output of the Specific Module at STC (W)

STC conditions are defined by: $T_{STC} = 298.15K$, $G_{STC} = 1000W/m^2$ and air mass equal to 1.5.

The efficiency loss of a PV module can thus be calculated as:

$$\eta_{Loss} = \eta_{Estimated} - \eta_{Measured} \tag{3.4}$$

A threshold value (κ_{Th}) is used to balance the measured and estimated efficiency for real world applications. Factors that cause an imbalance include the specific installation site, uncertainties in the estimation of $\eta_{Estimated}$ and $\eta_{Measured}$ and uncertainties in temperature, irradiance, voltage and current measurements.

The threshold value is user-defined and is used to create a set-point or base value that describes a 'healthy' or normal operating module within a specific PV installation. Theoretically the threshold value can be calculated by:

$$\kappa_{Th} = \eta_{Estimated} - \eta_{Measured(Healthy)} \tag{3.5}$$

Stellenbosch University https://scholar.sun.ac.za

The efficiency loss for a PV module that is adapted for a specific application can be calculated as:

$$\eta_{Loss} = \eta_{Estimated} - \eta_{Measured} + \kappa_{Th} \tag{3.6}$$

If there is an efficiency loss calculated on a specific module it implies that the module is not operating normally and that there is a fault present. An efficiency loss value of zero or close to zero indicates a healthy module. If the efficiency loss value is low there might be a minor fault present. These faults include: partial shading, soiling, ageing and mismatches. If the efficiency loss value is high there might be a critical fault present. These faults include: complete shading, electrical failures (earth leakage, over current, over voltage) and damaged modules.

The fault detection model thus uses measurement data, manufacturer data, STC data and a user-defined threshold to calculate an efficiency loss value that indicates the health status of a specific module and whether a minor or critical fault is present.

3.4 System Design

3.4.1 Overall System

Figure 3.1 illustrates a diagram of the measurement system. The measurement system consists of wireless sensor nodes, a gateway, a database on a cloud server, and a GUI. LoRa was chosen as the wireless technology due to its low-power, long range, adequate data rates and ability to create a private star or mesh network as mentioned in Section 2.5.6.2.

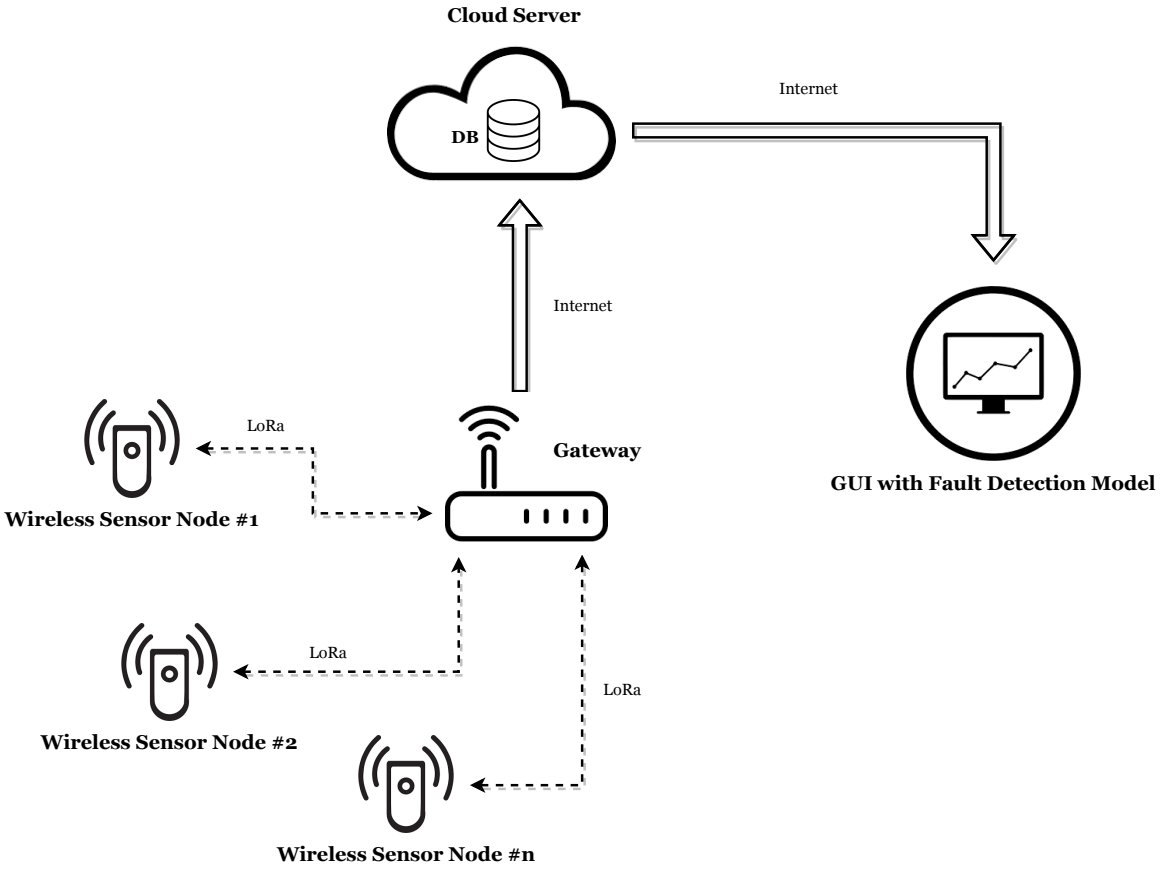

Figure 3.1: Measurement System Diagram

Stellenbosch University https://scholar.sun.ac.za

3.4.2 Wireless Sensor Node

Figure 3.2 illustrates the diagram of a wireless sensor node. The electrical and environmental quantities required to evaluate the performance of the PV module as set out in Section 2.4 (with some additional quantities), are gathered by a microcontroller which is sent to the gateway via a LoRa wireless transceiver.

The additional quantities that can be measured are ambient temperature, orientation and tampering detection. Ambient temperature is added to provide more insight into module backside temperature and how these two quantities differ for different environmental conditions. Orientation is added to provide a better insight into irradiance readings specifically for single- and two-axis tracking systems. Tampering is added to detect theft attempts or mechanical striking on PV modules.

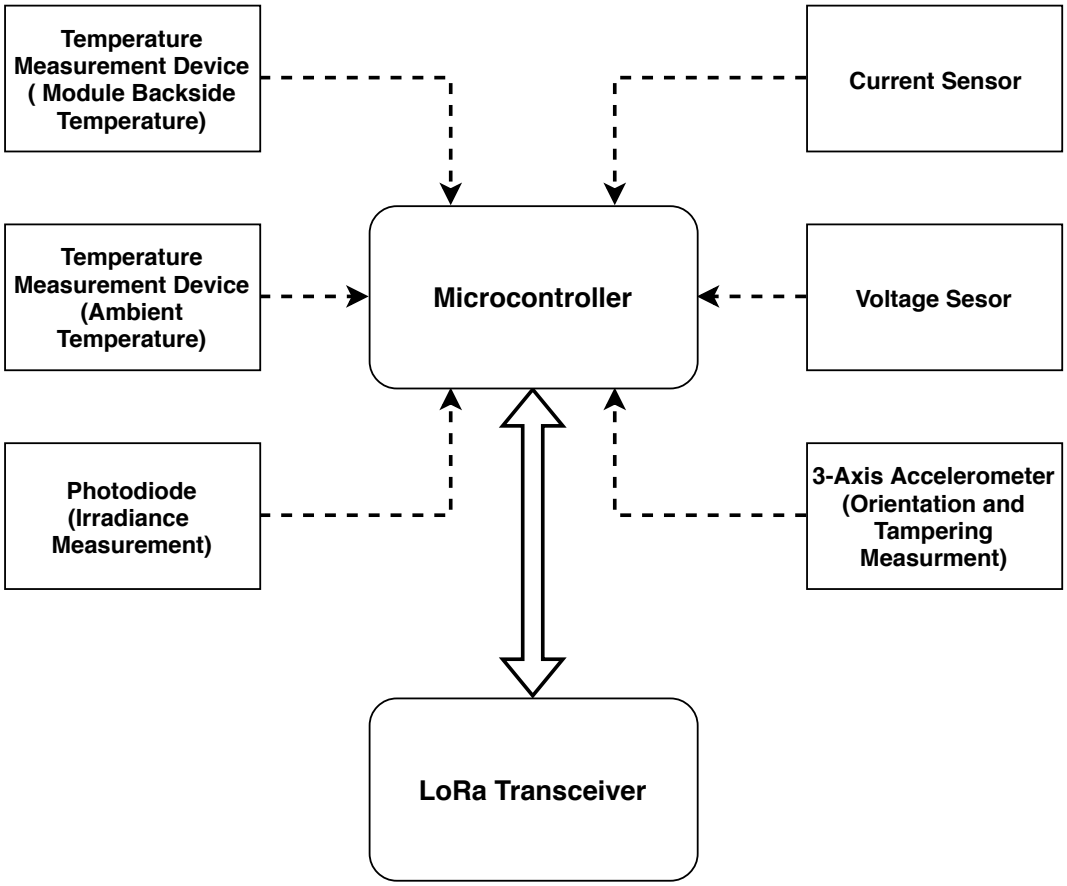

Figure 3.2: Wireless Sensor Node Diagram

3.4.3 Gateway, Cloud and GUI

A diagram for the gateway, the cloud and a GUI application is shown in Figure 3.3. A computer that is based on the same site as the wireless sensor nodes receives measurement data via a LoRa transceiver. The computer then publishes the measurement data into a database that is stored on a cloud server via an Internet connection (Wi-Fi or Ethernet). The data can be retrieved from the cloud server by another computer that can be anywhere with a Internet connection. The data is then accessed by a GUI application that analyses and displays the data.

Stellenbosch University https://scholar.sun.ac.za

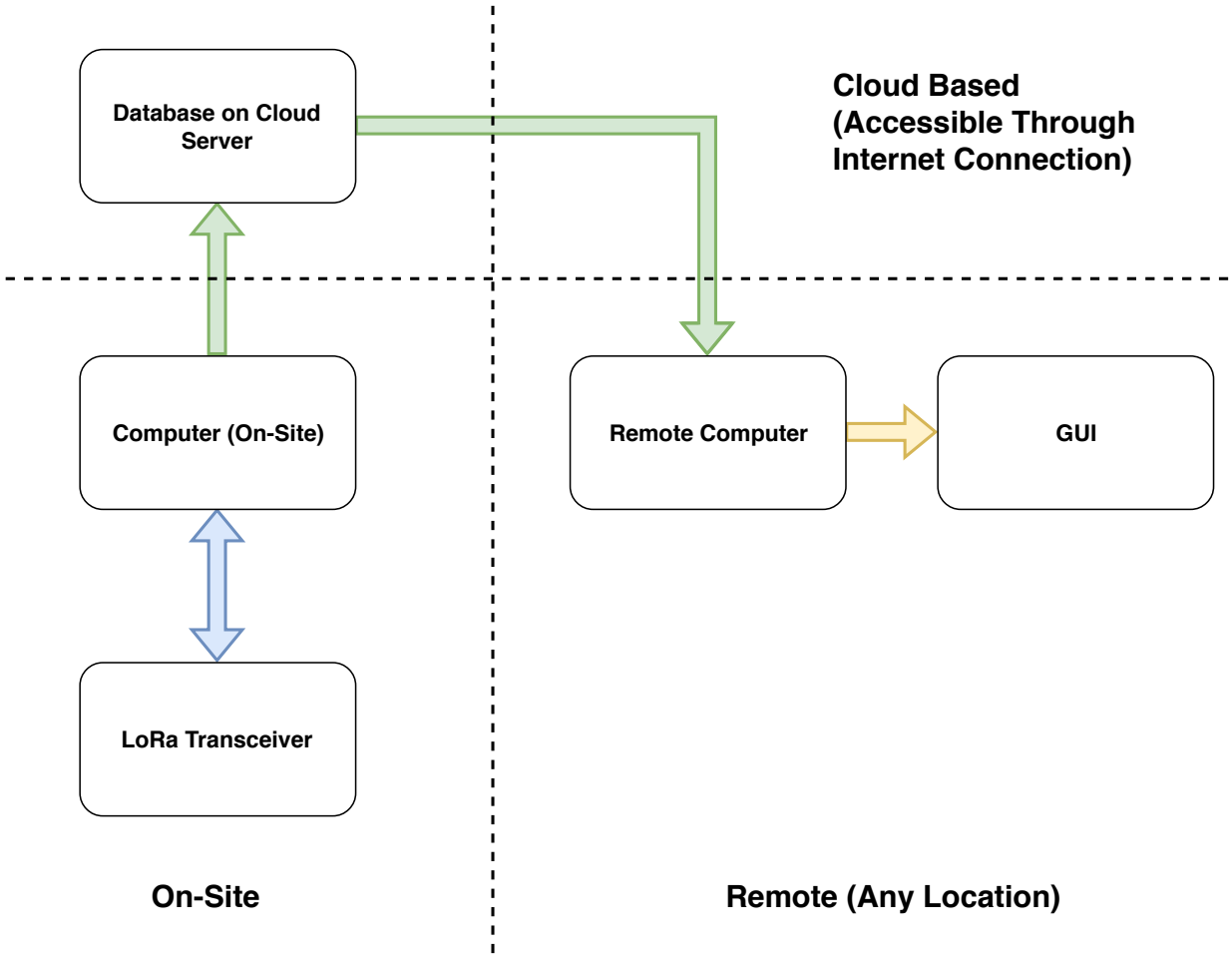

Figure 3.3: Gateway, Cloud and GUI Diagram

Stellenbosch University https://scholar.sun.ac.za

Chapter 4

Hardware Design of Monitoring System

4.1 Chapter overview

In this chapter the hardware design of the sensor nodes and a gateway is discussed. The hardware designs are based on the system design presented in Chapter 3. There are three different sensor versions and one gateway version. A complete breakdown of the different sub-sections for each sensor node version and gateway is presented along with component selection, design parameters, circuit design and preliminary measurement results.

4.2 Measurement Information and Requirements

The sensor nodes' measurement requirements are based on the electrical specifications of a 320 W polycrystalline PV module. The electrical specifications of a ARTsolar ART320-72 is presented in Table 4.1. This specific module is installed on a PV site in Stellenbosch, South Africa. This site served as the main test site for the monitoring system.

Table 4.1: ARTsolar ART320-72 Electrical Specifications

Item	ART320-72
Maximum Power (Pmax)	320 Wp
Voltage at Maximum Power (Vmpp)	37.5 V
Current at Maximum Power (Impp)	8.53 A
Open Circuit Voltage (Voc)	46 V
Short-Circuit Current (Isc)	9.5 A

The electrical specifications presented in Table 4.1 serve as a guideline for the magnitude of the different electrical quantities that the sensor nodes need to measure. The electrical and environmental quantities that each sensor node is required to measure as set out in Section 3.4.2 are:

- Module Voltage
- Module Current
- Irradiance
- Module Backside Temperature
- Ambient Temperature

Stellenbosch University https://scholar.sun.ac.za

- Orientation and Tampering Detection

4.2.1 Electrical Connection

Each sensor node is designed to have an electrical connection with the module that it measures. A series connection is required to measure module current and a parallel connection is required to measure module voltage. The connectors used are the industry standard MC4 connectors. These connectors are used on the ART320-72 among other PV modules.

Figure 4.1 illustrates how PV modules are connected to form a string in a typical solar installation (top) and how PV modules are connected to form a string in a solar installation when there is a sensor node present on each module (bottom) that requires a series and parallel connection.

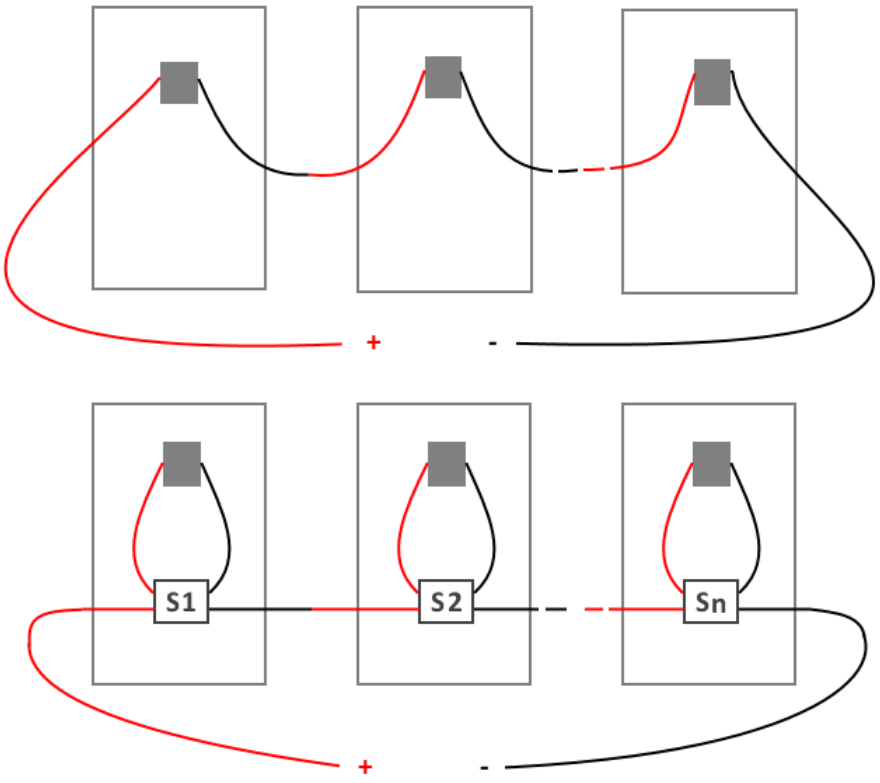

Figure 4.1: Connection Diagram of a normal Solar String (top) and a Solar String with Sensor Nodes having a Series and Parallel Connection (bottom).

There are two PCB (Printed Circuit Board) terminal blocks that connect the MC4 connectors to the sensor node circuitry. One terminal block is used to connect the input and the output of the positive (red) terminal of the PV module and the other terminal block is used to connect the negative (black) input and output of the PV module. The MC4 connectors are connected to the PCB terminal blocks via a piece of solar cable. Three sizes of solar cable are commonly used in solar installations, namely: 6 mm^2 70 A, 4 mm^2 55 A, and 2.5 mm^2 41 A cables.

The PCB terminal block used on all versions of the sensor nodes is the Phoenix Contact COMBICON GMKDS Series, 7.62 mm Pitch Straight, Through Hole, 2 Way, PCB Terminal

Stellenbosch University https://scholar.sun.ac.za

Block [32]. The terminal block has a current rating of 30 A and a voltage rating of 1000 V. 4 mm^2 solar cable is used to connect the MC4 connectors to the PCB termination blocks.

4.3 Sensor Node Versions

Three sensor node versions were designed, built and tested. The evolution and differences between the versions are depicted in Table 4.2. A detailed discussion with component selection, circuit design and measurement results for the various aspects of each sensor node version is presented in Sections 4.4, 4.5 and 4.6.

Table 4.2: Sensor Node Version Changes

Category	Description	V1	V2	V3
Power	From Measured PV Module	✓		
	4 x NiMH AA Batteries + 0.5 W PV Module		✓	
	18650 Li-ion Battery + 0.5 W PV Module + Charge Controller			✓
Operating Voltage	5 V	✓		
	3.3 V		✓	✓
Microcontroller	Arduino Nano	✓		
	ATmega328P		✓	✓
LoRa Transceiver	DRF1278	✓		
	RFM98		✓	✓
Voltage Measurement	Linear Optocoupler	✓		
	Digitally Isolated ADC		✓	✓
Current Measurement	Hall-Effect Sensor (100mV/A Sensitivity)	✓		
	Hall-Effect Sensor (264mV/A Sensitivity)		✓	✓
Irradiance Measurement	Photo-diode (photo-current-to-voltage)	✓	✓	✓
Temperature Measurement (Ambient)	Analog Temperature Sensor (10 mV/°C)	✓	✓	✓
Temperature Measurement (Module)	Digital Thermometer (10-bit True Reading)	✓	✓	✓
Orientation & Tampering	±1.5g 3-Axis Accelerometer	✓	✓	
	±6g 3-Axis Accelerometer			✓
Enclosure	No Enclosure	✓		
	3D Printed Enclosure		✓	
	IP66 Waterproof Enclosure			✓

4.4 Sensor Node Version 1

Version 1 of the sensor node serves as a proof of concept idea with no field trails in mind. This version aims to integrate, test and verify the different sub-systems that make up the sensor node.

Stellenbosch University https://scholar.sun.ac.za

4.4.1 Power

Sensor node Version 1 is powered from the PV module that it measures. According to Table 4.1 the sensor node input voltage can go as high as 46 V, The sensor node circuitry requires 5 V DC as input voltage. A voltage regulator (DC-DC converter) is required to bring the PV module voltage down to 5 V to power the sensor node circuitry. There are two types of voltage regulators than can do this, a linear regulator and a switching regulator.

A linear regulator has a low input voltage range and should not be used if there is a big difference between the input and output voltage The difference between the input voltage and regulated output voltage is continually dissipated as heat, making the regulator inefficient. The power dissipated as heat can be calculated as:

$$P_{diss} = [V_{in} - V_{out}] \cdot I \tag{4.1}$$

A switching regulator has a wide input voltage range and can be used for various input and output voltages with high efficiency. Switching regulators are further divided into isolated and non-isolated. To protect the sensor node circuitry from high voltages which are generated by solar panels it was chosen to use an isolated switching regulator to power the sensor node.

The isolated DC-DC converter that is used for the sensor node power supply is the NCS3S-4805SC from Murata Power Solutions Inc. The device has an input voltage range of 18 - 75 V with a nominal input voltage of 48 V [33]. It features 1.5 kVDC isolation 'Hipot Test' (1.5 kVDC for 60 seconds) with continuous short-circuit protection. The converter has an output voltage of 5 V and a minimum load requirement of 5%. It is rated at 3 Watt with a maximum output current of 600 mA. It has a minimum efficiency of 77.5% and a typical efficiency of 80%. It has a maximum load regulation of ±1% which means that the output voltage will change by a maximum of ±1% over the supply's load current range (30 mA - 600 mA).

The circuit design of the isolated DC-DC converter can be seen in Figure 4.2. There is a 10 μF ceramic capacitor placed across the output which is recommended in the device data sheet for a smooth output voltage. Note also a 5.1 V Zener diode placed over the output voltage to prevent the voltage from exceeding 5.1V that may occur when the load is less than the required 5%.

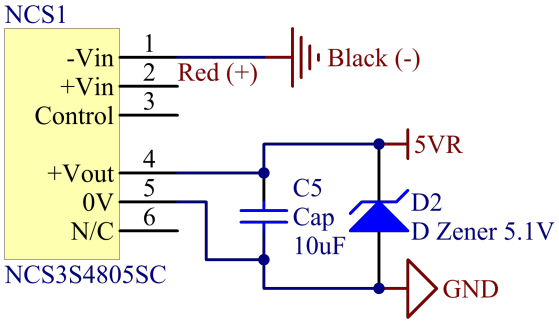

Figure 4.2: Power Supply Sensor Node Version 1 Circuit Design

4.4.2 Microcontroller

An Arduino Nano v3.0 serves as the microcontroller for the sensor node. The Arduino Nano is a small, complete board based on the ATmega328 and has a clock speed of 16

Stellenbosch University https://scholar.sun.ac.za

MHz. The ATmega328 is a high performance 8-bit AVR RISC based microcontroller with 32 KB flash memory, 1 KB EEPROM, 2 KB SRAM amongst other features [34]. The Arduino Nano v3.0 is used for sensor node Version 1 because it is plug-and-play and easy to program using the Arduino programming language (based on Wiring) and the Arduino development environment(based on Processing). Arduino has a lot of public support and is a well developed and supported platform for developing various products and applications.

The Arduino Nano is used to receive inputs from a variety of sensors and circuitry, convert those inputs, and send them via a LoRa radio transceiver to a central gateway. These inputs include voltage, current, temperature, irradiance and inertial measurements. An image of the Arduino Nano is shown in Figure 4.3.

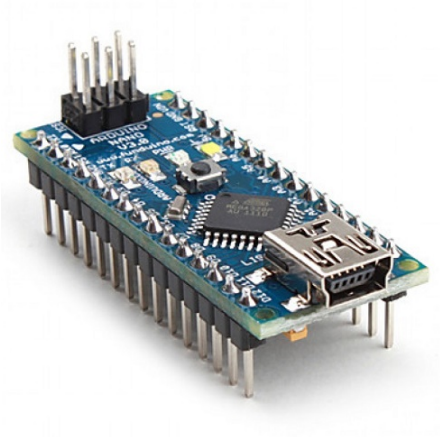

Figure 4.3: Arduino Nano v3.0 ATmega328 Board

4.4.2.1 Power

The Arduino Nano can be powered via the Mini-B USB connection, 6-20 V unregulated external power supply, or 5 V regulated external power supply [34]. There is no Mini-B USB connection to draw power from when the sensor node is installed on a PV module. The maximum voltage of a PV module is higher than the allowed unregulated external supply limit of 20 V. The Arduino Nano is powered via the 5 V regulated power supply which is supplied by the isolated DC-DC converter discussed in Section 4.4.1. The 5 V output voltage of the isolated DC-DC converter is further referred to as the main 5 V supply.

4.4.2.2 Input and Output Pins

The Nano has 14 digital I/O (Input/Output) pins. Each of the 14 digital pins can be used as input or output, these pins operate at 5 V [34]. Each pin can provide or receive a maximum of 40 mA and has an internal pull-up resistor (disconnected by default) of 20 - 50 kΩ.

The Nano has 8 analog inputs, each of which provide 10 bits of resolution (1024 different values). By default they measure from ground to 5V though it is possible to change the upper range with a software function [34].

Pins with Specialized Functions: In addition to the normal use case of the digital I/O pins some pins have dedicated special functions. There are two pins used to receive (RX) and transmit (TX) TTL serial data. These pins are connected to the corresponding pins of the FTDI USB-to-TTL Serial chip. There are two pins for external interrupts. These pins can be configured to trigger an interrupt on a low value, a rising or falling edge, or a change

Stellenbosch University https://scholar.sun.ac.za

in value. There are six pins that can provide 8-bit PWM output. There are four pins (SS, MOSI, MISO and SCL) which supports SPI communication and there is a pin connected to a built-in LED [34].

In addition to the normal use case of the analog pins there are two pins (SDA and SCL) that support I^2C (TWI) communication using the Wire library [34].

4.4.2.3 Circuit Design

The circuit design of the Arduino Nano v3.0 used in sensor node Version 1 can be seen in Figure 4.4.

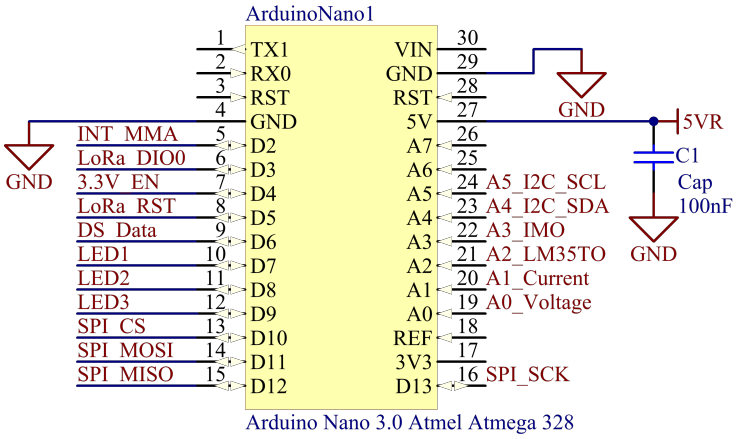

Figure 4.4: Arduino Nano (Microcontroller) Circuit Design

4.4.3 LoRa Radio Module

The LoRa radio module that is used used to send measurement data from the sensor node to a gateway is the DRF1278 LoRa transceiver. The module operates in the 433 MHz ISM (license free) band. The module can make use of a simple wire antenna, a U.FL or a SMA radio connector. An image of the DFR1278 LoRa transceiver is presented in Figure 4.5.

Figure 4.5: DRF1278 LoRa Radio Transceiver 433 MHz

The module is based on the SX1278 LoRa chip from Semtech Corporation. The module consists of the SX1278 LoRa module, a thin SMD crystal and antenna matching circuitry. The DRF1278 electrical specifications can be seen in Table 4.3 [35].

Stellenbosch University https://scholar.sun.ac.za

Table 4.3: DRF1278 Electrical Specifications

Symbol	Parameter (condition)	Min.	Typ.	Max.	Units
VCC	Supply Voltage	1.8	3.3	3.6	V
Temp	Operating Temperature Range	-40	25	80	°C
Freq	Frequency Range	410	433	460	MHz
IDD_R	Current in Receive Mode		12		mA
IDD_T	Current in Transmit Mode		120	125	mA
IDD_S	Current in Sleep Mode			1	μA
Pout	Maximum Output Power		20		dBm
Sen	Receiver Sensitivity @LoRa 300bps			-136	dBm
Z_{ANT}	Antenna Impedance		50		Ohm

4.4.3.1 Power

The module requires a power supply of 1.8 - 3.6 V. The module data sheet states that the power source of the module should be able to supply 150 mA peak [34]. A NCP700BSN33T1G 3.3 V, 200 mA, ultra low noise, LDO (Low Drop Out) linear voltage regulator is used to supply power to the radio module [36]. The voltage regulator is powered from the main 5 V supply.

The circuit design of the 3.3 V voltage regulator used to power the LoRa radio module can be seen in Figure 4.6. There is a 1 μF capacitor placed on the input and output of the voltage regulator as well as a 10 nF capacitor placed at the BYP (Bypass) pin to ensure low noise and a smooth voltage output. The voltage regulator has an EN (Enable) pin that connects to one of the Digital I/O pins of the microcontroller as seen in Figure 4.4. This pin is used to switch the voltage regulator on and off as necessary to save power.

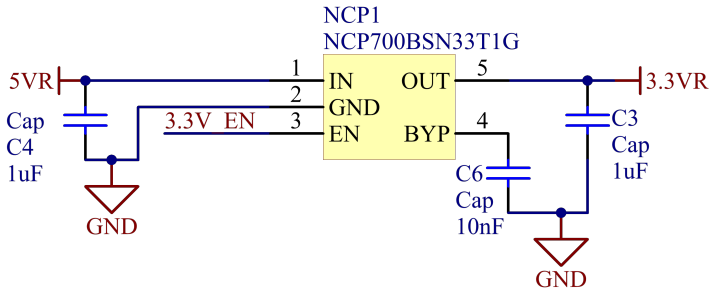

Figure 4.6: LoRa Radio Module Power Supply Circuit Design

4.4.3.2 Communication and Digital I/O Pins

The module communicates to a microcontroller, in this case an Arduino Nano, via SPI communication. SPI communication consists of 4 digital lines (MOSI, MISO, NSS and SCK).

The module has five digital I/O pins that are used to indicate different flags that occur in LoRa communication. For the sensor node the first digital I/O pin (DIO0) is used. This pin is is used to indicate when a LoRa message has successfully been sent or received [35].

All of the pins on the radio module operate on 3.3 V supplied by the 3.3 V voltage regulator. The microcontroller that these pins connect to, operate on 5 V. A bidirectional logic level

Stellenbosch University https://scholar.sun.ac.za

shifter is used to interface between each of the pins that are connected from the radio module to the microcontroller.

Each bidirectional logic level shifter uses a single N-channel MOSFET (BSS138TA N-Channel Logic Level Enhancement Mode Field Effect Transistor) and two pull-up resistors. A bidirectional level-shifting circuit design can be seen in Figure 4.7.

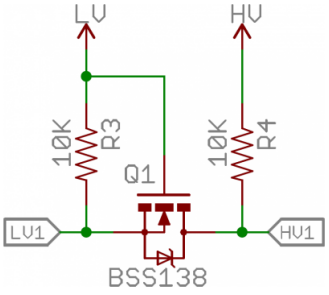

Figure 4.7: Bidirectional Logic Level-Shifting Circuitry

The circuit design for all of the digital lines (SPI, Reset and DIO0) that is connected between the radio module and the microcontroller can be seen in Figure 4.8. The level shifters convert between the main 5 V supply (5VR) and the 3.3 V regulated supply (3.3VR) supplied by the 3.3 V voltage regulator.

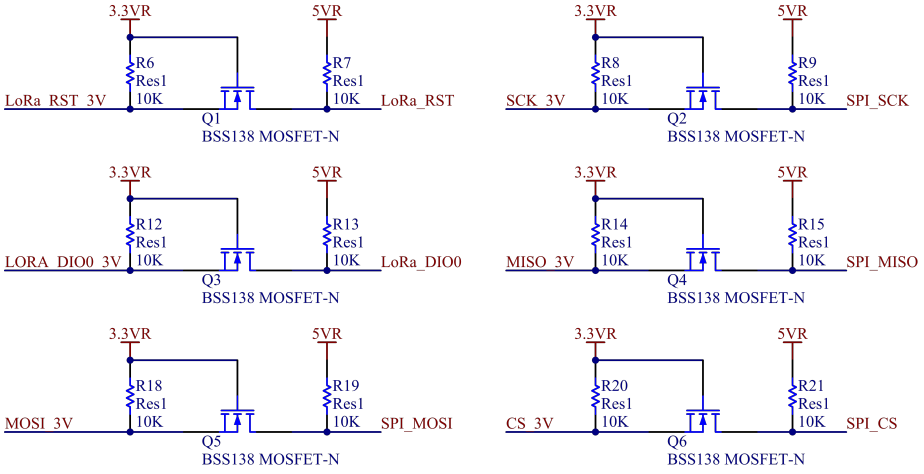

Figure 4.8: Level-Shifting Circuit Design for interface between LoRa Module and Microcontroller

4.4.3.3 Antenna

The DRF1278 has a pin (ANT) for connecting an external antenna. For the sensor node a female U.FL antenna connector is connected to the ANT pin. The antenna that connects to the female U.FL connector is a 433 MHz, Straight, Whip, 1/2 wave dipole, U.FL, 3.3 dBi antenna from Linx Technologies Inc [37]. The antenna has a height of 173 mm and a cable length of 216 mm [37]. The antenna can be seen in Figure 4.9.

Stellenbosch University https://scholar.sun.ac.za

Figure 4.9: 433 MHz, U.FL, 3.3 dBi Antenna

4.4.3.4 Circuit Design

The circuit design of the DRF1278 Radio Module can be seen in Figure 4.10.

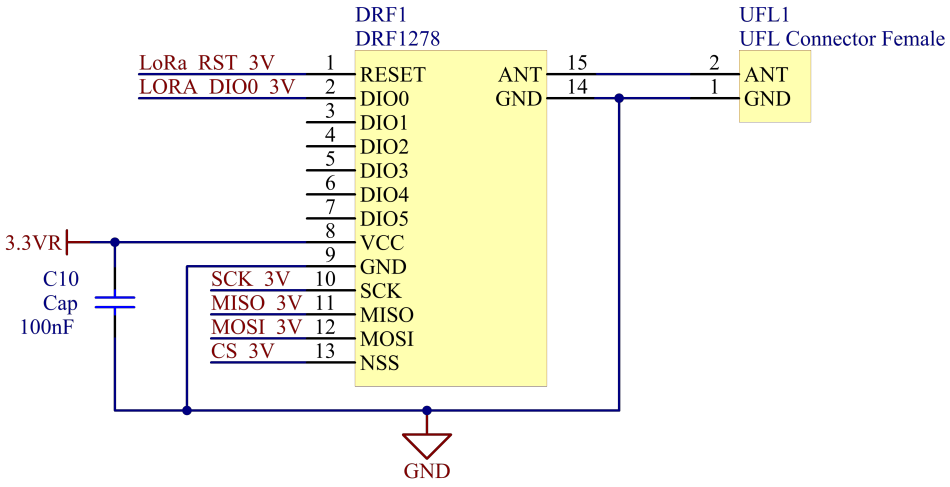

Figure 4.10: DRF1278 LoRa Radio Module Circuit Design

4.4.4 Voltage Measurement

The sensor node utilizes the linear optocoupler method mentioned in Section 2.4.1.2 to make voltage measurements. The linear optocoupler used is the IL300 from Vishay Semiconductors. The IL300 has 0.01% servo linearity (The ratio between the photo-diode current and the LED current) and a high gain stability of $\pm 0.005\%/°C$ [17]. The IL300 has a power consumption of < 15 mW with an isolation voltage of 5300 VRMS tested for 1 second. The LED in the IL300 is an infra-red emitter that emits at 890 nm and operates efficiently with a drive current from 500 μA to 40 mA. The IL300 data-sheet recommends a drive current between 5 mA and 20 mA for the best linearity.

4.4.4.1 Circuit Design

The voltage being measured by means of the optocoupler circuit range from 0 - 46 V according to Table 4.1. The first part of the voltage measurement circuitry is a voltage divider that

Stellenbosch University https://scholar.sun.ac.za

scales the input voltage (V_{mod}). With a safety margin added the circuit was designed to have an output voltage (V_a) of 4.5 V for a input voltage (V_{mod}) of 50 V. The voltage measurement circuit diagram can be seen in Figure 4.11.

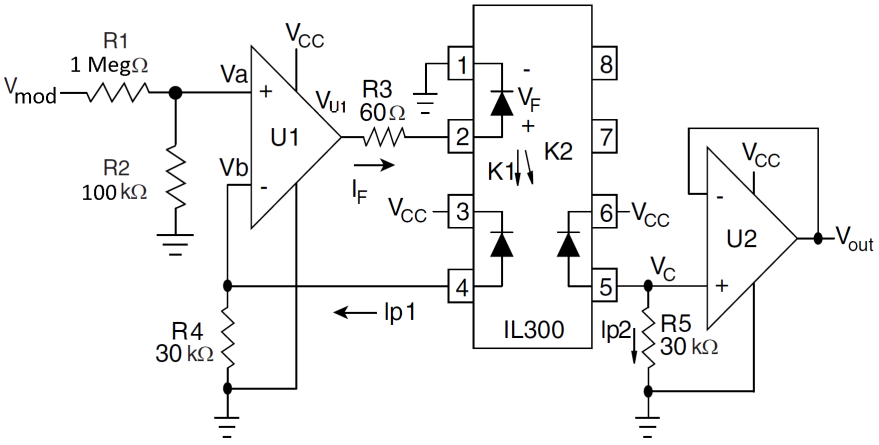

Figure 4.11: Voltage Measurement Circuit Diagram

Resistor R1 was chosen as 1 Mega-Ohm for low energy dissipation. The equation for resistor R2 can be written as:

$$R2 = \frac{R1 \cdot V_a}{V_{mod} - V_a} = \frac{1Meg\Omega \cdot 4.5V}{50V - 4.5V} \approx 100k\Omega \tag{4.2}$$

Resistor R4 creates voltage V_b through the current I_{P1}. R4 is calculated at a certain LED current (I_F). R4 was designed at the following conditions: The input voltage (V_a) is at a maximum (4.5 V) and the LED current (I_F) is 20 mA. The LED current (I_F) was chosen as 20 mA for the maximum input voltage, since 20 mA is the upper boundary for the best linearity - as mentioned in the device data-sheet [17]. The relationship between the LED current I_F and the photocurrent I_{P1} is shown in Figure 4.12 [17].

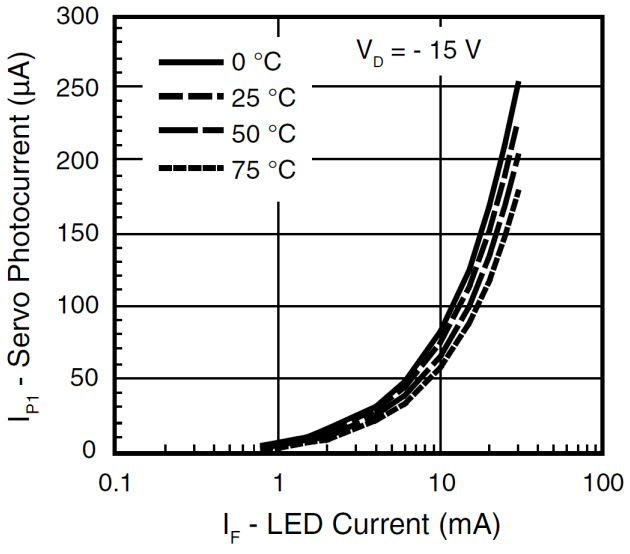

Figure 4.12: Photocurrent vs. LED Current for different Temperature values IL300

Stellenbosch University https://scholar.sun.ac.za

From Figure 4.12 it can be seen that the photocurrent I_{P1} will be $\approx$ 150 μA for a LED current I_F of 20 mA at room temperature. The equation for R4 can be written as:

$$R4 = \frac{V_b}{I_P 1} = \frac{V_a}{I_P 1} = \frac{4.5V}{150\mu A} = 30k\Omega \tag{4.3}$$

Resistor R5 is chosen to be the same value as R4 since the IL300 has a transfer gain (K2/K1) of $\approx$ 1 [17]. The output voltage (V_{out}) will thus theoretically be equal to V_b which is equal to V_a.

Resistor R3 is the LED current (I_F) limiting resistor. The output voltage of the Op-amp (V_{U1}) is targeted to be 50% of the supply voltage (Vcc), or 2.5 V when the LED current (I_F) is 20 mA and the input voltage (V_a) is 4.5 V. The Op-amp output voltage (V_{U1}) was chosen as 50% of the supply voltage because this is the voltage at which a single supply Op-amp delivers it's highest output current. The typical LED forward voltage (V_F) of the IL300 is 1.3 V as stated in the device data-sheet [17]. The equation for R3 can be written as:

$$R3 = \frac{V_{U1} - V_F}{I_F} = \frac{2.5V - 1.3V}{20mA} = 60\Omega \tag{4.4}$$

Components The operational amplifiers that are used in the voltage measurement circuitry are OPA347 rail-to-rail single supply operational amplifiers from Texas Instruments. The OPA347 has rail-to-rail input and output and operates from a single supply of 2.3 - 5.5 V. The input range of the OPA347 extends 200mV beyond the rails and the output range is within 5mV of the rails [38]. The OPA347 can source 25mA at an output voltage of 2.5V with a supply voltage of 5V.

An isolated power supply is required to power the 'high side' Op-amp. This is done with a CRE1S0505SC 1 Watt isolated DC-DC converter from Murata Power Solutions. The CRE1S0505SC has an input voltage of 4.5 - 5.5 V and an output voltage of 5 V. The device has a minimum isolation voltage of 1000 VDC and a maximum output current of 200 mA [39]. The circuit design of the isolated DC-DC converter can be seen in Figure 4.13. The DC-DC converter is powered by the main 5 V power supply. A capacitor is placed across the output for a smooth output voltage, while a Zener diode in the same position prevents the output voltage being higher than 5.1 V when the load on the DC-DC converter is less than 10% as stated in the device data-sheet.

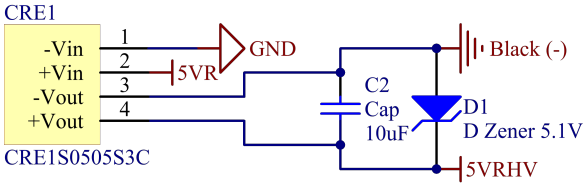

Figure 4.13: High Side Power Supply Circuit Design

The circuit design of the voltage measurement circuit can be seen in Figure 4.14 and 4.15. A capacitor C7 placed in parallel with resistor R3 to form a low-pass RC filter that filters out

Stellenbosch University https://scholar.sun.ac.za

high frequency and noise components from the measured input voltage. The -3 dB cut-off frequency of the RC filter is:

$$f_c = \frac{1}{2\pi RC} = \frac{1}{2\pi \cdot 100k\Omega||1Meg\Omega \cdot 100nF} = 17.5Hz \tag{4.5}$$

The rest of the circuitry is similar to the circuitry from Figure 4.11. The circuitry is split up into a 'High Voltage Side' (Figure 4.14) and a 'Low Voltage Side' (Figure 4.15) with the isolation barrier between the two sides being the IL300 linear optocoupler. On the 'High Voltage Side' Red(+) and Black(-) refer to the PV module positive and negative connections. The output of the voltage measurement circuitry (A0_Voltage) is connected to one of the analog input pins (A0) on the microcontroller as seen in Figure 4.4.

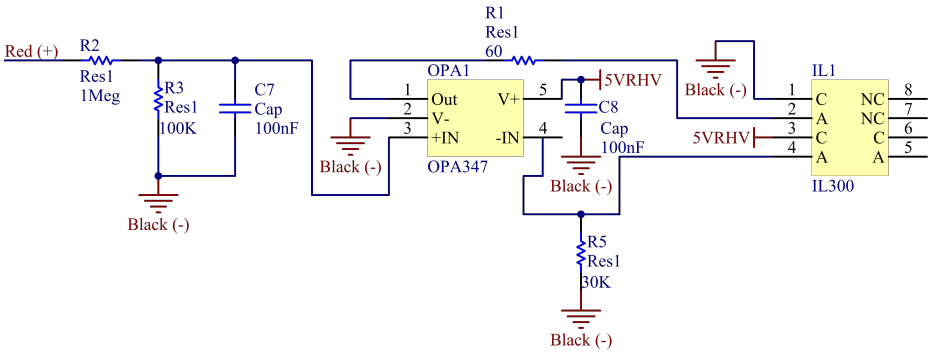

Figure 4.14: Isolated Voltage Measurement High Voltage Side Circuit Design

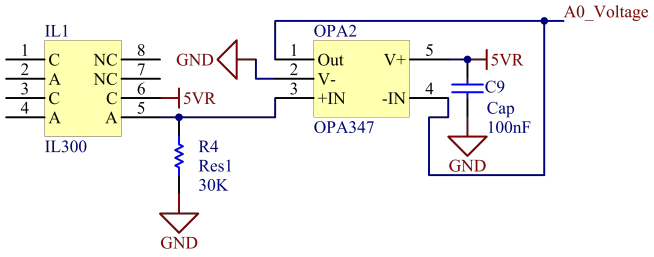

Figure 4.15: Isolated Voltage Measurement Low Voltage Side Circuit Design

4.4.5 Current Measurement

The sensor node makes use of the Hall-effect method described in Section 2.4.1.2 to measure current. According to Table 4.1 the PV module current can go as high as 9.5 A. A Hall-effect sensor is ideal for this application since it requires no additional isolated power supply and it works optimally with currents in the Ampere range.

The sensor node makes use of a ACS712 Fully Integrated, Hall-Effect Based Linear Current Sensor IC. The ACS712 has 2.1 kVRMS isolation between the input current and the output voltage and a low-resistance current conductor (1.2 mΩ) [40]. The ACS712 consists of a precise, low-offset, linear Hall circuit with a copper conduction path located near the surface of the die. Applied current flowing through this copper conduction path generates a magnetic field which the Hall IC converts into a proportional voltage. The ACS712 is powered from the main 5 V power supply. The device is rated to measure up to a maximum current of 20A and has a typical sensitivity of 100 mV/A.

Stellenbosch University https://scholar.sun.ac.za

The circuit design of the current measurement method can be seen in Figure 4.16. The two Phoenix GMKDS PCB Terminal Blocks are connecting terminal blocks from the PV module as described in Section 4.2.1. There is a 1 nF capacitor C13 placed between the Filter pin and ground for noise management as recommended in the device data-sheet [40]. The output voltage of the ACS712 (A1_Current) is connected to one of the analog pins (A1) of the microcontroller illustrated in Figure 4.4.

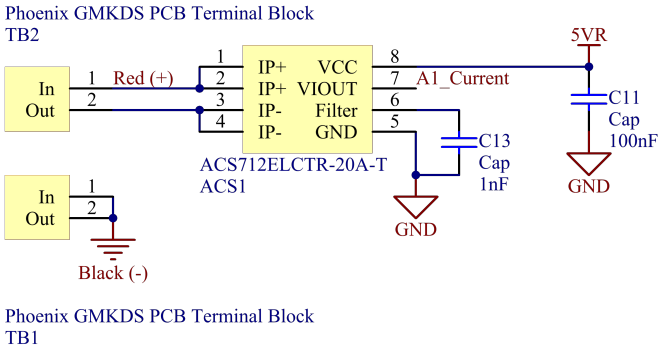

Figure 4.16: Current Measurement Circuit Design

4.4.6 Irradiance Measurement

Irradiance measurements are made with a photodiode and an operational amplifier by creating a photo-current-to-voltage converter circuit. For these measurements the photodiode requires to be in contact with direct sunlight. The photodiode used is a SFH203 Silicon PIN Photodiode.

The SFH203 photodiode has a wavelength range of 400 nm to 1100 nm, thus detecting infrared and visible light [41]. The radiant sensitive area is 1 mm^2 with a dimension (L by W) of 1 mm by 1 mm. The SFH203 has a typical photocurrent of 9.5 μA in Ev = 1000 lx, Standard Light with a reverse voltage of 5 V.

Figure 4.17 shows a photo-current-to-voltage converter circuit diagram using an operational amplifier as the amplifying device. The output voltage (V_{out}) is given as:

$$V_{out} = I_p \cdot R_f \tag{4.6}$$

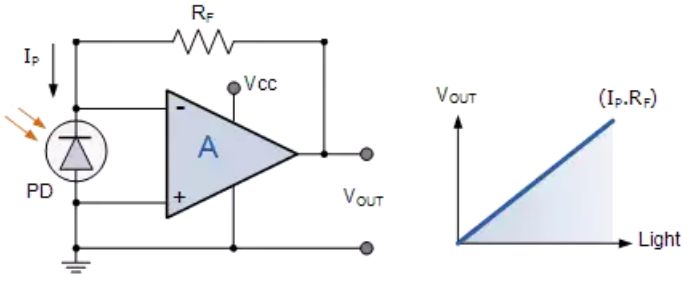

Figure 4.17: Photo-Current-To-Voltage Converter Circuit Diagram

The irradiance measurement circuit design can be seen in Figure 4.18. The output voltage (A3_IMO) is connected to one of the analog inputs (A3) on the microcontroller illustrated in Figure 4.4.

Stellenbosch University https://scholar.sun.ac.za

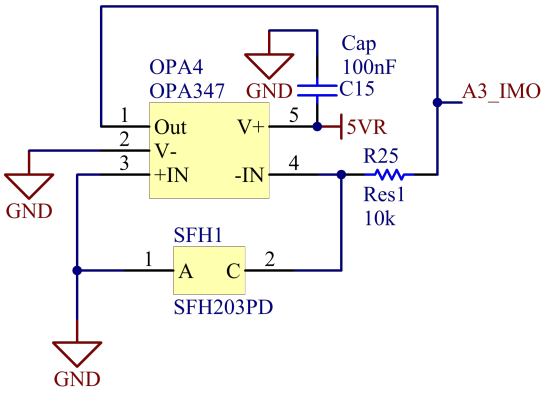

Figure 4.18: Irradiance Measurement Circuit Design

4.4.7 Temperature Measurement

4.4.7.1 Ambient Temperature

Ambient temperature is measured with a LM35 Precision Centigrade Temperature Sensor. The LM35 is linear with a 10 mV/°C scale factor and has 0.5°C ensured accuracy at room temperature [42]. The LM35 is an integrated-circuit temperature device with an output voltage linearly proportional to the centigrade temperature. When powered from a single voltage supply between 4V to 20V the LM35 can accurately measure temperatures in the range of 0°C to 100°C [42]. The LM35 is powered from the main 5 V power supply. The LM35 temperature sensor with an application circuit can be seen in Figure 4.19.

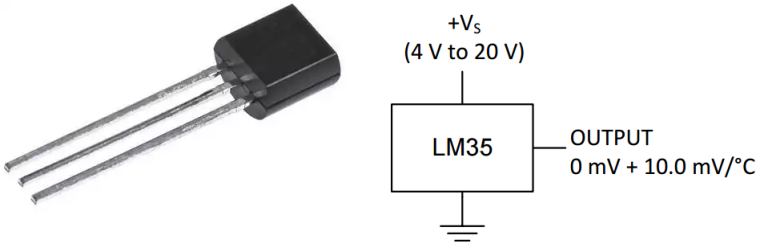

Figure 4.19: LM35 Temperature Sensor and Application Circuit

The LM35 has an output voltage of 0 mV + 10 mV/°C [42]. The output voltage of the LM35 will thus be 0V when the temperature is 0°C and 1 V when te temperature is 100°C. Because the Arduino Nano has a 10-bit ADC with an input range of 0 - 5 V a full range of 0 - 1 V for a temperature range of 0°C to 100°C will not have an optimal resolution. It was decided to amplify the output signal of the LM35 by a factor of 5 which results in an output voltage of 5 V when the LM35 is at the maximum measurable temperature (100°C). The output of the LM35 is amplified by a OPA347 Op-amp in a non-inverting amplification configuration. The ambient temperature measurement circuit design can be seen in Figure 4.20.

Stellenbosch University https://scholar.sun.ac.za

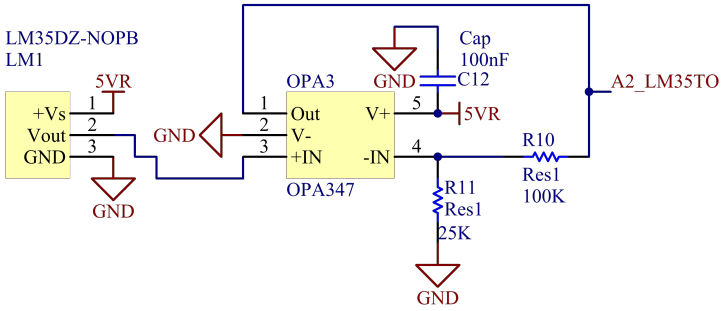

Figure 4.20: Ambient Temperature Measurement Circuit Design

When choosing resistor R10 as 100 kΩ and the ratio between the output and input voltage (Gain - A) as 5, the equation for resistor R11 can be written as:

$$R11 = \frac{R10}{A-1} = \frac{100k\Omega}{5-1} = 25k\Omega \tag{4.7}$$

The output of the operational amplifier (A2_LM35TO) is connected to one of the analog pins (A2) of the microcontroller as seen in Figure 4.4.

4.4.7.2 Module Backside Temperature

PV module backside temperature is measured using a digital thermometer IC. For these measurements the measuring IC is attached to the backside of the PV module. The digital thermometer used is the DS18B20 which is attached to a stainless steel temperature probe. The DS18B20 provides 9-bit to 12-bit Celsius temperature measurements via a 1-wire bus that requires only one data line and ground for communication [43]. It has an operating temperature range of -55°C to +125°C and is accurate to ±0.5°C over the range of -10°C to +85°C [43]. The DS18B20 sensor IC and temperature probe can be seen in Figure 4.21.

Figure 4.21: DS18B20 Thermometer and Temperature Probe

The circuit design of the DS18B20 thermometer can be seen in Figure 4.22. The DS18B20 is powered from the main 5 V power supply and the data line (DS_Data) is connected to one of the digital I/O pins (D6) of the microcontroller as seen in Figure 4.4.

Stellenbosch University https://scholar.sun.ac.za

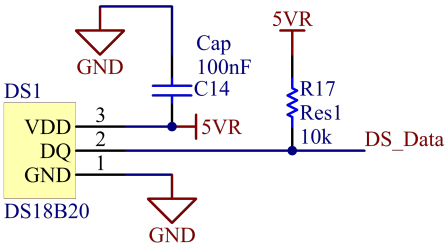

Figure 4.22: Module Backside Temperature Measurement Circuit Design

4.4.8 Orientation Measurement and Tampering Detection

The sensor node measures orientation and detects tampering with an accelerometer. The accelerometer used is the MMA7660FC 3-Axis Orientation/Motion Detection Sensor. The MMA7660FC is a ±1.5 g 3-Axis Accelerometer with digital output (I^2C) [44]. The device uses little power and gives 6-bit digital values at user configurable samples per second. The device has an interrupt pin for gesture detecting, product orientation and sensor data changes. The device operates on 3.3 V and is powered by the same 3.3 V voltage regulator that powers the LoRa radio module. The interrupt line and two I^2C lines (Data and Clock) are interfaced with the 5 V microcontroller via bi-directional logic level shifter circuitry. The circuit design of the bidirectional logic level shifters and the MMA7660FC accelerometer can be seen in Figure 4.23 and 4.24.

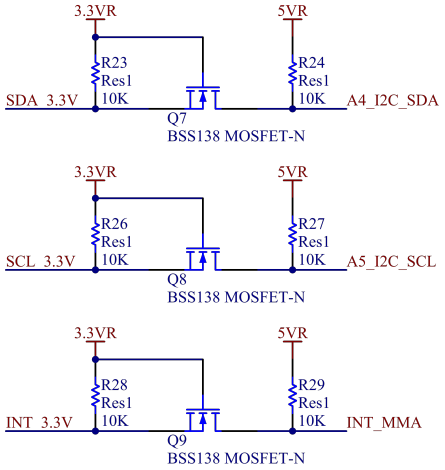

Figure 4.23: Level-Shifting Circuit Design for interface between MMA7660FC Accelerometer and Microcontroller

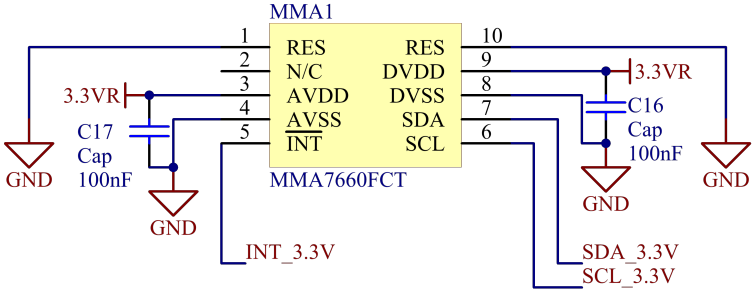

Figure 4.24: MMA7660FC Accelerometer Circuit Design

Stellenbosch University https://scholar.sun.ac.za

4.4.9 Assembled Sensor Node PCB

The PCB for sensor node Version 1 was constructed by means of a CNC (Computer Numerical Control) router. Figure 4.25 shows the assembled PCB and where various components are located. The two terminal blocks where Red (+) and Black (-) connect to, are on the bottom layer of the PCB and thus not visible on Figure 4.25.

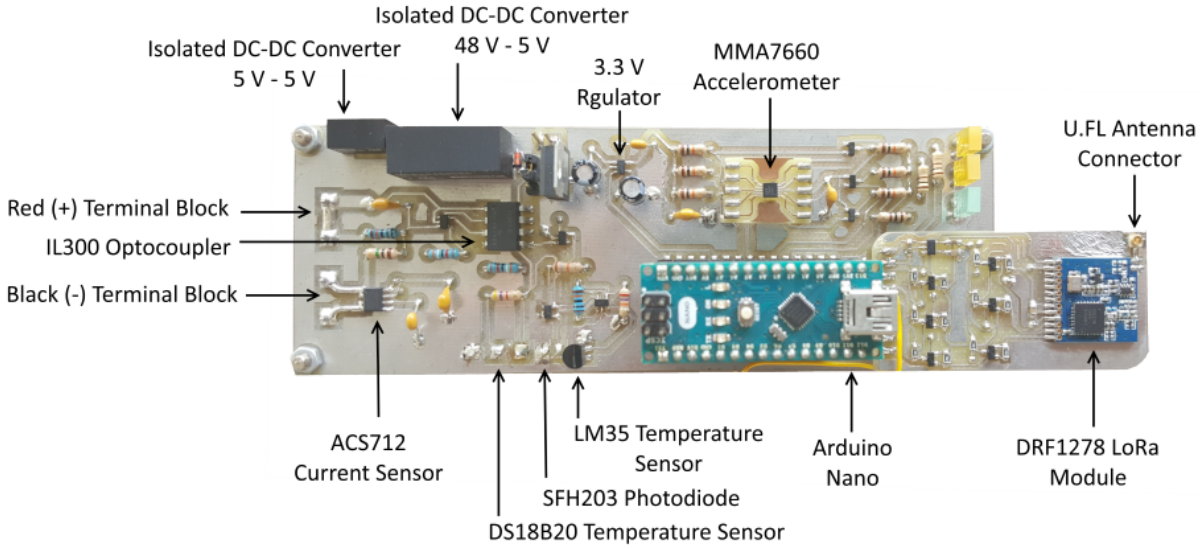

Figure 4.25: Sensor Node Version 1 Assembled PCB

4.4.10 Sub-System Evaluation

Sensor node Version 1 was designed to evaluate the operation of the different sub-systems that the sensor consists of. The different sub-systems were integrated and evaluated. The power supply operated within the parameters specified in the device datasheet [33]. The microcontroller was programmed to read the values from the different analog and digital sensors. These values were converted to their respective 'true' values by means of calibration constants. The LoRa radio module and microcontroller were successfully integrated and data packets were sent and received to and from another LoRa radio module.

4.4.10.1 Voltage Measurement

A graph of the input voltage and measured voltage that were carried out in a lab set-up is shown in Figure 4.26. The input voltage was supplied by an adjustable DC power supply and ranges from 2.5 V - 30 V. The input voltage was connected to the positive and negative terminal blocks marked Red (+) and Black (-) on Figure 4.25. The output voltage was measured on analog pin A0 of the microcontroller.

Stellenbosch University https://scholar.sun.ac.za

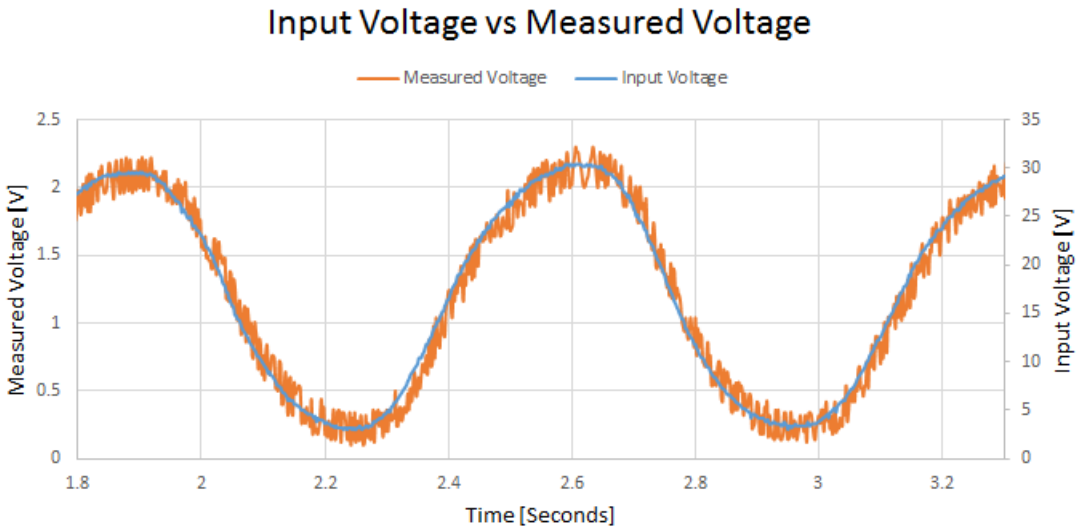

Figure 4.26: Input Voltage vs Measured Voltage

Figure 4.26 illustrates a linear relationship between the input 'high side' voltage and the isolated measured 'low side' voltage. This figure confirms that the linear optocoupler is operating in the manner that was theoretically calculated in Section 4.4.4. There is noise on the measured voltage that can be filtered out with a software filter by means of multiple sample averaging. After software filtering was applied the voltage measurement resolution was measured at 0.1 V with an accuracy of 0.5 V.

4.4.10.2 Current Measurement

Figure 4.27 depicts a graph of the input current and measured voltage. The input current was supplied by an adjustable DC power supply and was measured with a current probe. The input current ranges from 0 A - 6 A. The output voltage which is supplied by the ACS712 Hall-Effect Based Linear Current Sensor IC, as discussed in Section 4.4.5, was measured on analog pin A1 of the microcontroller.

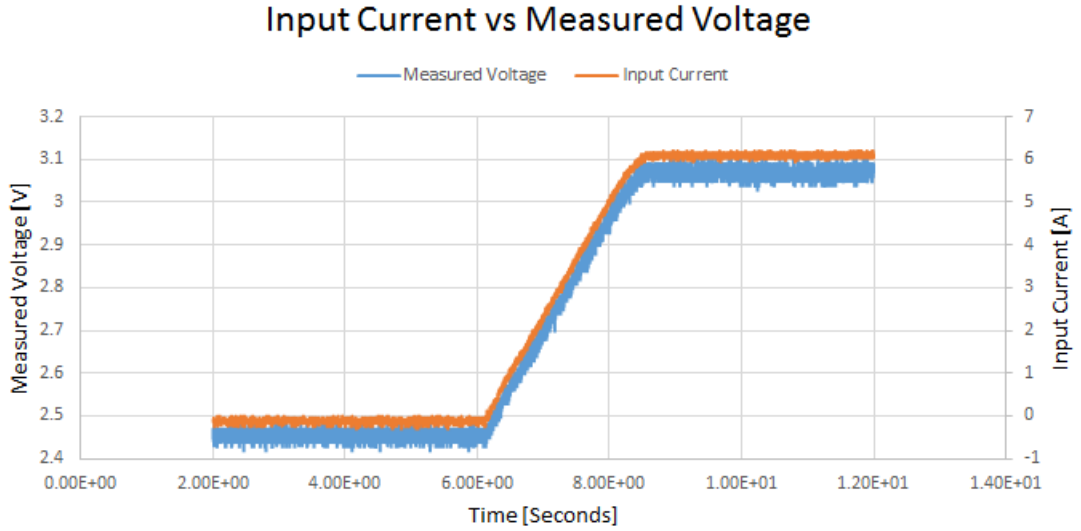

Figure 4.27: Input Current vs Measured Voltage

Stellenbosch University https://scholar.sun.ac.za

Figure 4.27 confirms a linear relationship between the input current and the isolated measured voltage. The current sensor measures at a resolution of 0.05 A with a total output error of ±1.5% as stated in the device datasheet [54]. The current sensor is thus capable of measuring isolated PV module current with a good accuracy.

4.4.10.3 Irradiance Measurement

Figure 4.28 and Figure 4.29 show graphs of irradiance measurements over the period of 1 day for a reference irradiance sensor and the irradiance sensor on sensor node Version 1.

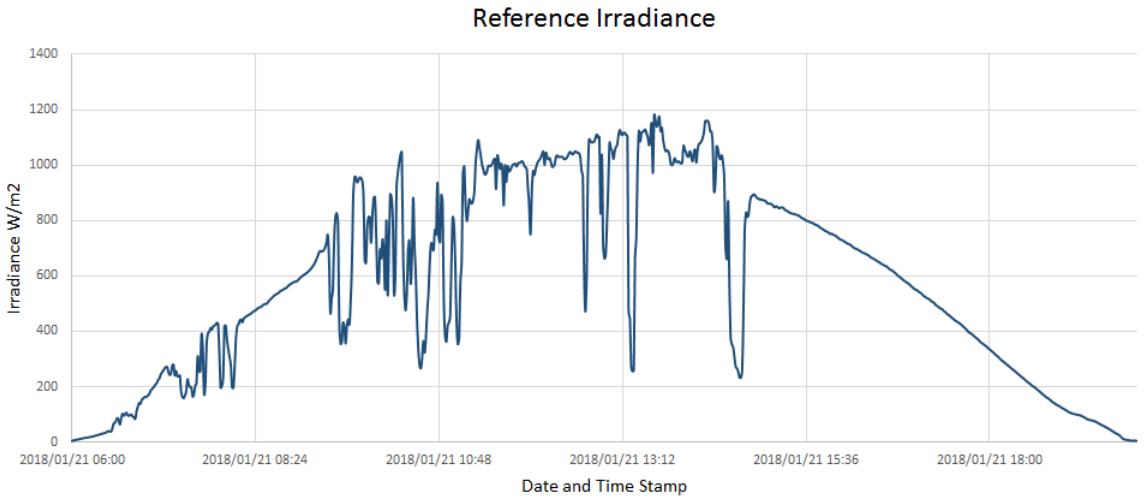

Figure 4.28: CMP11 pyranometer GHI Measurements for 1 day

The reference irradiance sensor is located in a solar resource measurement station, known as 'Sonbesie', which is situated on the rooftop of the Engineering Faculty at the University of Stellenbosch, South Africa. The reference irradiance sensor is a CMP11 pyranometer from Kipp & Zonen that provides GHI (Global Horizontal Irradiance) measurements [45]. GHI measurements are a sum of both the direct and diffuse components of solar irradiance. The measurements shown in Figure 4.28 were taken on the 21st of January 2018 from 06:00 am to 20:00 pm. Measurements were taken at 1 minute intervals.

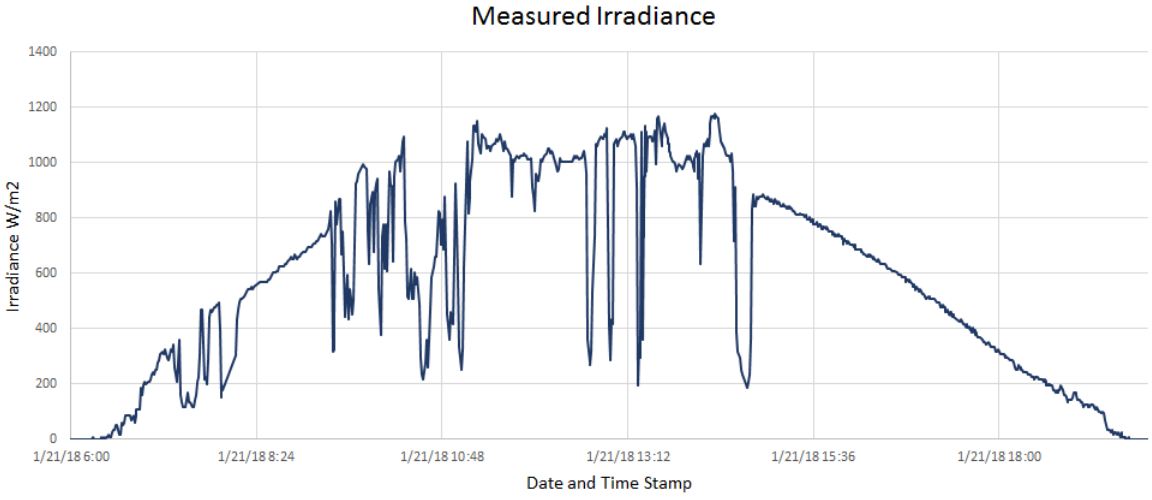

Figure 4.29: Sensor Node Version 1 Irradiance Measurements for 1 day

Stellenbosch University https://scholar.sun.ac.za

The irradiance measurements shown in Figure 4.29 was taken over the same period on 1 January 2018. The sensor node was placed on an adjacent rooftop close to the reference irradiance sensor. Irradiance was measured by means of a photodiode as discussed in Section 4.4.6. The photodiode was placed with the photo-collector horizontally orientated, thus measuring GHI. Measurements were taken at 1 minute intervals. The values presented in Figure 4.29 are voltage readings from analog pin A3 on the microcontroller that has been converted to true irradiance values by means of a calibration constant.

There is a clear correlation between Figure 4.28 and Figure 4.29. Some values differ due to the reading not occurring on the exact time and due to the fact that the two sensors were not located on the exact same location. The overall shape of the two figures proves that the photodiode measurement technique discussed in Section 4.4.6 provides accurate irradiance readings compared to an expensive industry standard irradiance sensor.

4.4.10.4 Temperature Measurement

Figure 4.30 illustrates ambient and module temperature readings that were taken over the course of 1 day at 1 minute intervals. The ambient temperature sensor is located on the sensor node circuitry and the module backside temperature sensor was attached to the backside of a working PV module on a PV test site located on the rooftop of the Engineering Faculty.

The LM35 ambient temperature sensor provides a voltage output that is linearly proportional to the temperature on analog pin A2 on the microcontroller as discussed in Section 4.4.7.1. The output voltage was converted to true temperature by means of a calibration constant. The DS18B20 sensor provides a digital true temperature value which is read on digital pin D6 as discussed in Section 4.4.7.2. Both temperature sensors measured within the resolution and accuracy specifications presented in their respective data sheets [42] and [43].

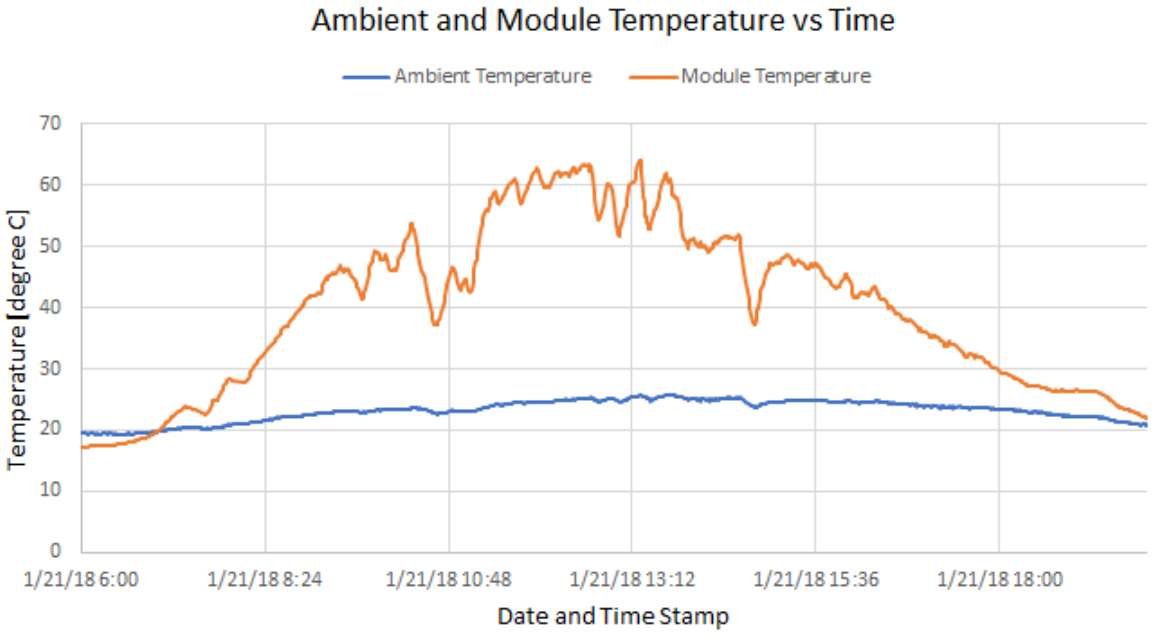

Figure 4.30: Ambient and Module Temperature Measurements for 1 day

Stellenbosch University https://scholar.sun.ac.za

4.4.10.5 Orientation Measurement and Tampering Detection

The accelerometer was interfaced with the microcontroller and orientation and tampering test were done. The accelerometer used as described in Section 4.4.8 produces a 6-bit result that can be converted to either the g value, X-axis angle, Y-axis angle or Z-axis angle. The 6-bit result ranges from 0 to 63 and provides g measurements from 0 g to 1.453 g with a resolution of 0.047 g. The result also provides the X, Y and Z-axis angles with a resolution of 2.7 degrees.

The accelerometer's tampering detection function was also tested. An interrupt pin connected to the microcontroller gets activated when an impact on the accelerometer greater than a user defined threshold is detected. It was found that the accelerometer is sensitive to small impacts since it only measures up to 1.5 g.

4.4.11 Power Consumption

The power consumption of sensor node Version 1 is presented in Table 4.4. The input voltage of the sensor node when the measurements were taken was 30V.

Table 4.4: Sensor Node Version 1 Power Consumption

Quantity	Idle Mode	Measurement Mode	Transmit Mode
Current	17.6 mA	23.5 mA	30.7 mA
Power	528 mW	705 mW	921 mW

The sensor node is in idle mode between measurement sets, for the duration of the interval between measurements. In this mode the microcontroller (Arduino Nano) and the LoRa transceiver is placed in sleep mode. In measurement mode the sensor node collects the measurement data from the various analog and digital sensors and constructs the LoRa message. Transmit mode is when the sensor node transmits measurement data to the central gateway. This mode has the highest power consumption.

4.5 Sensor Node Version 2

Version 2 of the sensor node serves as an improvement of the various sub-systems that were integrated and tested for Version 1. Version 2 was designed to be more compact and robust with field trials in mind.

4.5.1 Power

Version 1 is powered from the PV module that it measures. This results in no need for an external power source however unnecessary power is drawn from the PV module making it less efficient, and the sensor node can only send measurement data when the PV module voltage is higher than 18 V as discussed in Section 4.4.1. The sensor thus only operates in the daytime when there is sufficient sunlight to produce the minimum required voltage.

For Version 2 it was decided to not draw any power from the PV module it monitors and to have some sort of energy storage for the sensor node to be operational throughout day and night. Version 1 has a main power supply voltage of 5 V, it was decided to lower this voltage to 3.3 V for Version 2. This is done to save power since 3.3 V devices use less power than their 5 V counterparts. Most low power devices, such as the LoRa radio module and accelerometer operate on 3.3 V.

Stellenbosch University https://scholar.sun.ac.za

The voltage regulator used to supply the 3.3 V main power supply is a LM3670 miniature step-down DC-DC converter from Texas Instruments. The LM3670 has an input voltage range of 2.5 V - 5.5 V with a fixed output voltage of 3.3 V [46]. The device is optimised for powering ultra-low circuits from a Li-ion cell or Ni-MH/NiCd batteries. The device can provide up to 350 mA load current.

Figure 4.31 illustrates the main power supply circuit design for sensor node Version 2. There is a small 500 mW solar panel connected to PVin that is used to charge the batteries that give power to the DC-DC converter. The solar module is a 55 mm by 70 mm 500 mW panel with a voltage of 5.5 V and a current of 100 mA at peak power [47]. Diode D2 is a Schottky diode that is placed between the small PV module and the battery connection. The function of D2 is to prevent reverse current flow from the battery to the PV module. A Schottky diode is used because it has a lower forward voltage drop than regular diodes.

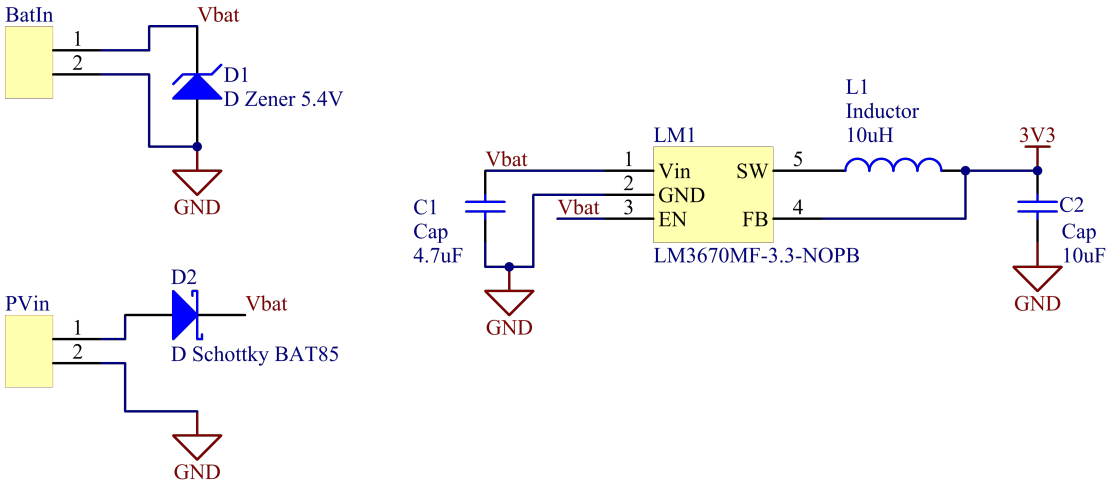

Figure 4.31: Main Power Supply Sensor Node Version 2 Circuit Design

Diode D1 is a 5.4 V Zener diode that is placed across the battery to limit the battery voltage to below the maximum voltage of 5.5 V that the DC-DC converter can handle [46]. The batteries that are used to power the sensor node circuitry are 4 NiMH 700 mAh AA rechargeable batteries. These batteries have a nominal voltage of 1.2 V resulting in a combined voltage of 4.8 V when connected in a series configuration.

Capacitor C1, C2 and Inductor L1 is recommended by the LM3670 datasheet [46]. C1 is required to make the input voltage stable, C2 and L1 are required to filter the square wave that is generated by the SMPS (Switch Mode Power Supply) into a 3.3 V DC signal. The values of C1, C2 and L1 are recommended in the device datasheet and inductor L1 should have a saturation current rating of at least 800 mA [46]. The inductor that is used for L1 is a 10 uH inductor with a maximum DC resistance of 52 mΩ and a saturation current of 2.5 A [48].

4.5.2 Microcontroller

The microcontroller used on Version 2 of the sensor node is the Atmel ATmega328/P. This is the same microcontroller that is used on the Arduino Nano as discussed in Section 4.4.2. The microcontroller has an operating voltage of 1.8 V to 5.5 V and has the same number of input and output pins as discussed in Section 4.4.2.2 [49].

Stellenbosch University https://scholar.sun.ac.za

The circuit design for the ATmega328/P microcontroller is shown in Figure 4.32. The Bootloader Header is used to burn the bootloader onto the microcontroller for the IDE (Integrated Development Environment) that is used to program the microcontroller. The Arduino IDE is used for Version 2 of the sensor node. The FTDI Header is used to load a program from the IDE onto the microcontroller. An external 8 MHz crystal oscillator is used as the main clock source for the microcontroller. The Arduino Nano used in Version 1 has 16 MHz crystal oscillator. An 8 MHz crystal was used in Version 2, because the microcontroller uses less power when operating at a lower frequency [49]. XTAL Y1 and capacitor C5 and C6 make up the external crystal oscillator circuitry.

Capacitor C3, C4, C7 and C8 are decoupling capacitors to ensure a smooth power supply voltage. An external switch S1 is added to manually reset the microcontroller as needed. The microcontroller is powered from the main 3.3 V power supply.

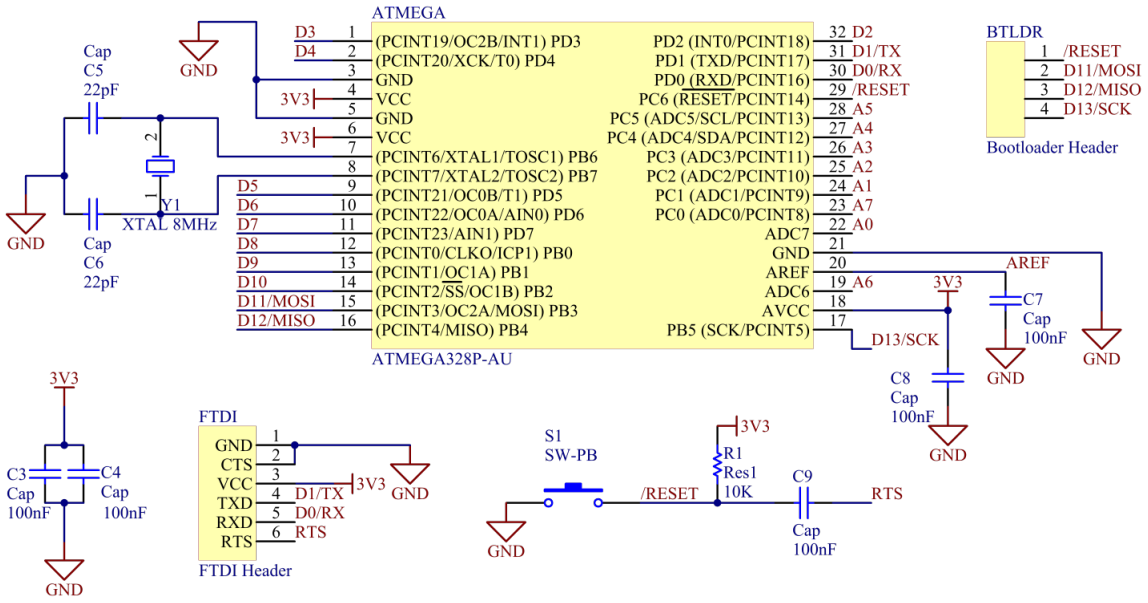

Figure 4.32: Microcontroller Sensor Node Version 2 Circuit Design

4.5.3 LoRa Radio Module

The LoRa radio module used for Version 2, is the RFM98 from Seeed Technologies. The RFM98 is similar to the DRF1278 used in Version 1; it consists of the SX1287 LoRa module, a SMD crystal and antenna matching circuitry [50]. The RFM98 was chosen because of availability issues with the DRF1278. The RFM98 module is shown in Figure 4.33. The module has a similar pin-out as the DRF1278 but the pins are not located on the same position on the module.

Figure 4.33: RFM98 LoRa Radio Transceiver 433 MHz

Stellenbosch University https://scholar.sun.ac.za

The circuit design for the RFM98 LoRa radio module is shown in Figure 4.34. The module is powered by the main 3.3 V power supply while the communication (SPI) and other digital (Reset and Interrupt) lines are connected directly to the microcontroller. An female SMA connector is used as the antenna connector. Version 1 used a U.FL connector but a SMA connector is used for Version 2 because it is more robust.

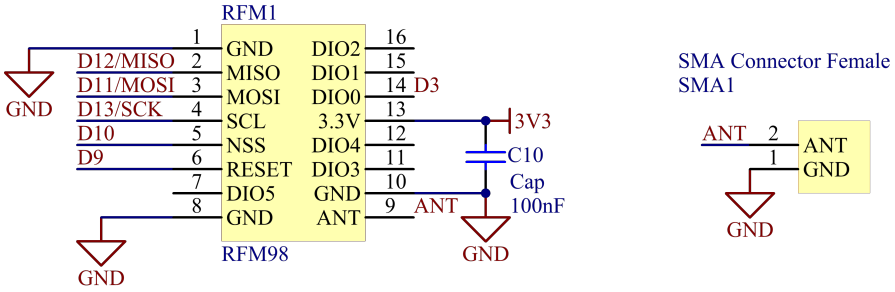

Figure 4.34: RFM98 LoRa Radio Module Circuit Design

4.5.4 Voltage Measurement

Version 2 makes use of a different voltage measurement method than Version 1. In Version 1 a linear optocoupler circuit was used to isolate the analog signal that is a scaled representation of the input voltage. This method produced noise as seen in Figure 4.26. This method also uses a substantial amount of power to produce the necessary LED drive current (1 - 20 mA) as discussed in Section 4.4.4. For Version 2 it was decided to make use of a method where a digital representation of the analog signal is isolated. Isolating a digital signal is simpler and more accurate since a digital signal only has one of two values, a high or a low.

The voltage measurement method makes use of a separate ADC IC with an isolated power supply. The ADC produces the sampled analog signal digitally in the form of I^2C communication. The digital I^2C signal is isolated with a digital isolator that works on the optocoupler principle discussed in Section 2.4.1.2. The circuit design of the voltage measurement circuitry for Version 2 of the sensor node is shown in Figure 4.35.

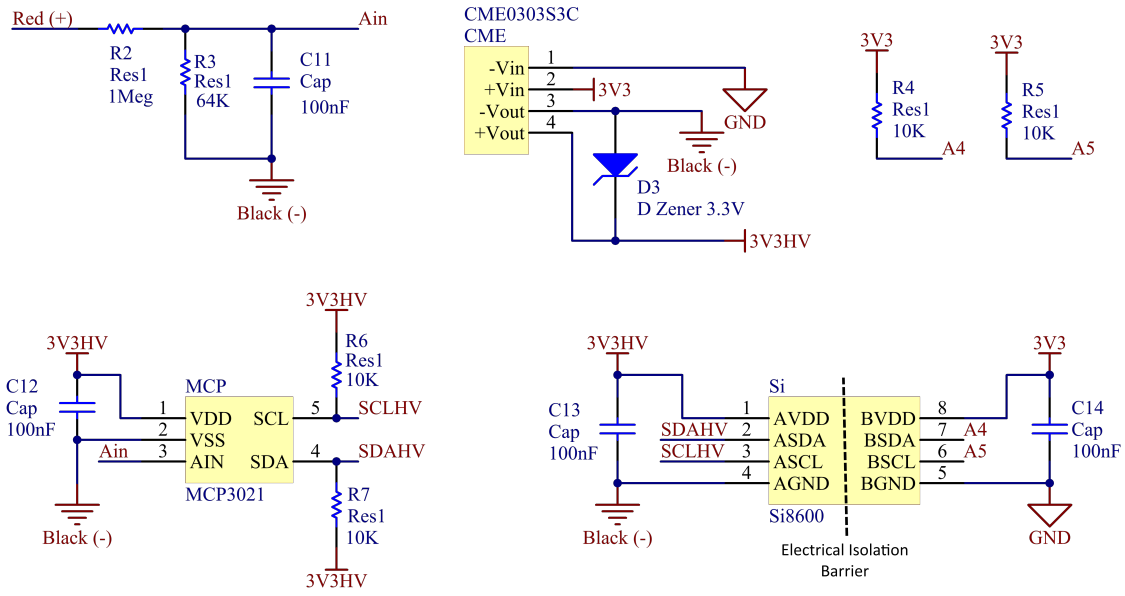

Figure 4.35: Voltage Measurement Circuitry Sensor Version 2 Circuit Design

Stellenbosch University https://scholar.sun.ac.za

The isolated power supply used to power the 'high voltage' circuitry is a CME0303S3C from Murata Power Solutions. The device is similar to the CRE1S0505SC used to provide an isolated power supply for Version 1 as discussed in Section 4.4.4, with the only difference of the input and output voltage being 3.3 V instead of 5 V [51]. Diode D3 is a 3.3 V Zener diode that is used to limit the output voltage (3V3HV) of the isolated DC-DC converter to 3.3 V. The input voltage (3V3) is supplied by the main 3.3 V power supply.

Resistor R2 and R3 represent a voltage divider circuit that is used to scale the input voltage to a voltage that fall within the ADC IC specifications. With a safety margin added the voltage divider circuit was designed to have an output voltage (Ain) of 3 V for an input voltage (Red(+)) of 50 V. Resistor R2 was chosen as 1 Mega-Ohm for low energy dissipation. The equation for resistor R3 can be written as:

$$R3 = \frac{R2 \cdot A_{in}}{Red(+) - A_{in}} = \frac{1Meg\Omega \cdot 3V}{50V - 3V} \approx 64k\Omega \tag{4.8}$$

Capacitor C11 is placed in parallel with resistor R3 to form a low-pass RC filter that filters out high frequency and noise components from the measured input voltage. The -3 dB cut-off frequency of the RC filter is:

$$f_c = \frac{1}{2\pi RC} = \frac{1}{2\pi \cdot 64k\Omega || 1Meg\Omega \cdot 100nF} = 26.5Hz \tag{4.9}$$

The ADC IC that is used to sample the scaled input voltage is a MCP3021 from Microchip Technology. The MCP3021 is a low-power single-channel 10-bit A/D (analog to digital) converter with I^2C interface. The device works from a single supply voltage of 2.7 V to 5.5 V [52]. The device is powered by the isolated DC-DC converter. Resistor R6, R7, R4 and R5 are pull-up resistors that are required for I^2C communication.

The digital isolator used to isolate the Data and Clock line of the I^2C communication between the MCP3021 ADC and the microcontroller is a Si8600 bidirectional I^2C isolator. The Si8600 has a operating voltage of 3 V to 5.5 V and has a UL 1577 safety regulatory approval that passed isolation voltage tests of up to 5000 VRMS for 1 minute [53]. The Si8600 is powered by the isolated DC-DC converter on the 'high voltage' side and by the main 3.3 V power supply on the isolated side.

Pins A4 and A5 are the Data and Clock lines that connect to the Data and Clock lines of the microcontroller as shown in Figure 4.32.

4.5.5 Current Measurement

Version 2 of the sensor node makes use of the same current measurement technique used in Version 1 as described in 4.4.5. The only difference is that a different current sensor IC is used. Version 1 used a ACS712 Hall-effect sensor. The ACS712 requires a supply voltage of 5 V and measured up to 20 A AC and DC thus ±20 A. This results in a output voltage of 2.5 V for a current of 0 A and an increase in voltage of 100 mV/A thereafter as shown in Figure 4.27.

Version 2 makes use of a ACS722 Hall-effect sensor. The ACS722 requires a 3.3 V supply voltage and is specifically designed to measure DC current. The device can measure up to 10 A and has a sensitivity of 264 mV/A [54]. The current measurement circuit design is shown in Figure 4.36. The ACS722 is powered by the main 3.3 V power supply and the measured output voltage is connected to analog input A1 of the microcontroller.

Stellenbosch University https://scholar.sun.ac.za

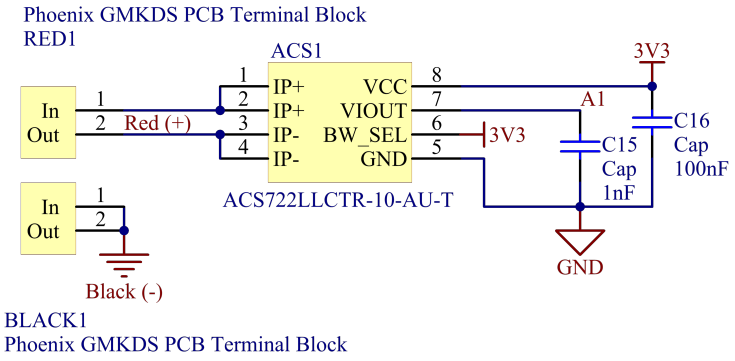

Figure 4.36: ACS722 Current Measurement Circuit Design

4.5.6 Irradiance Measurement

Version 2 conducts irradiance measurements using the same principle and circuit components than in Version 1 with minor changes. The irradiance measurement circuit design for Version 2 is shown in Figure 4.37. The operational amplifier (OPA347) is powered by the main 3.3 V power supply. The resistor that converts the photocurrent into a voltage, was changed from 10 kΩ to 8 kΩ to compensate for the maximum voltage that the microcontroller can sample being 3.3 V instead of 5 V.

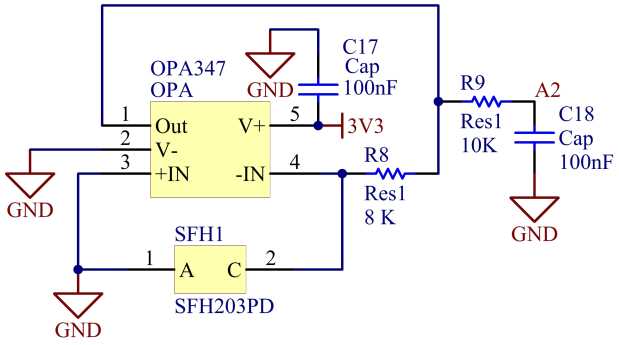

Figure 4.37: Irradiance Measurement Sensor Node Version 2 Circuit Design

Resistor R9 and Capacitor C18 was added to create a RC filter that filters out high frequency and noise components before the signal is sampled by the microcontroller. The -3 dB cut-off frequency of the RC filter is:

$$f_c = \frac{1}{2\pi RC} = \frac{1}{2\pi \cdot 10k\Omega \cdot 100nF} = 159.1Hz \tag{4.10}$$

4.5.7 Temperature Measurement

4.5.7.1 Ambient Temperature

Version 2 makes use of a different IC to take ambient temperature readings, this is done because the LM35 temperature sensor used in Version 1 requires at least a 4 V power supply. Version 2 makes use of a MCP9700AT low-power linear active thermistor IC. The MCP9700 is a analog temperature sensor that converts temperature to analog voltage. The MCP9700 has a measurement range of -40°C to 125°C, a operating voltage range of 2.3 V to 5.5 V and a sensitivity of 10 mV/°C [55]. The ambient temperature circuit design is shown

Stellenbosch University https://scholar.sun.ac.za

in Figure4.38. The MCP9700 is powered by the main 3.3 V power supply and the output voltage is connected to analog input pin A3 on the microcontroller.

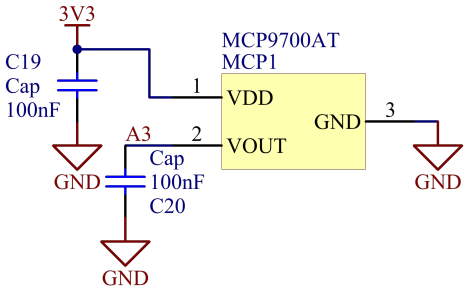

Figure 4.38: MCP9700 Ambient Temperature Measurement Circuit Design

Module Backside Temperature measurements and orientation and tampering detection are done with the same devices in Version 2 than those used in Version 1. The only difference is that the devices are powered by the main 3.3 V power supply and that there is no logic level shifting circuitry required to interface the accelerometer with the microcontroller in Version 2, since both these devices operate on 3.3 V.

4.5.8 Assembled Sensor Node PCB

The PCB for sensor node Version 2 was manufactured commercially by a PCB manufacturer. The PCB was populated in-house. The assembled PCB and where various components are located is shown in Figure 4.39.

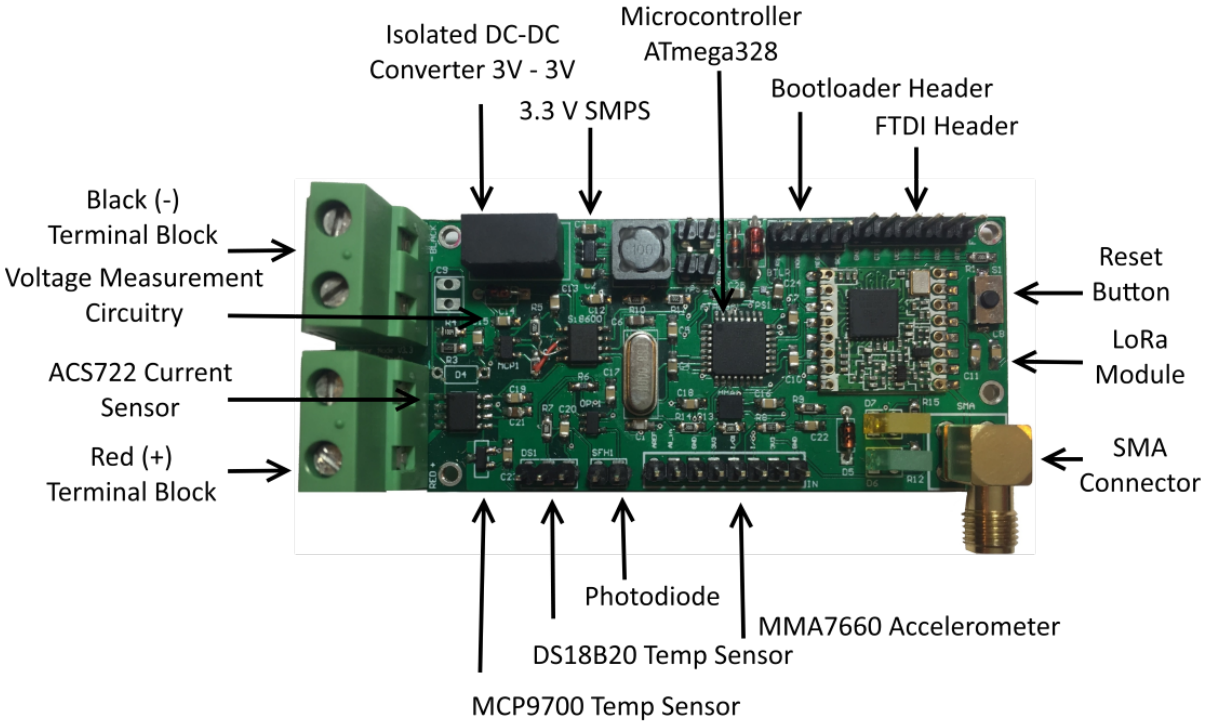

Figure 4.39: Sensor Node Version 2 Assembled PCB

An enclosure and a bracket was designed in Autodesk Inventor and manufactured with PLA (Poly-Lactic Acid) plastic using a 3D printer. The design drawing of the enclosure is

Stellenbosch University https://scholar.sun.ac.za

presented in Appendix A. The enclosure is used to house the sensor node PCB along with a battery holder that contains the 4 NiMH AA rechargeable batteries. The bracket attaches to the enclosure with two nuts and bolts and is clamped onto the edge of a PV module with another nut and bolt. The bracket is used to attach the enclosure to the backside of the PV module that is being measured. The photodiode and small PV module that charges the sensor node batteries are also attached to the bracket. The design drawing of the bracket is presented in Appendix B.

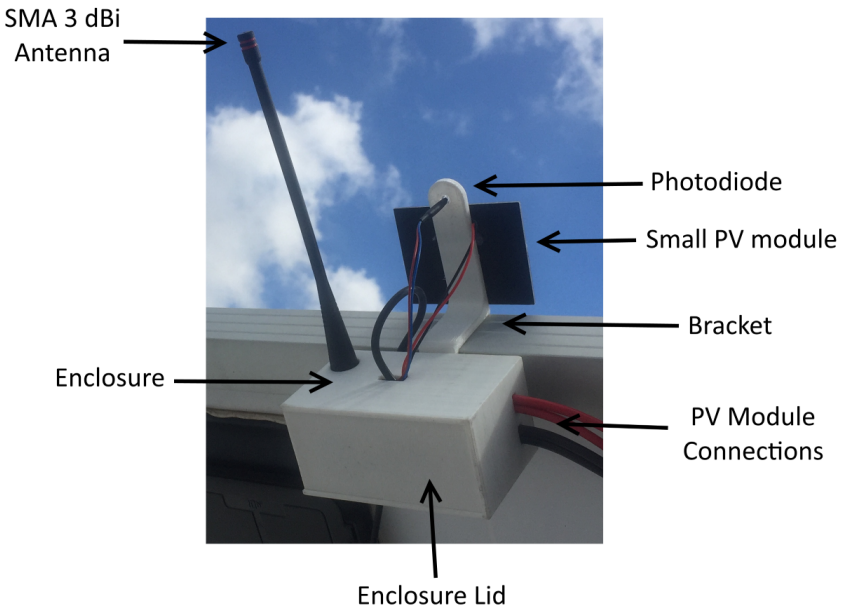

Figure 4.40: Sensor Node Version 2 Enclosure and Bracket Bottom View

The sensor node enclosure and bracket and the various external components that connect to the sensor node can be seen in Figure 4.40 and Figure 4.41. A bottom view is shown in Figure 4.40 and a top view is shown in Figure 4.41.

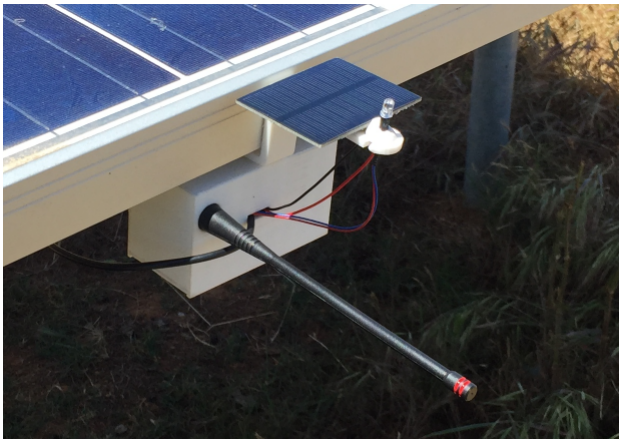

Figure 4.41: Sensor Node Version 2 Enclosure and Bracket Top View

4.5.9 Sub-System Evaluation

The sub-system evaluations were done in the form of field measurement results that are presented in Chapter 6.

Stellenbosch University https://scholar.sun.ac.za

4.5.10 Power Consumption

The power consumption of sensor node Version 2 is presented in Table 4.5. The input voltage of the sensor node when the measurements were taken was 4.8 V. This is the nominal voltage of the 4 x 1.2 V batteries that power the sensor node.

Table 4.5: Sensor Node Version 2 Power Consumption

Quantity	Idle Mode	Measurement Mode	Transmit Mode
Current	52.3 mA	59.8 mA	78.7 mA
Power	251.04 mW	287.04 mW	377.76 mW

Version 2 of the sensor node uses less than half of the power that Version 1 used as presented in Section 4.4.11. This can be attributed to the reduction in operating voltage of the circuitry from 5 V to 3.3 V. However, the idle power usage is a concern since the only function of the sensor node in this mode is to wait for the interval period to pass. When measurement are taken and sent at a one minute interval on a Spreading Factor of 11 the sensor node is in idle mode 98.7 % of the time.

4.6 Sensor Node Version 3

Version 3 of the sensor node serves as an improvement of various sub-systems and external features resulting from issues that were found in field tests of Version 2. Version 3 was designed with field trials and commercial production of higher quantities in mind.

4.6.1 Power

In Version 2 the small PV module that charges the batteries was connected directly to the battery voltage. Not regulating the current and voltage that are applied to rechargeable batteries can damage the batteries over time. Version 3 has an additional charge controller IC that regulates how the battery is charged by the small PV module. The small PV module input and battery charging circuit design is shown in Figure 4.42.

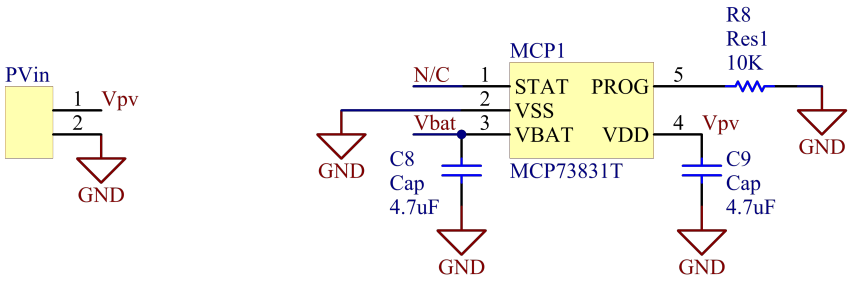

Figure 4.42: Battery Charging Circuit Design

The charge controller IC used is the MCP73831 miniature single-cell, fully integrated Li-ion charge management controller from Microchip Technology. The MCP73831 has reverse discharge protection, programmable charge current of 15 mA to 500 mA and an output voltage of 4.2 V [56]. Resistor R8 (10 kΩ) is used to select the maximum charge current at 100 mA according to the device datasheet [56]. Capacitor C8 and C9 are used to make the input and output voltage stable.

Stellenbosch University https://scholar.sun.ac.za

Version 3 is powered by a single-cell 3.7 V 18650 Li-ion battery. A 18650 PCB mount battery holder is located on the sensor node PCB that houses the battery. A 500 mA surface mount fuse is added for over-current protection since 18650 batteries can deliver a high current in the event of a short-circuit failure. The same LM3670 SMPS used in Version 2 is used in Version 3. The battery and power supply circuit design is shown in Figure 4.43.

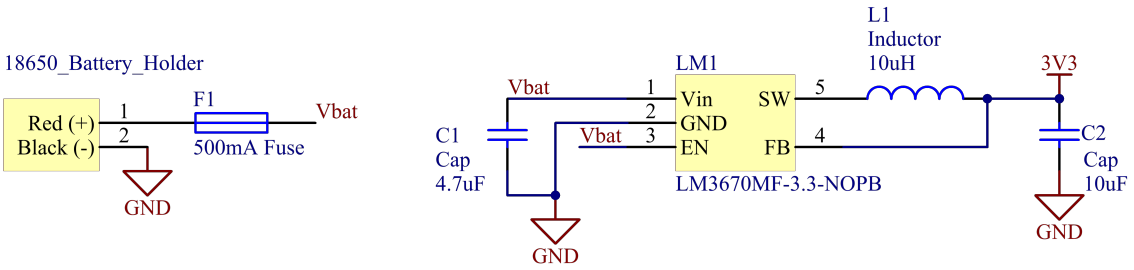

Figure 4.43: Power Supply Version 3 Circuit Design

A power switch was added to reduce the power consumption of circuit elements in the interval between measurements. The power switch is used to disconnect the main 3.3 V power supply from all of the circuit components except for the microcontroller, LoRa module and accelerometer when the sensor node is not actively taking any measurements. The power switch circuit design is shown in Figure 4.44.

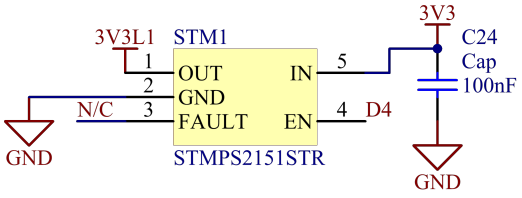

Figure 4.44: Power Switch Circuit Design

The power switch used is a STMPS2151STR enhanced single channel power switch from STMicroelectronics. The STMPS2151STR can switch a constant current of 500 mA and has an operating voltage of 2.7 V to 5.5 V [57]. The power switch is controlled by a logic enable input, digital pin D4 on the microcontroller.

The microcontroller, LoRa module, voltage-, current-, irradiance- and temperature measurement techniques and devices are similar to those used in Version 2.

4.6.2 Orientation Measurement and Tampering Detection

Field tests on sensor node Version 2 found that the accelerometer used on Version 1 and Version 2 is too sensitive and triggers the tampering detection interrupt pin for low impacts. This is due to the fact that the accelerometer used (MMA7660) can only detect up to ±2g. The aim of the accelerometer is to pick up mechanical striking events such as attempted theft. A mechanical strike of this kind generates forces between 3g and 6g. For Version 3 an accelerometer with a higher measurement range is used. The accelerometer circuit design for Version 3 is shown in Figure 4.45.

Stellenbosch University https://scholar.sun.ac.za

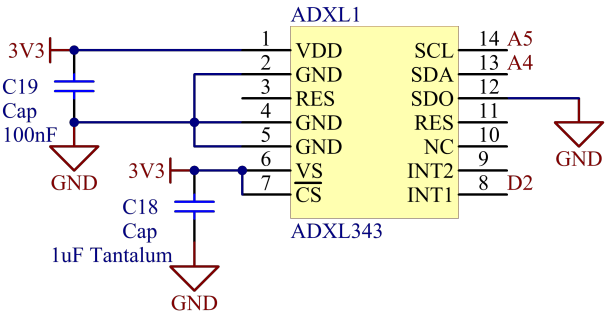

Figure 4.45: ADXL343 Accelerometer Circuit Design

The accelerometer used is the ADXL343 digital MEMS accelerometer supplied by Analog Devices. The ADXL343 has a measurement range of ±2g up to ±16g and a operating voltage of 2 V to 3.6 V [58]. The device is powered by the main 3.3 V power supply and communicates with the microcontroller via I^2C communication using analog pins A4 and A5. There is also an interrupt pin that is connected to digital pin D2 of the microcontroller. This pin is used to send an interrupt signal to the microcontroller when a mechanical strike greater than a user defined threshold is detected.

4.6.3 Assembled Sensor Node PCB

The PCB for Sensor Node Version 3 was manufactured commercially by a PCB manufacturer. The PCB was populated in-house. Figure 4.46 shows the assembled PCB and where various components are located. The complete schematic design for sensor node Version 3 is presented in Appendix C.

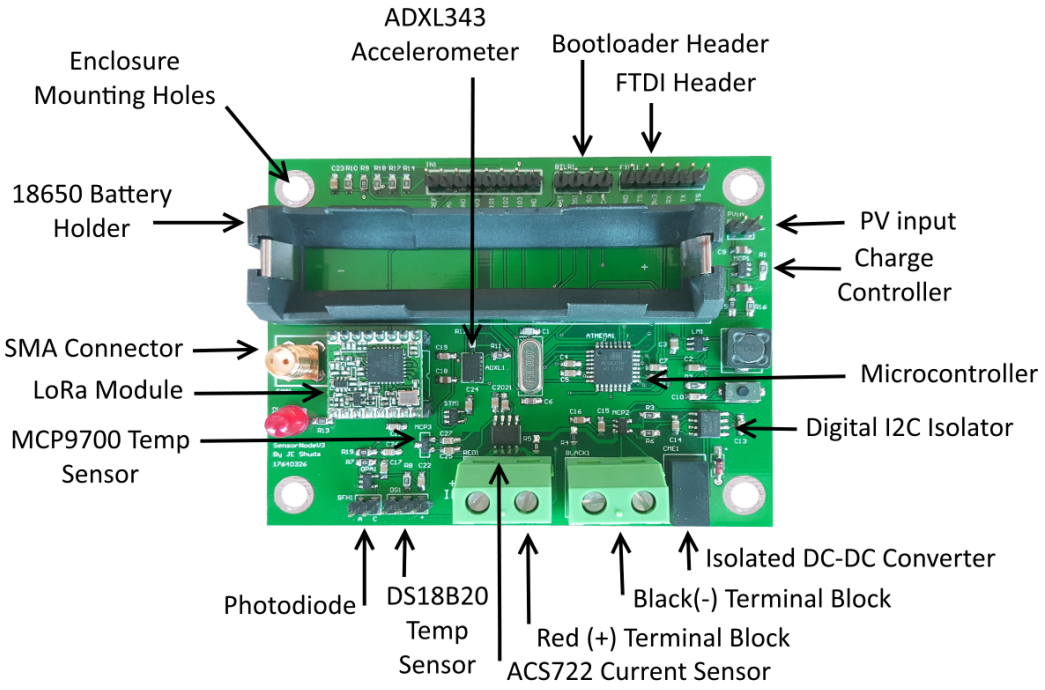

Figure 4.46: Sensor Node Version 3 Assembled PCB

The enclosure used for Version 2 was constructed by means of a 3D printer with PLA material. PLA is not waterproof or UV resistant. The enclosure for Version 2 was made as a

Stellenbosch University https://scholar.sun.ac.za

proof of concept to test the sensor node with its various attachments in the field. For Version 3 an IP66 Polycarbonate enclosure is used. The enclosure used is a Enlec ENL120806P from Allbro. The enclosure has an operating temperature of -20°C to 110°C and an expected UV life of 5 to 8 years for direct exposure. The PCB was designed to have mounting holes that align with dedicated mounting pedestals within the enclosure.

For Version 2 one bracket was used to secure the enclosure to the PV module, this was found to be unstable. For Version 3 two brackets was designed that screw onto the enclosure with two nuts and bolts each. The brackets were constructed by means of a 3D printer using PLA material. Each bracket has one large nut and bolt that attach the enclosure to the PV module. One bracket is also houses the small PV module that charges the sensor node battery as well as the photodiode that is used for irradiance measurements. The design drawing of both brackets is presented in Appendix B.

A bottom view of the sensor node circuitry within the enclosure attached to a PV module is shown in Figure 4.47. The enclosure lid was removed to show the sensor node circuitry. The antenna used for the test set-up shown is a simple wire-wound helical antenna. There are two glands inserted into the enclosure where the various external cables and components enter the enclosure. These are PG13.5 IP68 rated glands from ACDC Dynamics.

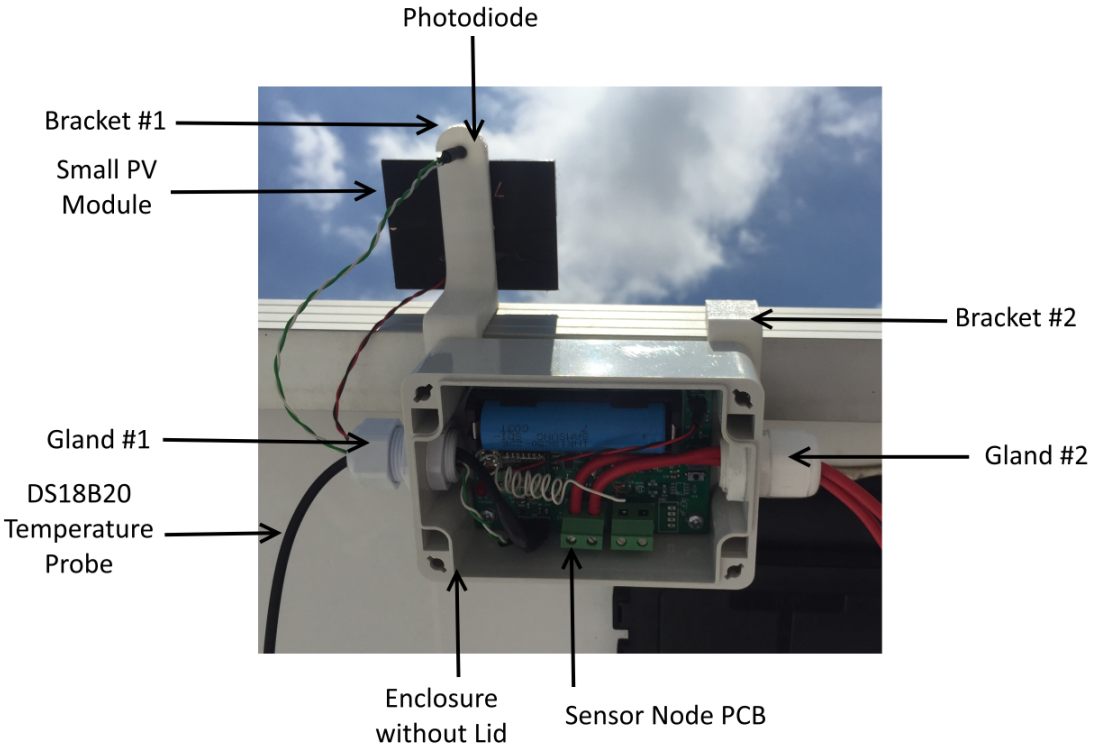

Figure 4.47: Sensor Node Version 3 Enclosure and Bracket Bottom View

4.6.4 Sub-System Evaluation

The sub-system evaluations were done in the form of field measurement results that are presented in Chapter 6.

4.6.5 Power Consumption

The power consumption of sensor node Version 3 is presented in Table 4.6. The input voltage of the sensor node when the measurements were taken was 4.2 V. This is the nominal voltage

Stellenbosch University https://scholar.sun.ac.za

of 18650 battery that powers the sensor node.

Table 4.6: Sensor Node Version 3 Power Consumption

Quantity	Idle Mode	Measurement Mode	Transmit Mode
Current	5.7 mA	60.4 mA	79.1 mA
Power	23.9 mW	253.68 mW	332.2 mW

The measurement and transmit mode power usage for Version 3 is in the same order than for Version 2. The idle mode power consumption however is more than ten times less. This can be attributed to the power switch that was implemented in Version 3. The power switch removes power from all of the analog and digital sensor circuitry for the duration between measurements. The microcontroller and LoRa transceiver are also placed in sleep mode during this time. These interventions greatly reduce the overall power consumption of the sensor node.

4.7 Gateway

The purpose of the gateway is to collect measurement data from the various sensor nodes, add a date and time stamp to each measurement, and store the measurement data on a server that can be accessed remotely and immediately. For the gateway a Raspberry Pi 3 Model B was used. The Raspberry Pi 3 Model B is a ARM based SBC (Single Board Computer) that runs the Debian based GNU/Linux operating system, Rasbian. The Pi 3 Model B has an Ethernet and Wi-Fi connection for Internet access and has 40-pin extended GPIO (General Purpose Input Output). The GPIOs operate on 3.3 V, incorporating a dedicated hardware SPI interface with two chip enable pins.

The same LoRa module that is used on Version 2 and Version 3 of the sensor node is used for the gateway. A shield was designed that attaches to the GPIO pins of the Pi 3 Model B. The circuit design for the shield is shown in Figure 4.48. The LoRa module is powered by a 3.3 V rail supplied by the Pi 3 Model B. A female SMA connector is used to connect an antenna to the LoRa module.

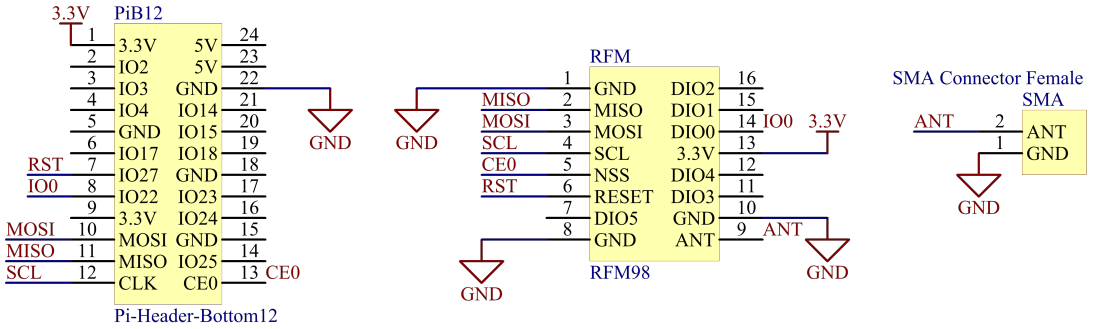

Figure 4.48: Gateway to RFM89 Shield Circuit Design

A top view of the Raspberry Pi 3 Model B and the RFM98 shield is shown in Figure 4.49. The Pi 3 Model B is powered by a 2 A 5.1 V micro USB supply and is connected to the internet via the Ethernet port that is connected to an Internet modem with a network cable.

Stellenbosch University https://scholar.sun.ac.za

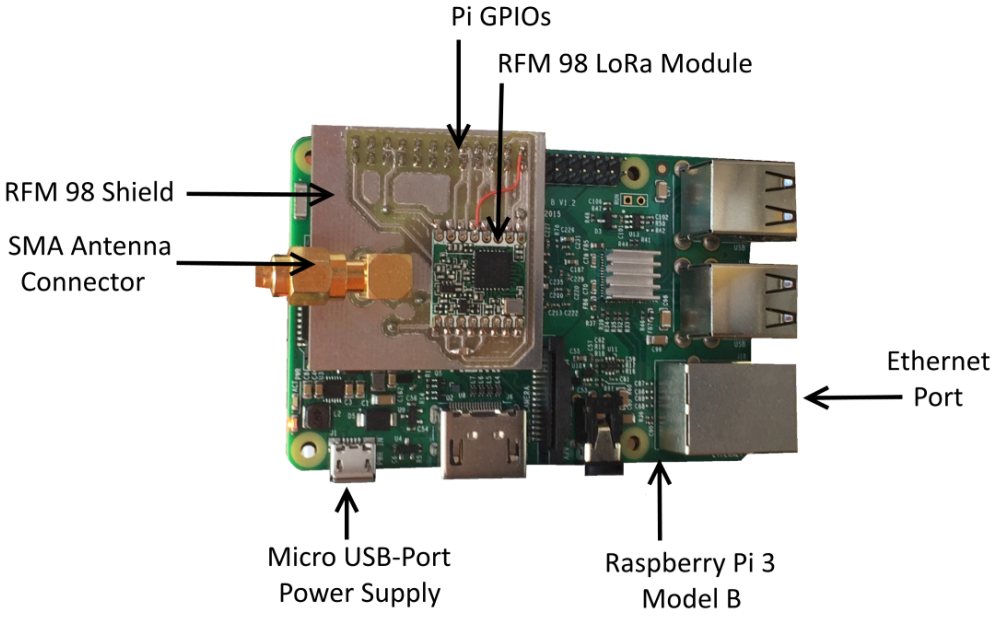

Figure 4.49: Raspberry Pi 3 Model B and RFM98 Shield Top View

Stellenbosch University https://scholar.sun.ac.za

Chapter 5

Software Design of Monitoring System

5.1 Chapter overview

In this chapter the software design of the monitoring system is presented. Software flow diagrams are used to show how the various sub-components of the monitoring system function and interact with one another.

5.2 Sensor Node Measurement Procedure

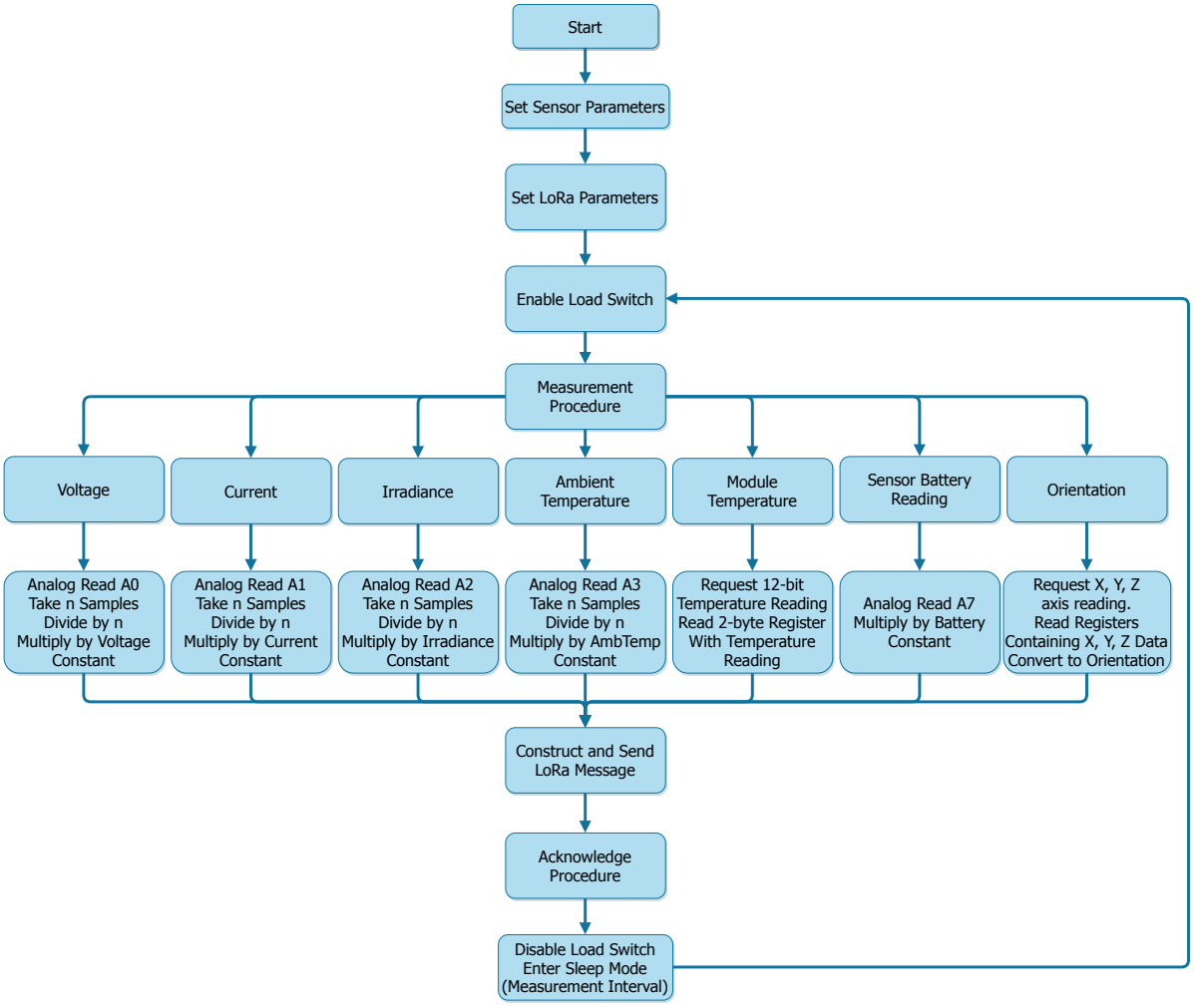

Figure 5.1: Software Flow Diagram of Sensor Node Operation

Stellenbosch University https://scholar.sun.ac.za

A software flow diagram of the sensor node operation is shown in Figure 5.1. The software presented is used in the final monitoring system that utilises sensor node Version 3.

5.2.1 Sensor Parameters

The following sensor parameters are set for each sensor node:

- Gateway ID
- Sensor ID
- Number of Samples
- Measurement Interval
- Measurement Constants

The Gateway ID is a hexadecimal value containing the ID of the gateway that the specific sensor node reports to (Default value 0xFF). The Sensor ID is a hexadecimal value containing the ID of the specific sensor node. The ID starts at 0x01 for sensor node number 1 and is incremented accordingly thereafter.

The Number of Samples parameter is used to implement multiple sample software filtering on analog inputs. The number of samples is taken by the ADC, added together, and divided by the number to obtain an average. This is done to smooth out noise and conversion errors produced by the measurement circuitry and the ADC. The default number of samples is set to 300.

The measurement interval indicates the amount of time (in milliseconds) that each sensor node is placed into sleep mode before the next set of measurements are taken. The measurement interval is dependant on the amount of measurement detail that is required for the specific application. The default measurement interval is set to 1 minute. This results in a set of measurements from each sensor node at an interval of one minute.

The measurement constants are calibration constants that are used to convert each analog measurement result, ranging from 0 - 1023 (10-bit ADC) to the respective true values. Each individual sensor is calibrated due to tolerance differences in resistor values and measurement ICs. The calibration constants are obtained by dividing the true value of a measurement by the ADC result.

5.2.2 LoRa Parameters

The following LoRa parameters are set for each sensor node:

- Frequency
- Transmit Power
- Spreading Factor
- Signal Bandwidth
- Coding Rate
- Preamble Length

Stellenbosch University https://scholar.sun.ac.za

- Sync Word

Frequency refers to the centre frequency or carrier frequency of the LoRa signal. The LoRa radio module used on the sensor nodes and gateway (RFM98) has a frequency range of 433 MHz to 470 MHz. The frequency range for ISM devices in South Africa in the 433 MHz range are 433.04 MHz to 434.79 MHz [59]. The default frequency is set to 434 MHz which falls within the ISM frequency range.

Transmit Power of the RFM98 ranges from -1 dBm to +17 dBm in normal mode. The power can be set to +20 dBm in high power mode but this mode is not recommended for long term operation [50]. The default transmit power is set to +17 dBm.

Spreading Factor refers to the rate at which chirps are transmitted, a symbol is encoded into each chirp. The different spreading factors and data rates were discussed in Section 2.5.6.2. The default spreading factor is set to 10.

Signal Bandwidth can range from 7.8 kHz to 500 kHz. An increase in bandwidth results in a higher effective data rate, thus reducing transmission time at the expense of reduced sensitivity. The default bandwidth is chosen as 125 kHz.

Coding Rate refers to an overhead ratio on each LoRa packet that occurs due to cyclic error coding that is implemented to improve the robustness of the communication link. The overhead ratio ranges from 1.25 to 2. The default coding rate is set to 1 that results in an overhead ratio of 1.25.

Preamble Length refers to the amount of symbols (chirps) that is sent before the actual data packet to synchronize the LoRa receiver with the incoming data packet. The default preamble length is set to 8 symbols.

Sync Word is a hexadecimal value that is used to verify if a message from a certain node is meant for another node. The LoRa radio module only decodes a message containing the same sync word as set up on the receiver. The default sync word is set to 0x12.

5.2.3 LoRa Message Structure

After the various measurements have been taken sequentially a LoRa message containing the measurement data and various other data is constructed and sent to the gateway. The structure of each LoRa message is shown in Figure 5.2.

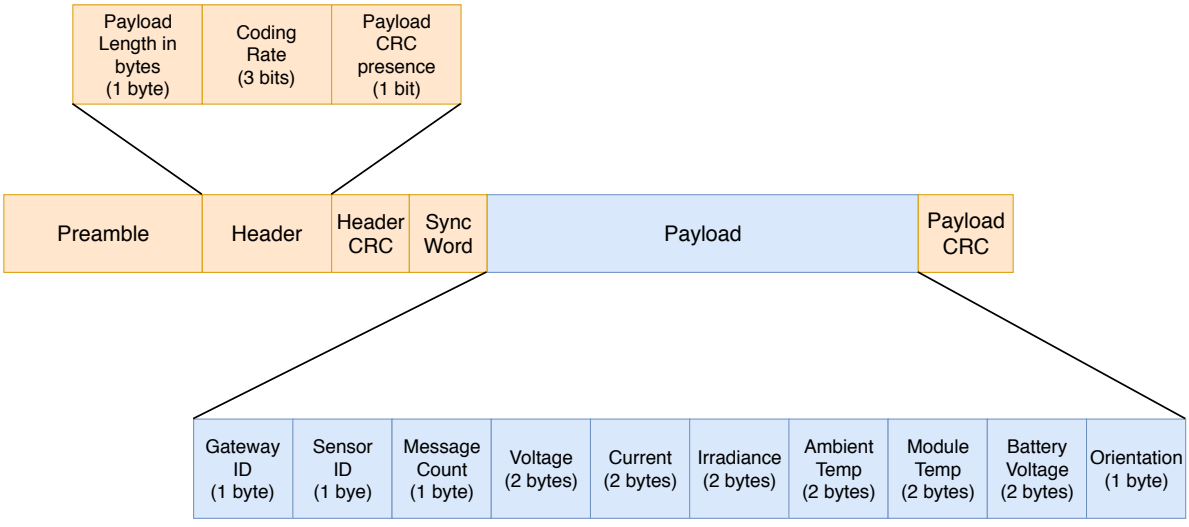

Figure 5.2: LoRa Measurement Message Structure

Stellenbosch University https://scholar.sun.ac.za

The Preamble, Header, Header CRC, Sync Word and Payload CRC are incorporated into each LoRa message, the payload is user-defined and can contain 0 - 255 bytes. The payload consists of the Gateway ID, Sensor ID and the various measurement data.

CRC (Cyclic Redundancy Check) is an error-detecting technique that is used to detect errors in the received data. There are a number of check bits (checksum) that are appended to the message. When the message is received the receiver inspects the check bits for any errors, if an error occurred the message is discarded.

5.2.4 Acknowledge Procedure

After each measurement message is sent there is an acknowledge procedure that takes place to ensure that sensor nodes are not sending measurement data simultaneously in monitoring systems where more than one sensor node is present. The software flow diagram of the acknowledge procedure is shown in Figure 5.3.

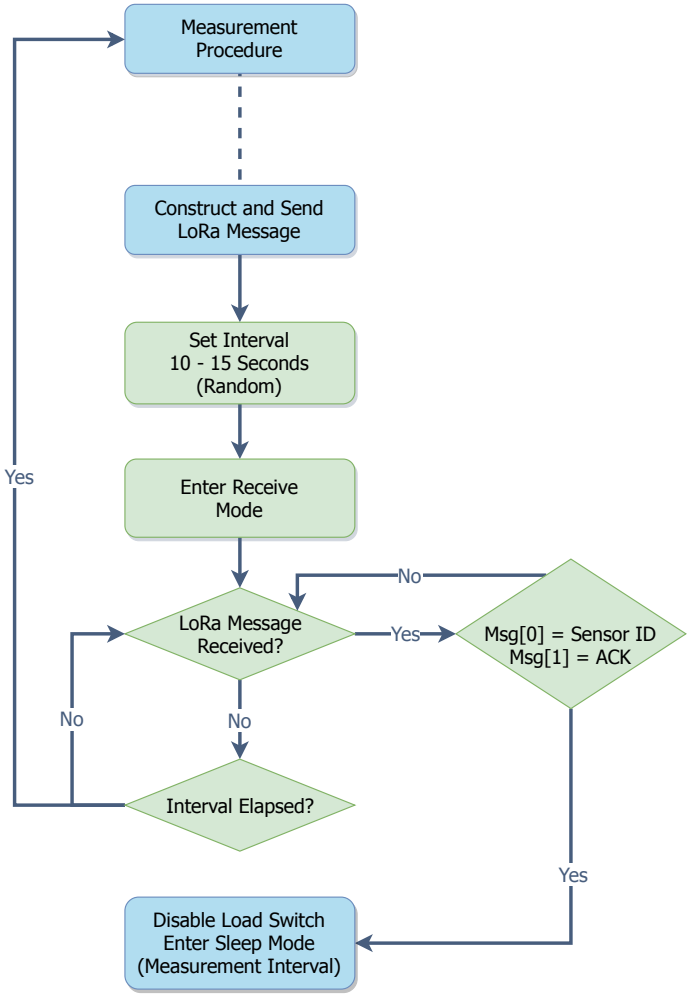

Figure 5.3: Software Flow Diagram of Acknowledge Procedure

After a measurement message is sent a random interval time of between 10 - 15 seconds is established. The LoRa module is then placed into continuous receive mode. In this mode the module listens for any incoming messages. After a LoRa message is received that contains the Sensor ID and an acknowledge code, the sensor disables the load switch and enters sleep mode for the duration of the measurement interval as defined in the sensor parameters.

Stellenbosch University https://scholar.sun.ac.za

If no message containing the Sensor ID and acknowledge code is received and the random interval time has elapsed, the sensor node takes another set of measurements and the process is repeated. In this case either the gateway did not successfully receive the message from the sensor node or the acknowledge message was not successfully received by the sensor node. A new set of measurements are taken to avoid a time difference in the gateway time-stamp and the time of the actual measurements. If the sensor node resends the message after the interval has elapsed the time-stamp and actual time of measurement would be out by the length of the interval.

A random time period of 10 - 15 seconds is used as the interval to ensure that when two or more sensor nodes send measurement data at the same time, there will be a random time difference in the resend message of each of the sensor nodes.

5.3 Gateway Data Handling Procedure

A software flow diagram of the gateway data handling procedure is shown in Figure 5.5. The default Gateway ID is 0xFF. The LoRa parameters are set the same as the parameters set for the sensor nodes as discussed in Section 5.2.2. This is required to ensure that the LoRa modules can successfully send and receive messages to and from one another.

The database used is a MySQL database that is stored on the Google Cloud Platform. The connection to the database entails entering the correct IP, an authorized user-name, password and the database name for the MySQL instance.

There is a table for each Sensor Node ID within the database. Each table contains a column for each different measurement quantity. The table name and column header with data types and sizes for Sensor Node ID 1 is shown in Figure 5.4.

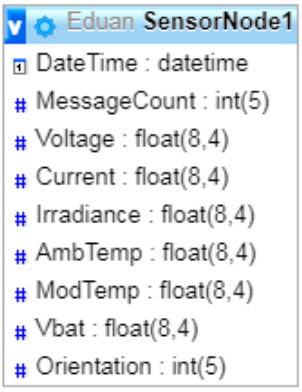

Figure 5.4: MySQL Table Name and Column Headers for Sensor Node ID 1

After a LoRa message is received containing the Gateway ID in byte position 1 the rest of the message is decoded and stored into corresponding variables. A time and date stamp is added and the variables are stored in the table corresponding to the Sensor ID.

After the data is stored into the corresponding table, the gateway sends an acknowledge message containing the Sensor Node ID and the acknowledge code. The radio is then placed into receive mode and the process is repeated.

Stellenbosch University https://scholar.sun.ac.za

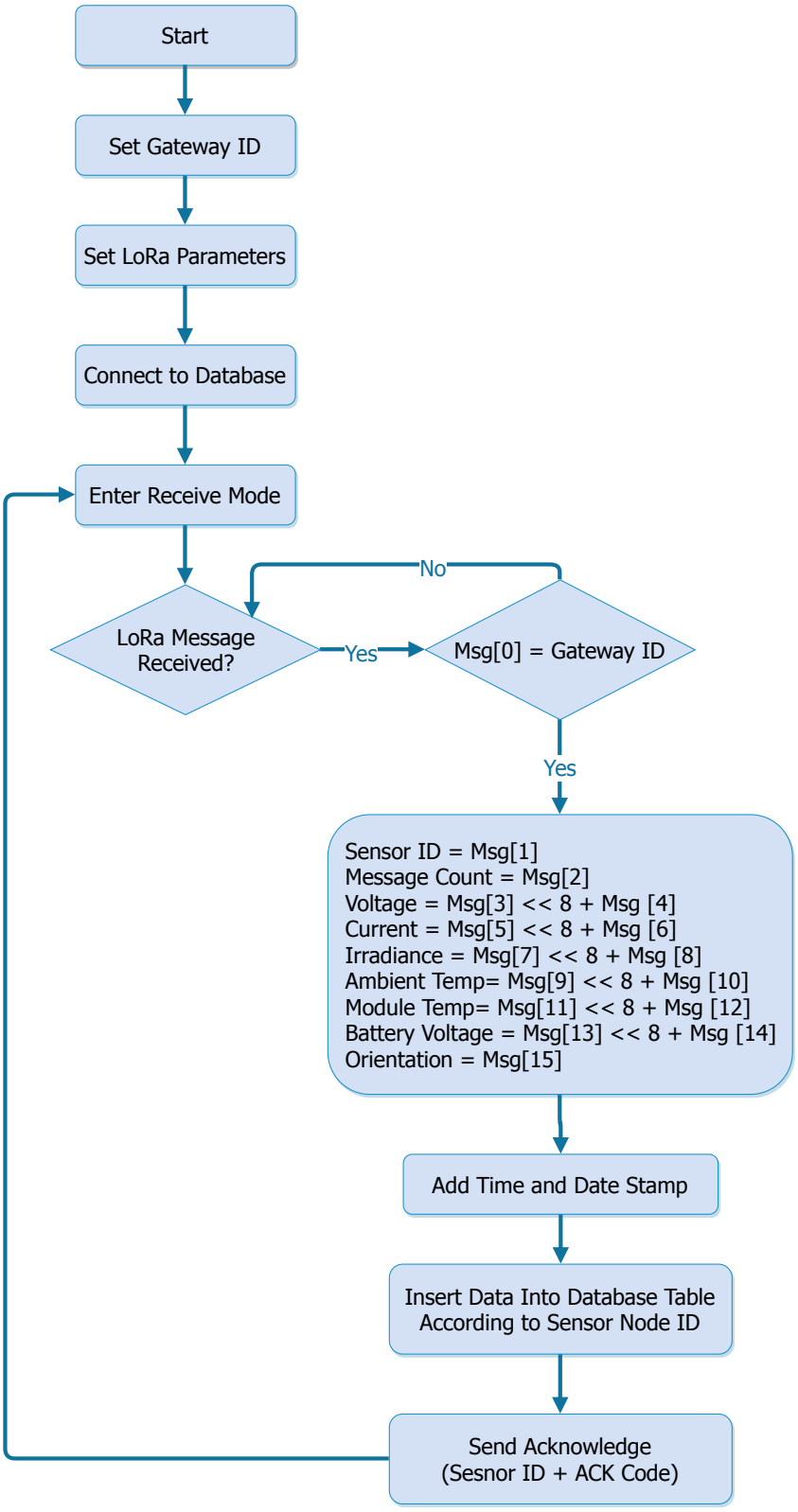

Figure 5.5: Software Flow Diagram of Gateway Data Handling Procedure

5.4 Data Analysis GUI Application

The data analysis GUI application is written in the Python Programming language using Matplotlib and Tkinter among other frameworks and tools. The interface has two main components, a Layout View and a Graph View.

Stellenbosch University https://scholar.sun.ac.za

5.4.1 Layout View

The layout view displays a layout of the solar PV plant and where various sensor nodes are located. The layout view displays critical information that is measured by each of the sensor nodes. This information includes ambient temperature, module temperature, irradiance, string current, module voltage and power, efficiency and health status. The purpose of the layout view is to display the current condition of the PV plant. The layout view is updated every 10 seconds and displays only the latest measurements. The software flow diagram of the layout view is shown in Figure 5.6.

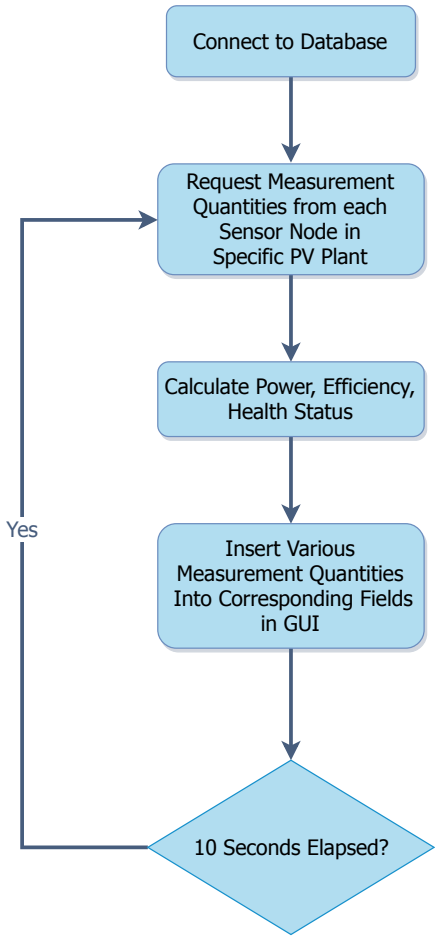

Figure 5.6: Software Flow Diagram of Layout View

5.4.2 Graph View

The graph view displays historical measurement data in the form of a graph, the user has the ability to view any measurement quantity for any of the sensor nodes. The time-frame can also be selected by the user. The purpose of the graph view is to enable the user to view and analyse historical measurement data. The software flow diagram of the graph view is shown in Figure 5.7.

Stellenbosch University https://scholar.sun.ac.za

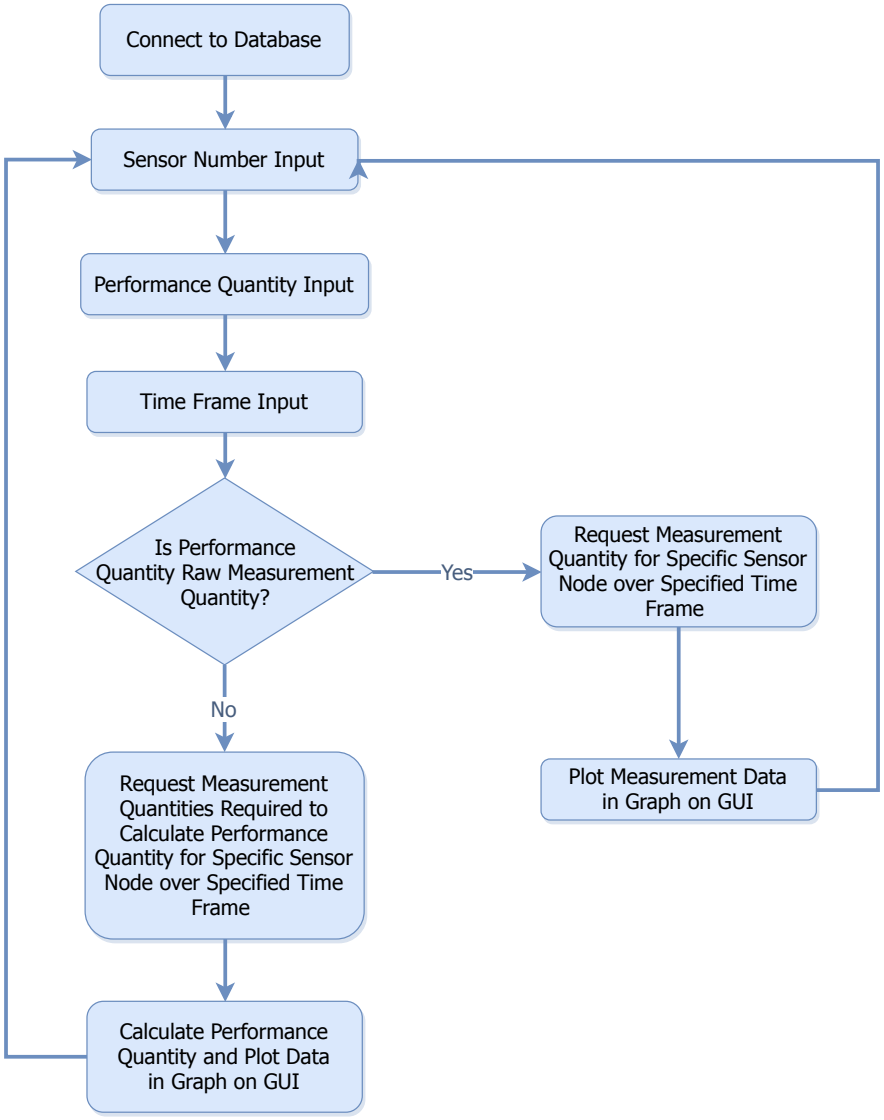

Figure 5.7: Software Flow Diagram of Graph View

Stellenbosch University https://scholar.sun.ac.za

Chapter 6

Results

6.1 Chapter overview

In this chapter measurement results are presented for various sensors nodes in a variety of set-ups. Initial field tests which were conducted to evaluate the various subcomponents of sensor node Version 2 and Version 3 are presented. This includes short-circuit and fixed resistor measurement set-ups. Wireless communication performance results which was used to evaluate the performance of LoRa in terms of range for different spreading factors are also presented. Finally, field measurements of the monitoring system as a whole is presented where a number of sensors was placed on a fully operational PV plant.

6.2 Sensor Node Version 2

6.2.1 Short-Circuit Field Measurements

A short-circuit configuration was chosen for the initial field tests because it is safe; since no high voltages are present when measuring short-circuit current. There is also a direct correlation between irradiance and short-circuit current which allows for the evaluation of the current and irradiance measurement sub-systems [5].

Sensor node Version 2 was connected to a SD ECO PLUS 240 Wp Mono-crystalline PV module. The PV module has a rated short-circuit current of 8.55 A and a current at maximum power of 8 A at STC. The test set-up is located on the 3rd floor rooftop of the Electrical and Electronic Engineering department at Stellenbosch University. The test set-up is shown in Figure 6.1.

For the test set-up a gateway was placed in another building in the Electrical and Electronic Engineering department. The distance between the sensor node and gateway is approximately 50 metres. The purpose of this test was to evaluate the performance of the measurement sub-systems of the sensor node and not the range-capabilities of the wireless communication. The sensor node was programmed to send a set of measurements at one minute intervals. The gateway stored each measurement in a mySQL database.

Stellenbosch University https://scholar.sun.ac.za

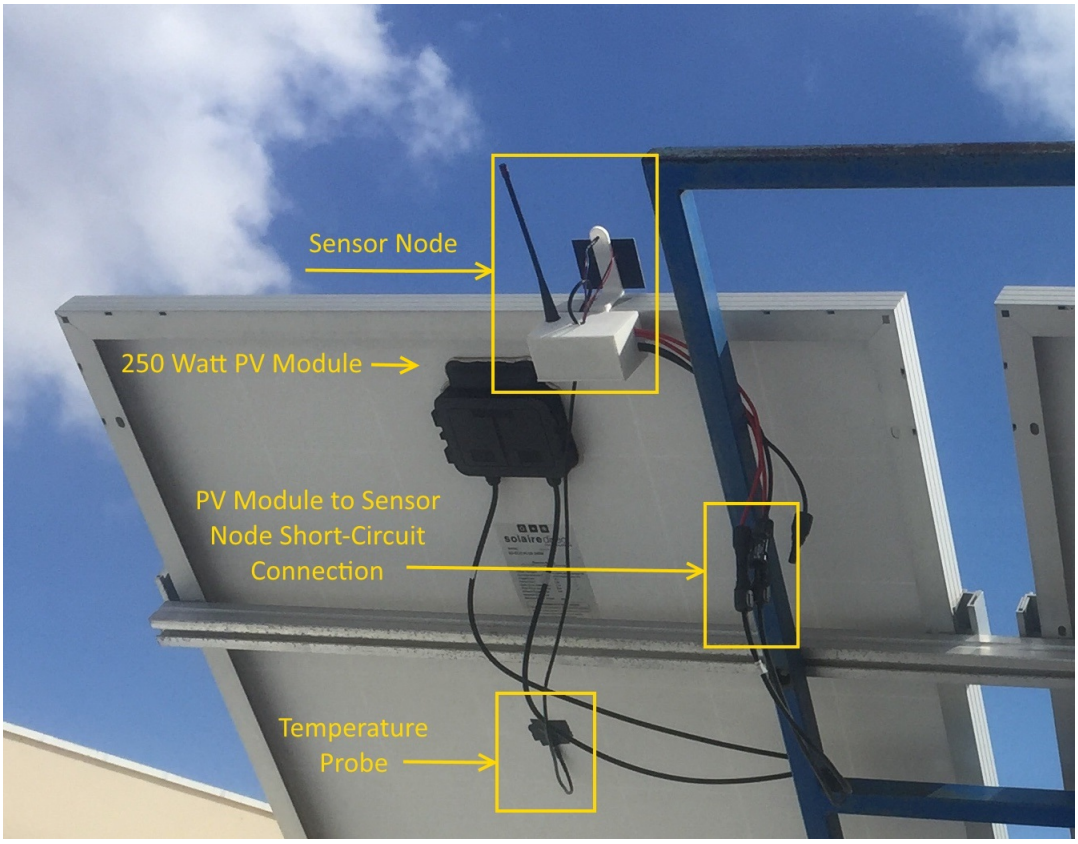

Figure 6.1: Field Test Set-up for Sensor Node Version 2 Short-Circuit Configuration

The measurement data was extracted from the mySQL database in the form of a CSV (Comma Separated Values) file and graphs were created to analyse the data. The short-circuit current measurements that were measured between the 20th and 21st of January 2018 are shown in Figure 6.2.

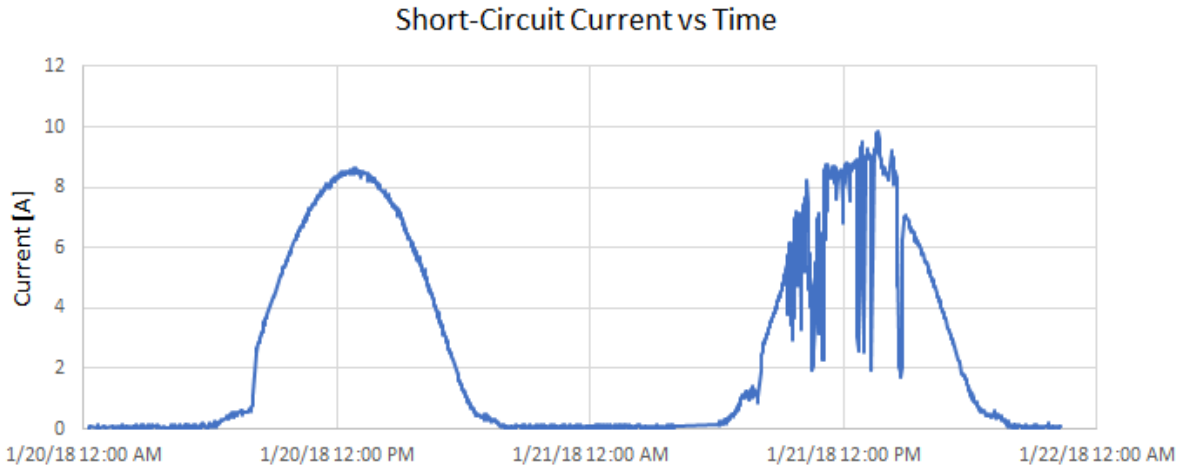

Figure 6.2: Sensor Node Version 2 Field Test Short-Circuit Current

The current sensor used in Version 2 and Version 3 of the sensor node measures at a resolution of 0.02 A with a total output error of $\pm 1.5\%$ as stated in the device datasheet [40]. The resolution of the current sensor is a 150% increase over the sensor used in Version 1. This can be attributed to the higher sensitivity of the sensor used in Versions 2 and 3.

Stellenbosch University https://scholar.sun.ac.za

The irradiance measurements that were taken over the same period is shown in Figure 6.3 There is a clear correlation between the short-circuit current and the irradiance as seen in Figure 6.2 and Figure 6.3. There is a sharp increase in irradiance at the beginning of the each day, this is due to a shadow caused by an adjacent building in the early hours just after sunrise. From the two figures it can be seen that the 20th of January was a sunny day with clear skies while the 21st of January was overcast.

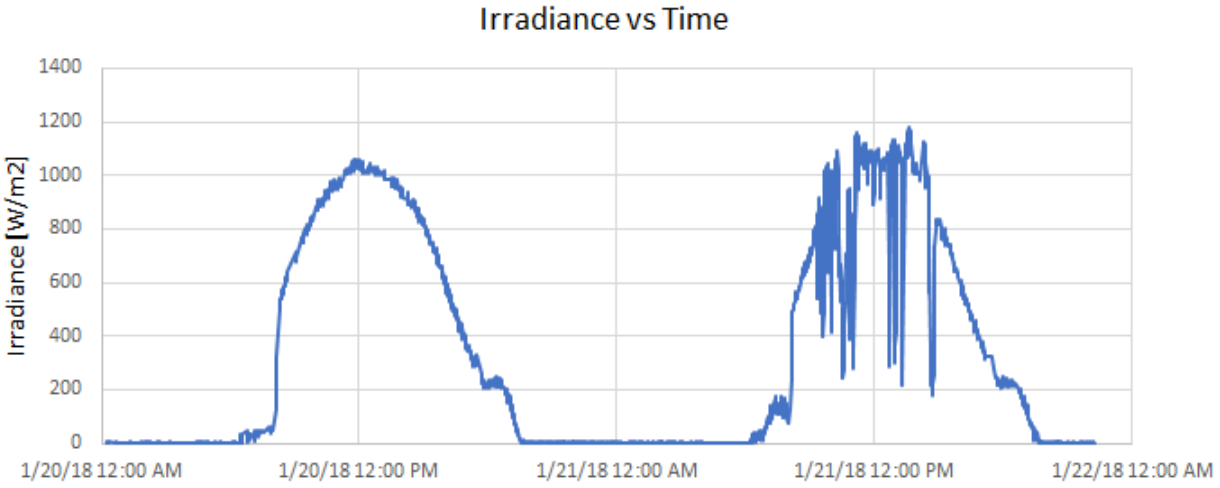

Figure 6.3: Sensor Node Version 2 Field Test Irradiance

A reference sensor is used to evaluate the irradiance measurements for sensor node Version 2. The reference sensor used is a CMP11 pyranometer from Kipp and Zonen which provides GHI measurements. The GHI measurements that were taken by the reference sensor at 1 minute intervals over the same period from the 20th to 21st January 2018 is shown in Figure 6.4.

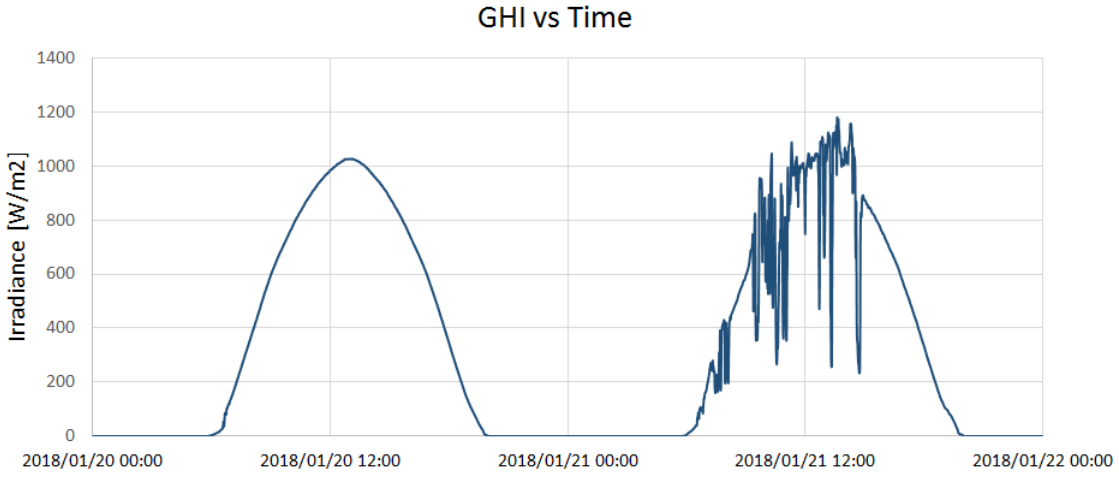

Figure 6.4: Field Test Reference Irradiance Sensor GHI Measurements

The shape of the graphs from Figure 6.4 and Figure 6.3 differ slightly, due to the fact that the pyranometer collector surface is horizontal while the photodiode located on the bracket that is attached to the PV module is not. The photodiode collector surface is placed at the same angle as the PV module surface thus measuring the irradiance that the PV module

Stellenbosch University https://scholar.sun.ac.za

is directly exposed to. This is referred to as POA (Plane of Array) irradiance. The overall shape, maximum and minimum values and intermittent dips due to clouds passing indicate accurate and reliable irradiance data captured by the sensor node.

The ambient and module backside temperature measurements are shown in Figure 6.5. The DS18B20 temperature probe used to measure the module backside temperature was attached to the PV module backside with scrim-backed polyethylene coated duct tape. The module temperature clearly differs from the ambient temperature, reaching almost 60°C on the 21st of January when the ambient temperature was just below 30°C.

The ambient temperature sensor is located on the sensor node PCB within the waterproof enclosure. This results in the ambient temperature that is being measured to be higher than the actual ambient temperature. The sensor node generates some of its own heat which stays within the enclosure; which explains the sections on Figure 6.5 where the module temperature is lower than the ambient temperature.

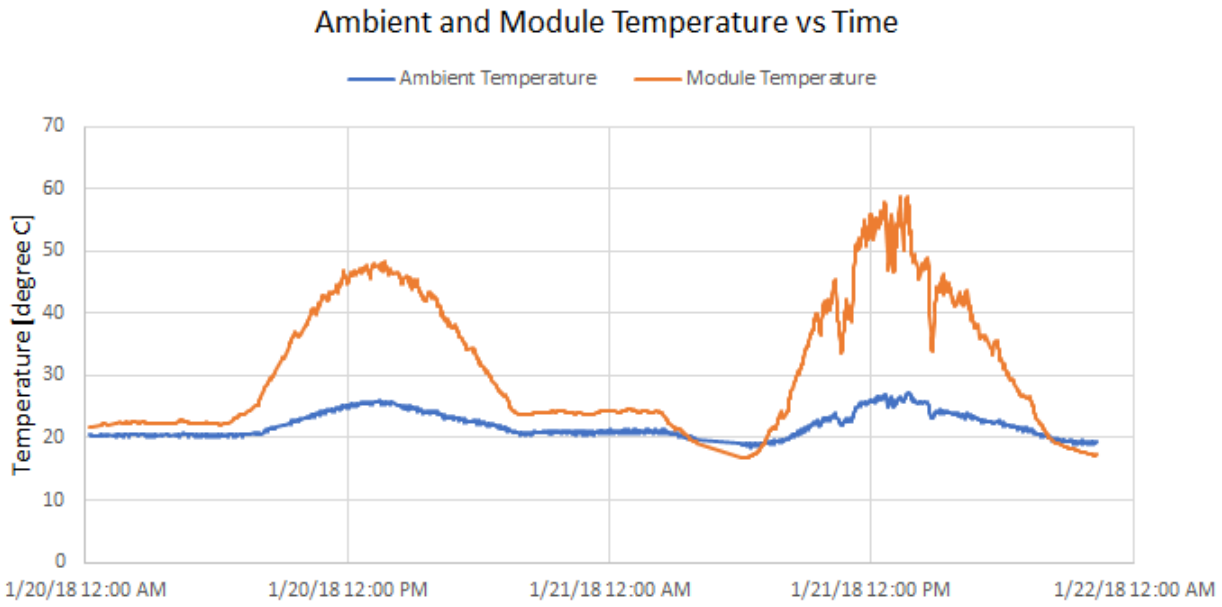

Figure 6.5: Sensor Node Version 2 Field Test Ambient and Module Temperature

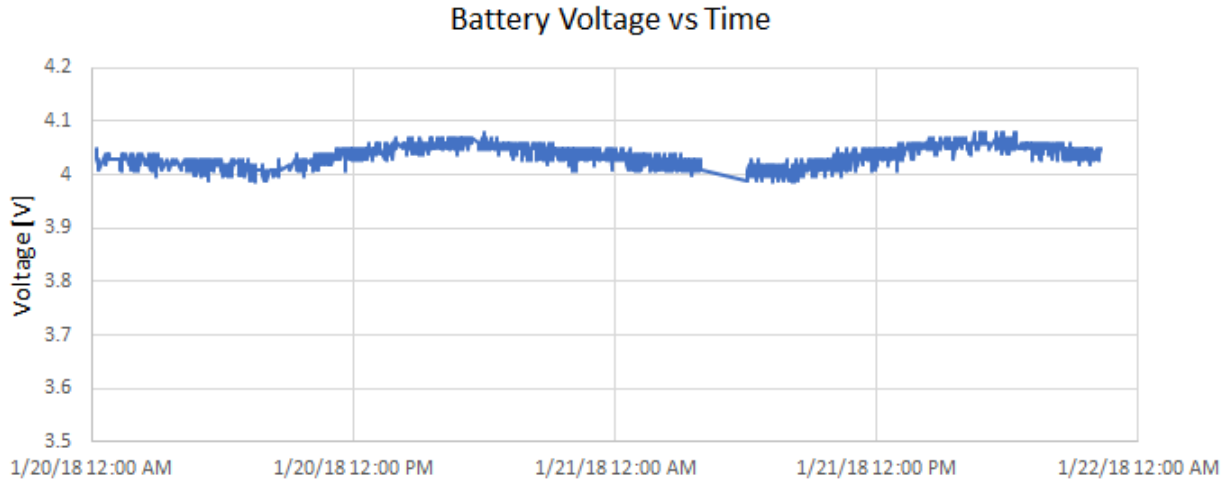

Figure 6.6: Sensor Node Version 2 Field Test Battery Voltage

Stellenbosch University https://scholar.sun.ac.za

The battery voltage of the sensor node is shown in Figure 6.6. There is a clear drop in voltage in the night-time and a rise in voltage in the day-time. This indicates that the small PV module placed on the sensor node bracket charges the sensor node battery sufficiently.

6.3 Sensor Node Version 3

6.3.1 Short-Circuit Field Measurements - Thin Film

Sensor node Version 3 was initially tested on a thin film module. A short-circuit current test similar to the test set-up mentioned in Section 6.2.1 was carried out. The module measured in the test is a SETSOLAR TF100 thin film module. The purpose of this test was to test the sensor node on a different type of PV module with different electrical characterizations. Thin film modules tend to produce a higher voltage and a lower current than similarly rated mono-crystalline modules.

The test was carried out to observe the sensor node's capabilities of measuring low current producing PV modules. The TF100 module has a rated short-circuit current of 1.65 A and a current at maximum power of 1.29 A at STC. The test set-up is shown in Figure 6.7.

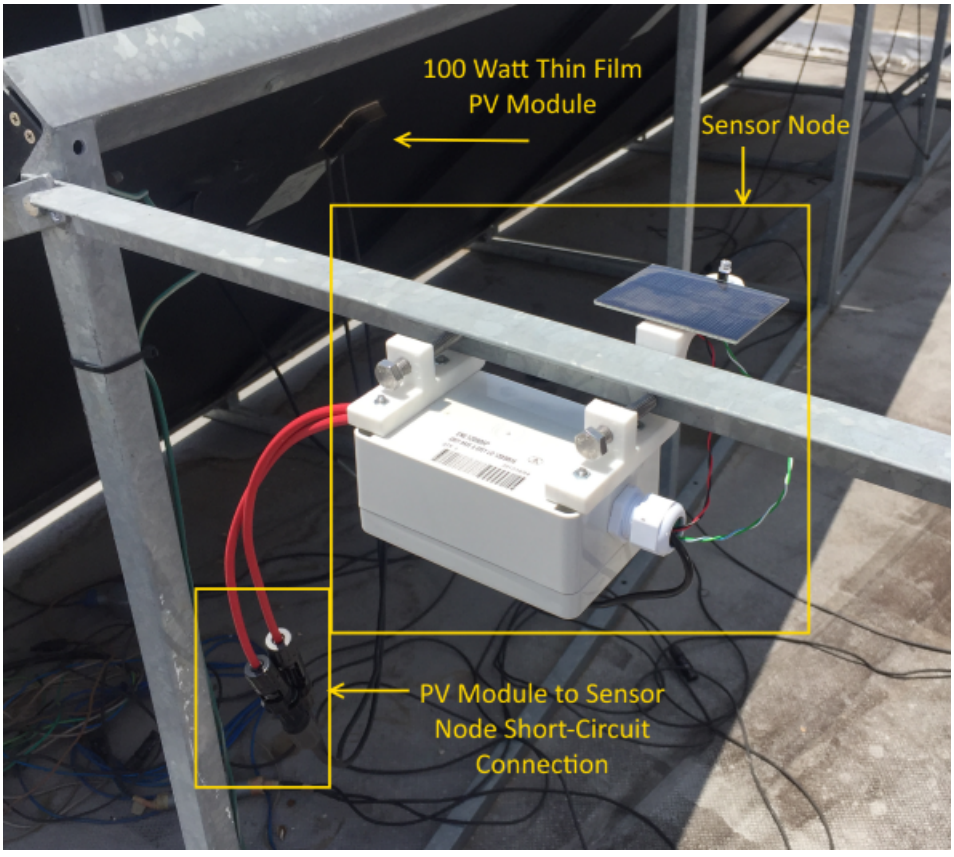

Figure 6.7: Field Test Set-up for Sensor Node Version 3 Short-Circuit Configuration - Thin Film PV Module

Short-circuit current and irradiance measurements that were taken between 00:00:00 am on 5 March 2018 and 11:59:59 pm on 8 March 2018 are shown in Figure 6.8 and Figure 6.9.

Stellenbosch University https://scholar.sun.ac.za

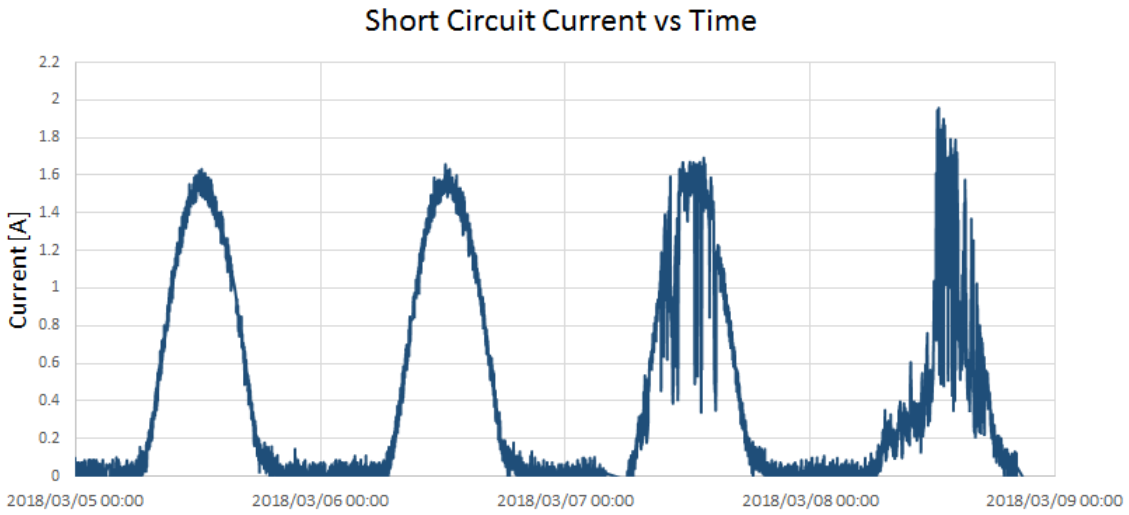

Figure 6.8: Sensor Node Version 3 Thin Film Module, Field Test Short-Circuit Current

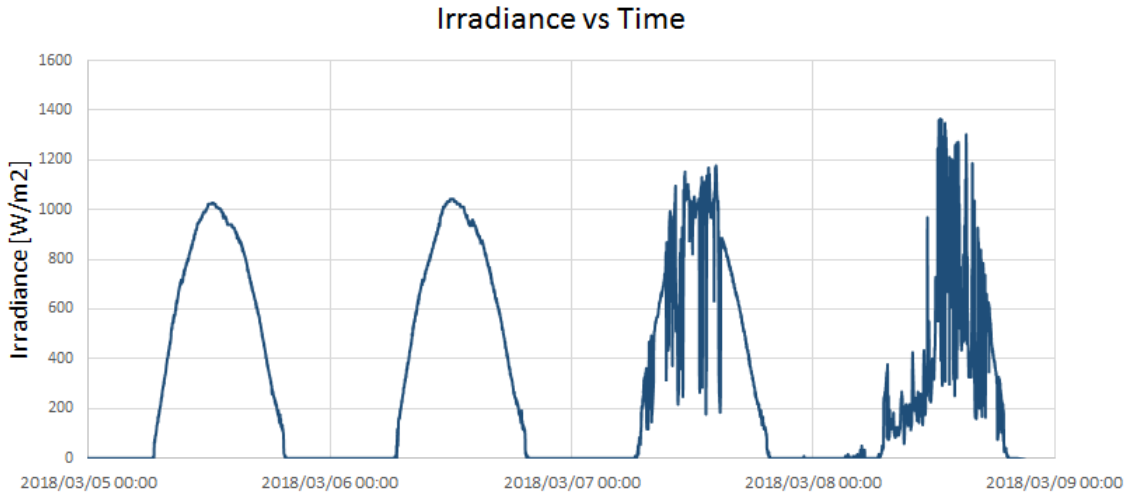

Figure 6.9: Sensor Node Version 3 Thin Film Module, Field Test Irradiance

Figure 6.8 and Figure 6.9 indicate that there were two clear days, one overcast day and one day with intermittent clouds. The current reaches a maximum of 1.63 A on the clear days and a maximum of 1.95 A on the day with intermittent clouds. The maximum current is higher on the day with intermittent clouds due to a phenomenon referred to as "lensing". Lensing is when diffuse and scattered irradiance from clouds adds to the direct irradiance resulting in a higher irradiance reading than on clear days.

There is a direct correlation between the short-circuit current and the irradiance graphs. The current-measurement graph contains more noise when compared to Figure 6.2. This is due to the fact that the current sensor has a full resolution of 10 A and only a tenth of that is used when measuring around 1 A. However, the correlation between the graphs is clear and the high level of detail, captured after small changes, is demonstrated.

Stellenbosch University https://scholar.sun.ac.za

6.3.2 Short-Circuit Field Measurements - Mono-crystalline

Sensor node Version 3 was tested on the same mono-crystalline PV module that Version 2 was tested on in Section 6.2.1. The PV module was similarly connected in short-circuit configuration. The purpose of this test was to collect measurement data over a longer period to test the durability, accuracy over time, and battery level of the sensor node. The test set-up is shown in Figure 6.10.

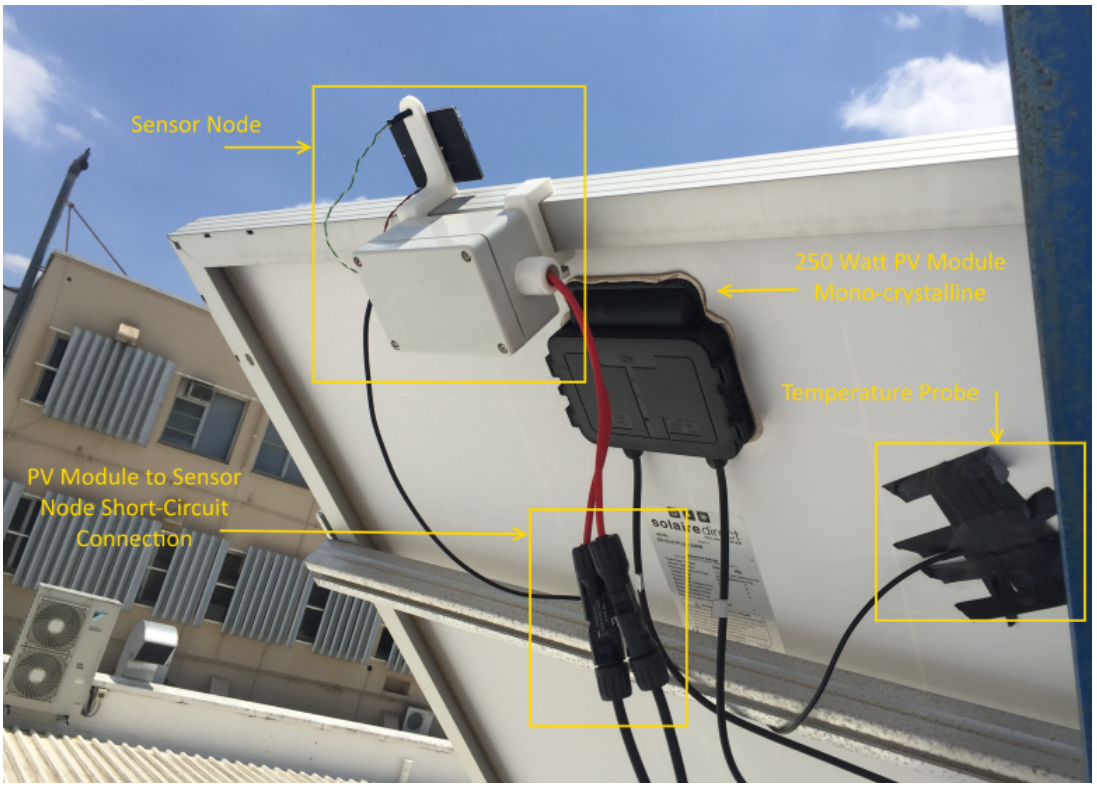

Figure 6.10: Field Test Set-up for Sensor Node Version 3 Short-Circuit Configuration - Mono-crystalline PV Module

Tests were carried out for a period of 10 days between 12 March 2018 and 22 March 2018. The short-circuit current graph for measurements taken between 00:00:00 am on 12 March 2018 and 11:59:59 pm on 22 March 2018 can be seen in Figure 6.11.

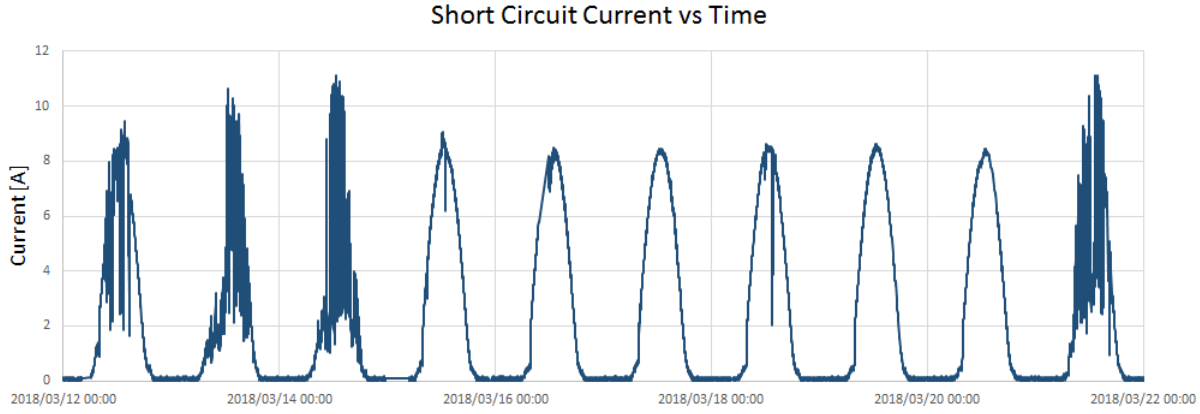

Figure 6.11: Sensor Node Version 3 Mono-crystalline Module, Field Test Short-Circuit Current

Stellenbosch University https://scholar.sun.ac.za

Irradiance measurements that were taken over the same period can be seen in Figure 6.12. Figure 6.11 demonstrates that there were clear days, cloudy days and days with intermittent clouds. There is a clear correlation between the short-circuit current and irradiance measurements.

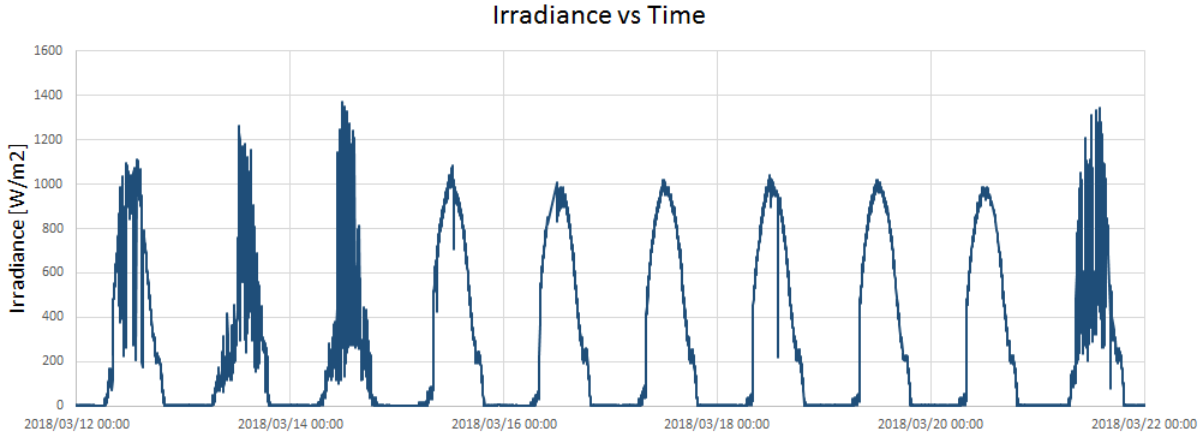

Figure 6.12: Sensor Node Version 3 Mono-crystalline Module, Field Test Irradiance

The shape of the irradiance measurement graph for clear days differ slightly from the shape of the current graph. Upon investigation it was found that the angle of the collector on the photodiode was not exactly the same as the angle of the PV module collector. The angle difference was approximately 4°. This highlights the importance of mounting the photodiode collector surface at the same angle as the PV module surface.

The ambient and module temperature measurements are shown in Figure 6.13. Module temperatures reached almost 60°C and went as low as 11°C. The vast difference between the module temperature and ambient temperature is obvious. The module temperature is much higher than the ambient temperature in the daytime which highlights the importance of measuring module temperature and not just ambient temperature when monitoring the health and performance of PV modules.

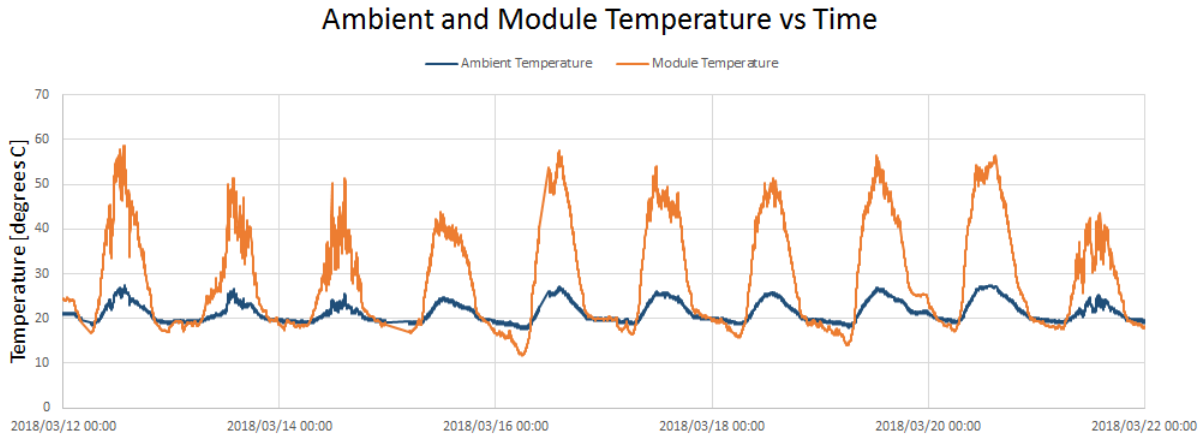

Figure 6.13: Sensor Node Version 3 Mono-crystalline Module, Field Test Ambient and Module Temperature

Stellenbosch University https://scholar.sun.ac.za

The sensor node battery voltage measurements can be seen in Figure 6.14. The battery voltage remained consistently between 3.85 V and 4.1 V for the duration of the 10-day test period. The overall voltage dropped during overcast days, but regained normal levels during clear days. Figure 6.14 clearly illustrates how the voltage level decreases during night-time and increases during the day-time when the battery is charged by the 500 mW PV module and the MCP73831 charge controller IC.

The break in data, occurring on the 15th of March 2018 between 12am and 4 am, was the result of a loss of Internet connectivity on the gateway side. The impact of the break in data can be seen in the level of battery drop; this is the result of the sensor node not receiving an acknowledge message from the gateway. This causes the sensor node to retake a set of measurements without entering sleep mode until an acknowledge message is received.

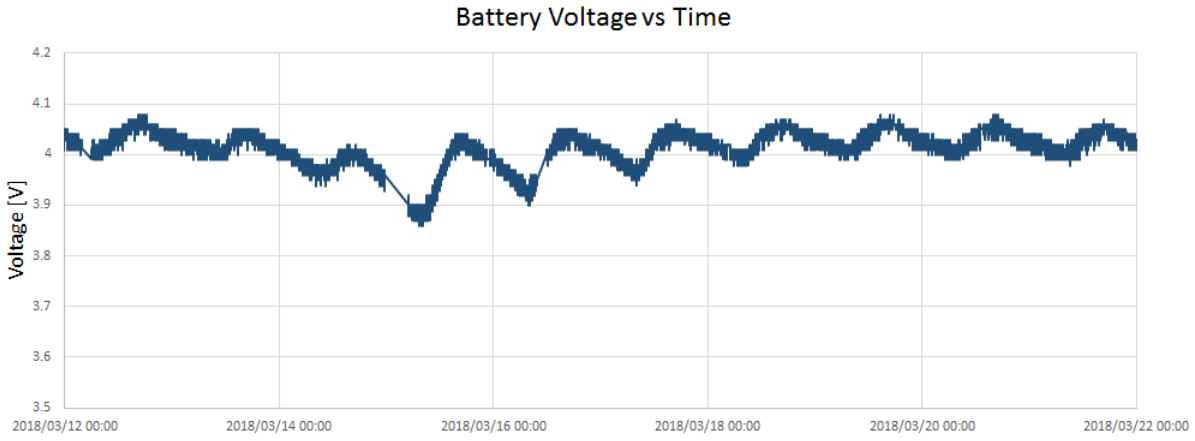

Figure 6.14: Sensor Node Version 3 Mono-crystalline Module, Field Test Battery Voltage

6.3.3 Fixed Resistor Field Measurements

All of the previous field tests measured a PV module in short-circuit configuration. For this test a fixed resistor was added which serves as a load that draws power from the PV module. The purpose of this test was to evaluate the sensor node measurement capabilities when the PV module is connected to an actual load, thus measuring voltage and current.

The test set-up of the PV module connected to the resistor load with the sensor node connected in series and parallel is shown in Figure 6.15. The PV module used is the same 240 Wp mono-crystalline module used in some of the previous tests. The resistor used is a high power variable resistor. The resistance was set to a fixed value of 2.6 Ohm for the test.

Stellenbosch University https://scholar.sun.ac.za

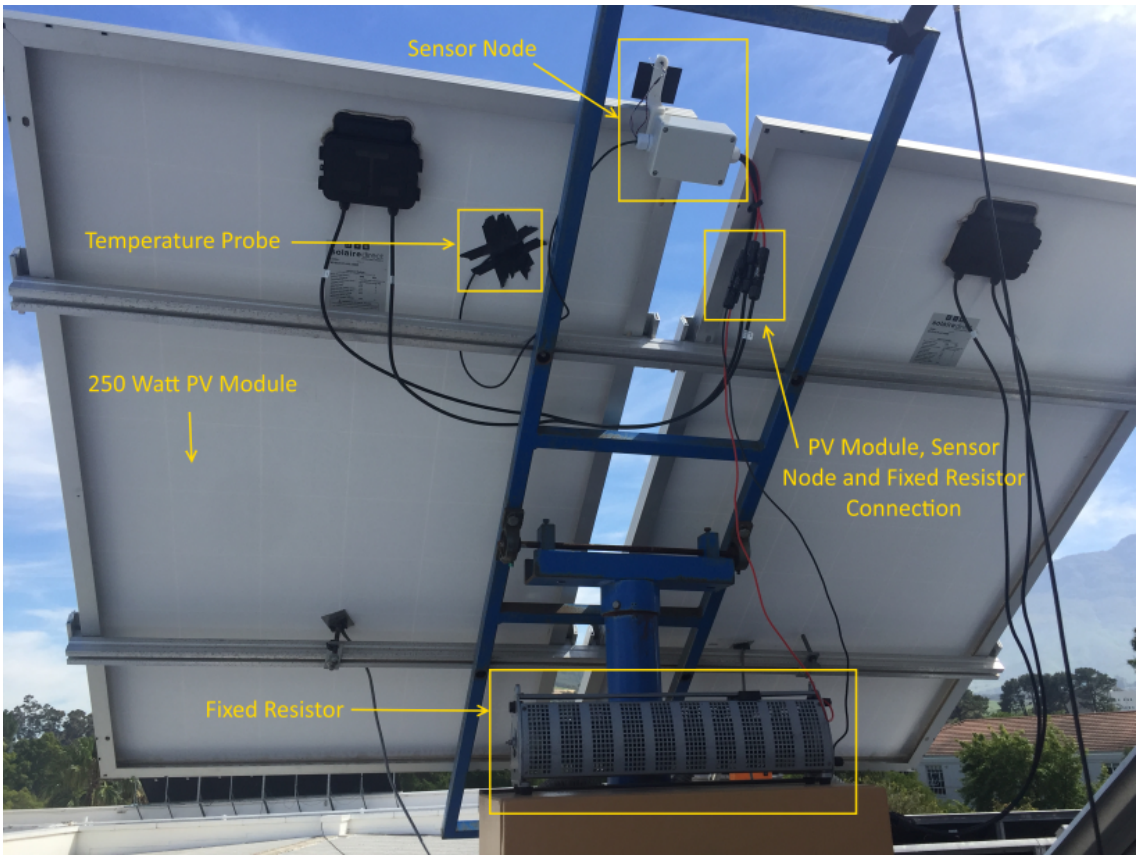

Figure 6.15: Field Test Set-up for Sensor Node Version 3 Fixed Resistor Configuration

The voltage and current measurements that were taken between 00:00:00 am on 3 April 2018 and 11:59:59 pm on 8 April 2018 are shown in Figures 6.16 and 6.17. The shapes of the voltage and current graphs are identical with the only difference being the values. The I-V curve of a resistor is a straight line in correlation with Ohm's law. For a fixed resistance the relationship between the voltage and current is linear, therefore the similar shape of the voltage and current graphs.

Voltage measurements for Version 2 and Version 3 of the sensor node is measured with a resolution of 0.05 V and an accuracy of 0.1 V. This is a 400% increase over Version 1 than can be attributed to the voltage technique used for Version 2 and Version 3. Isolating a digital signal is thus much more effective and accurate than isolating an analog signal.

Stellenbosch University https://scholar.sun.ac.za

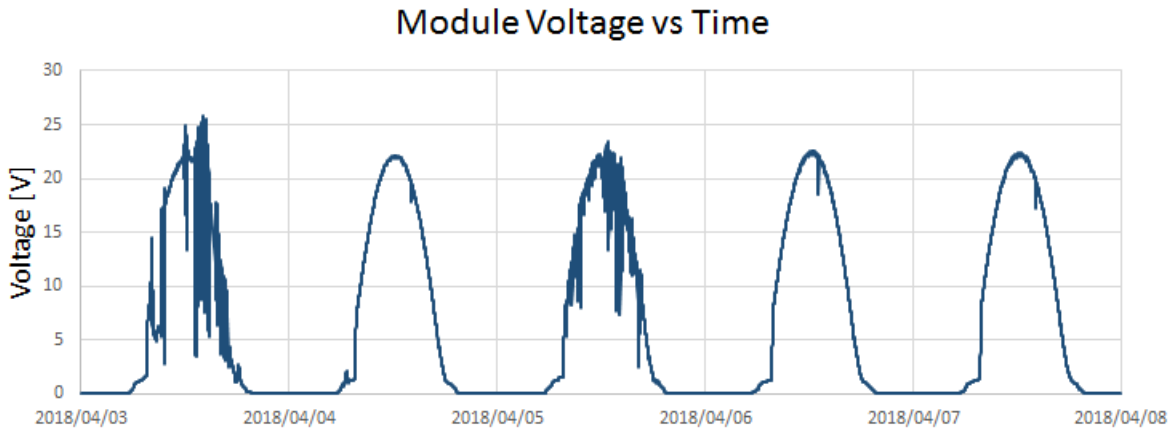

Figure 6.16: Sensor Node Version 3 Fixed Resistor Configuration, Field Test Voltage

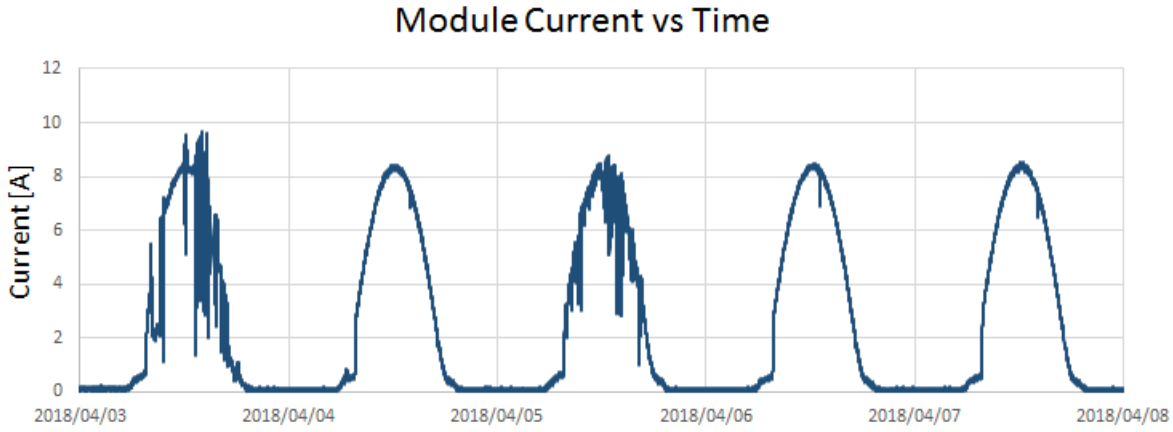

Figure 6.17: Sensor Node Version 3 Fixed Resistor Configuration, Field Test Current

The power graph shown in Figure 6.18 was obtained by multiplying the values of each instantaneous voltage and current measurement (P = V * I).

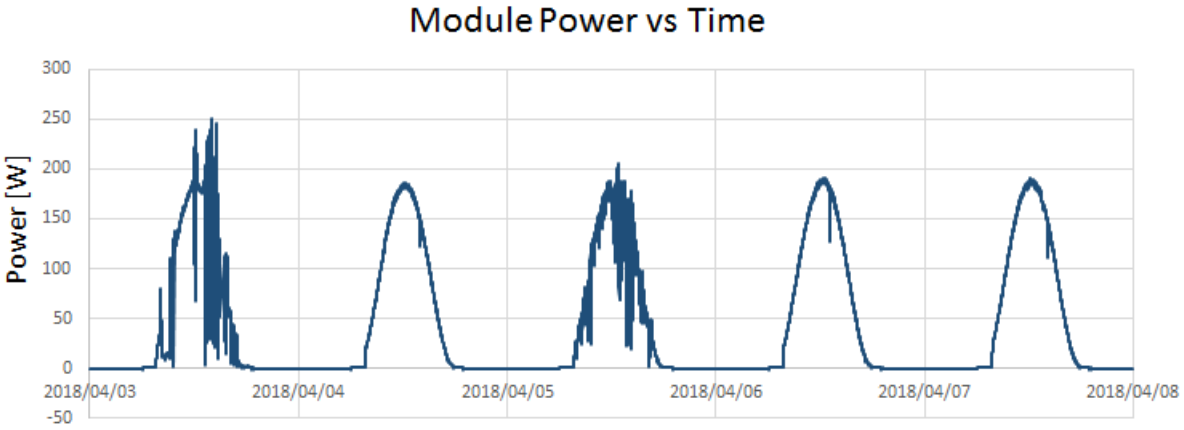

Figure 6.18: Sensor Node Version 3 Fixed Resistor Configuration, Field Test Power

Stellenbosch University https://scholar.sun.ac.za

From the power graph it is clear that the PV module is not operating at its maximum power on clear days. The operating power is lower than expected due to the PV module being connected to a fixed resistor. Each current value has a fixed voltage value that is given by Ohm's law for the fixed resistance. The I-V curve of a PV module, that has a specific maximum power point, is thus seldom at its maximum power point and hence the poor performance. This confirms the importance of having a MPPT (Maximum Power Point Tracker) that varies the voltage to be as close to the maximum power point on the I-V curve of the PV module as possible for the given conditions (irradiance).

6.4 Wireless Communication Performance

Wireless communication tests were carried out to evaluate the performance of LoRa in different configurations, scenarios and conditions. The same LoRa radio transceiver is used for Version 2 and Version 3 of the sensor node as well as the gateway as discussed in Chapter 4. The wireless communication tests were carried out with a gateway and a single sensor node.

6.4.1 Network Coverage

A network coverage test was done to evaluate the packet delivery ratio for different spreading factors at various locations. Tests were conducted in Stellenbosch, Western Cape, South Africa. Tests were carried out in the daytime with an air temperature ranging from 15°C to 25°C. The gateway was located on a steel structure on the rooftop of the 3rd floor of the Electrical and Electronic Engineering Department of Stellenbosch University. The height of the gateway is approximately 12 metres above ground level.

The antenna used on both the gateway and sensor node is a straight whip, 1/2 wave dipole, 3 dBi antenna. The sensor node was placed on 8 different locations around Stellenbosch. At each location the sensor was tested on spreading factor 7, 9 and 12. The sensor node sent 100 10-byte messages to the gateway on each of the three spreading factors at each location. The map of the LoRa network coverage field test is shown in Figure 6.19.

Stellenbosch University https://scholar.sun.ac.za

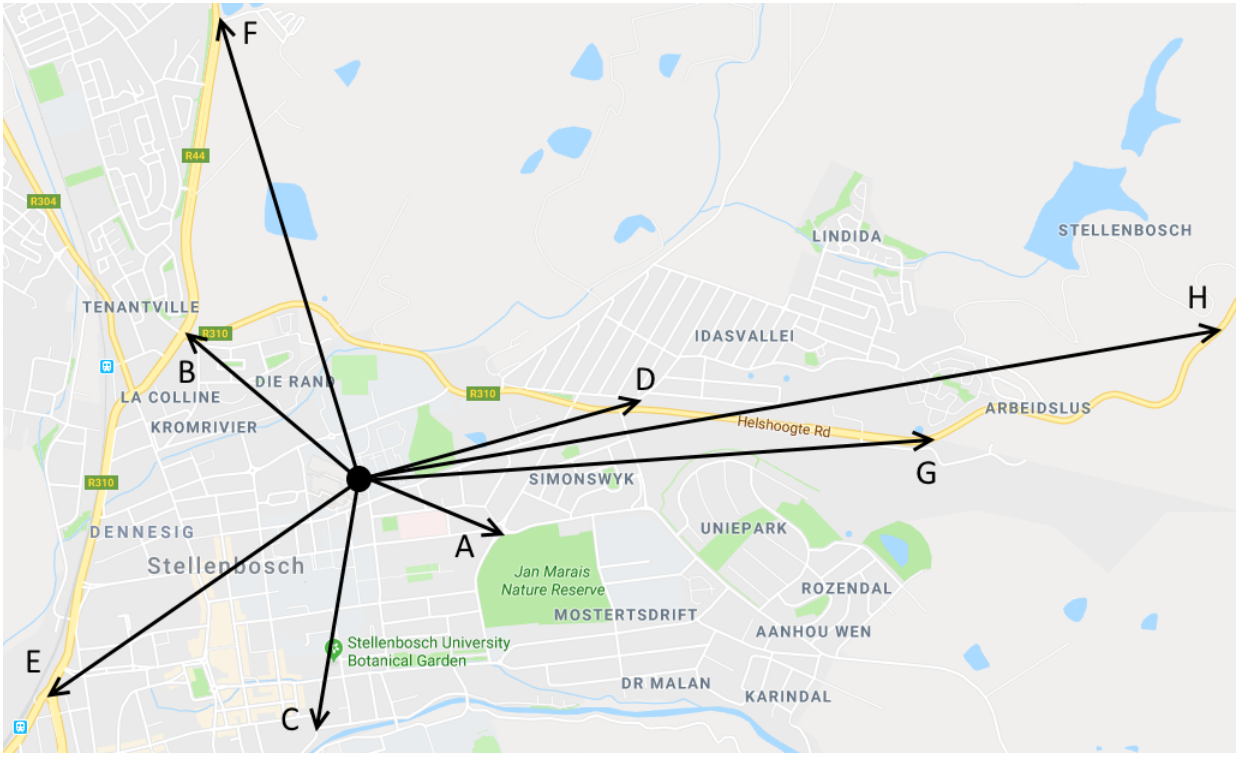

Figure 6.19: LoRa Network Coverage Field Test Map

The transmission power of the sensor node was set to 17 dBm and the bandwidth was set to 125 kHz; which are the default values specified in the LoRa transceiver datasheet [50]. The distance from the gateway to each test point as well as the elevation of each point and height difference with respect to the gateway are presented in Table 6.1. The elevation of the gateway is 132 metres above sea level.

Table 6.1: LoRa Network Coverage Field Test Location Information

Test Point	Distance	Elevation	ΔH
A	0.75 km	131 m	-1 m
B	1.03 km	121 m	-11 m
C	1.23 km	119 m	-13 m
D	1.35 km	151 m	19 m
E	1.71 km	100 m	-32 m
F	2.28 km	147 m	15 m
G	2.75 km	243 m	111 m
H	4.21 km	306 m	174 m

A graph containing the packet delivery ratio for the different spreading factors (SF) at each location is shown in Figure 6.20.

Stellenbosch University https://scholar.sun.ac.za

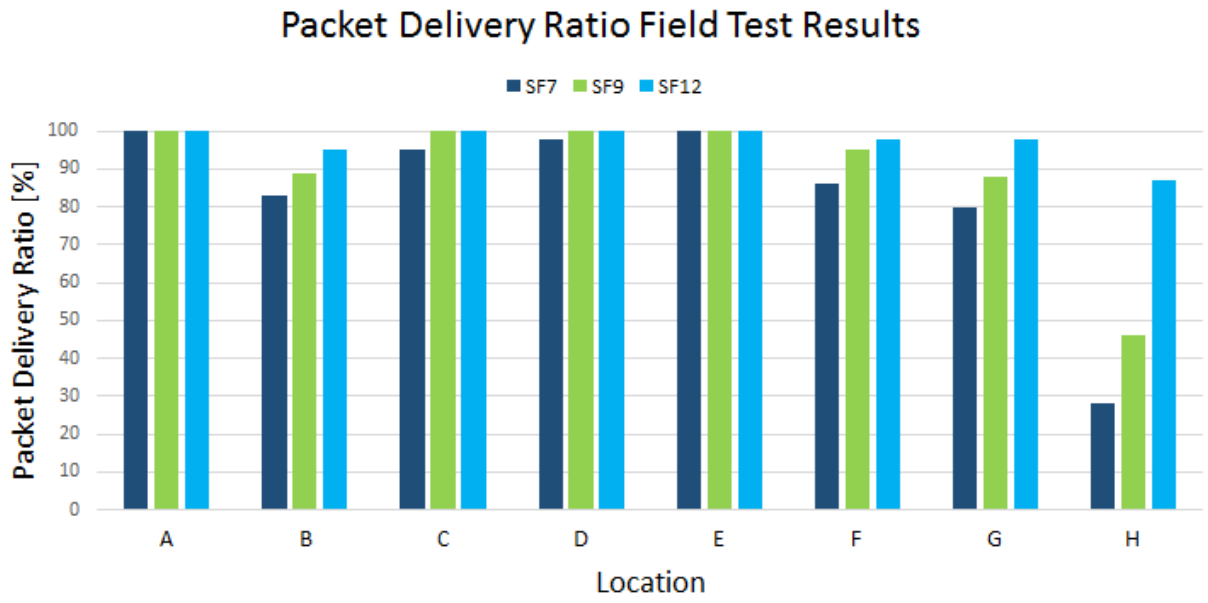

Figure 6.20: Packet Delivery Ratio for Network Coverage Field Test

The packet ratio for location B which is 1.03 km away from the gateway is significantly lower than that of location D which is located 1.35 km from the gateway. When viewing the elevation profile of both locations this phenomenon can be explained. The elevation profile of location B and D is shown in Figure 6.21.

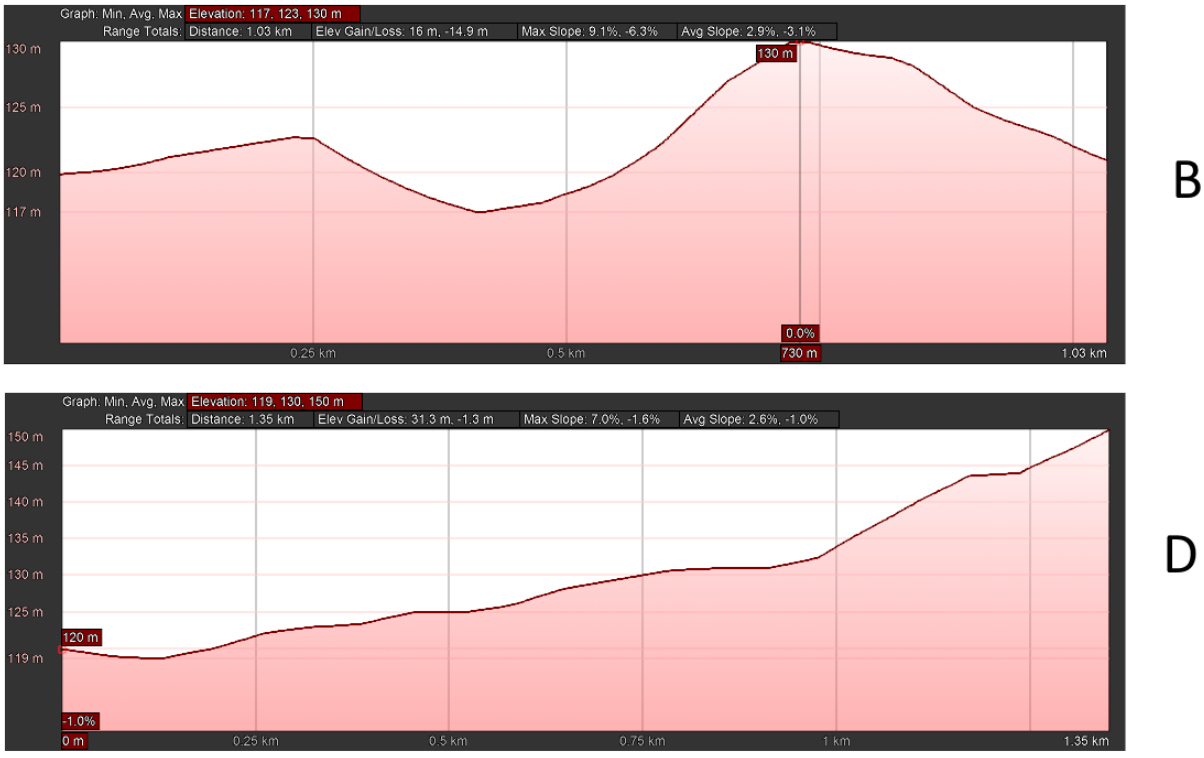

Figure 6.21: Location B and D Elevation Profile

Stellenbosch University https://scholar.sun.ac.za

Figure 6.21 depicts the landscape between location B and the gateway. It demonstrates the obstructed line-of-sight between location B and the gateway; while location D is in a more favourable position to communicate, unobstructed, with the gateway. The elevation profile only shows the profile of the ground level, all of the locations that were tested are located in a suburban area where buildings and other man-made obstacles are also present. Height and direct line-of-sight represent significant influential factors on packet delivery ratio.

6.5 PV Plant Field Test

To test the monitoring system as a whole, more sensor nodes were built to be installed on a fully functional PV installation. A total of fifteen sensor nodes were manufactured and assembled for testing. The sensor nodes were installed on a small PV plant located outside of Stellenbosch, Western Cape, South Africa. At the time of the testing the PV plant consisted of three strings. One string containing twenty 320 Watt PV modules and two strings containing fifteen 320 Watt PV modules. All of the PV modules are attached to a single axis tracking system.

The sensor nodes were placed sequentially from the 1st to the 15th PV module in the string containing twenty 320 Watt PV modules. Figure 6.22 shows the bottom view of one of the sensor nodes attached to one of the PV modules in the PV plant.

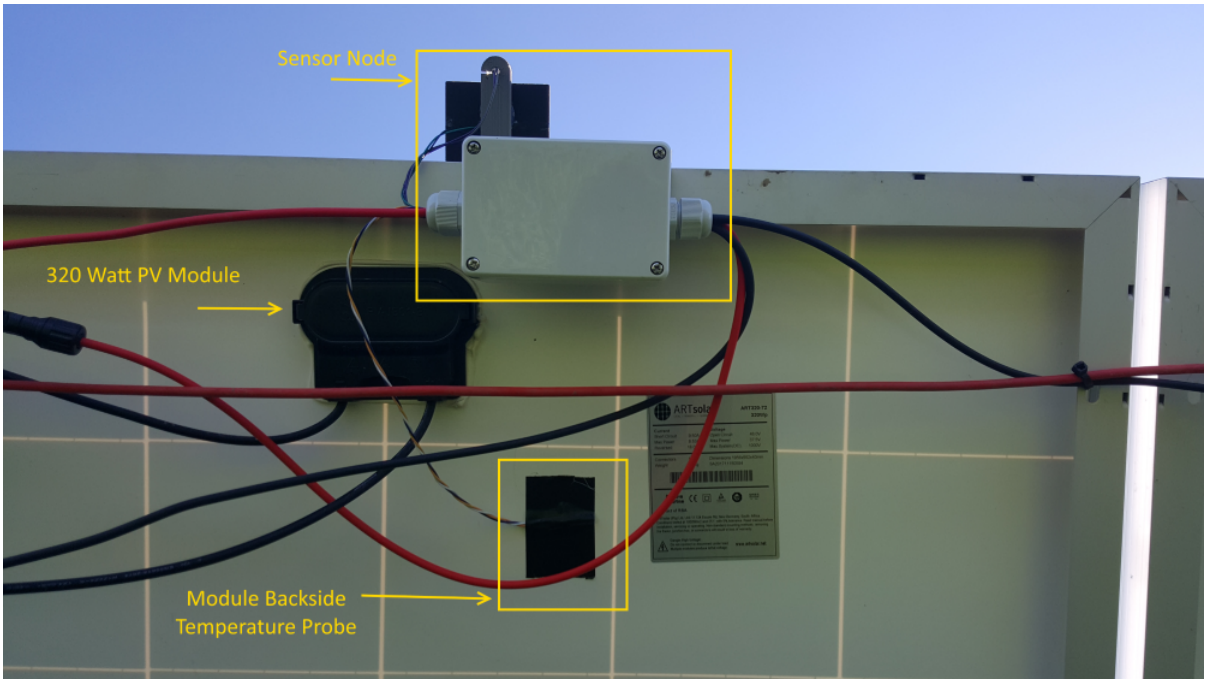

Figure 6.22: Sensor Node Bottom View PV Plant Field Test

The side-bottom and side-top view of the sensor nodes installed on the various PV modules on the PV plant are shown in Figure 6.23 and 6.24.

Stellenbosch University https://scholar.sun.ac.za

Figure 6.23: Sensor Node Side-Bottom View PV Plant Field Test

Figure 6.24: Sensor Node Side-Top View PV Plant Field Test

Stellenbosch University https://scholar.sun.ac.za

The gateway was placed inside of a 6 meter shipping container that contains the inverter that the three strings connect to. In order to store the measurement data on the cloud server, Internet connectivity was established by connecting the gateway to a GSM modem via an Ethernet cable. The inverter connecting the three strings is a SMA Sunny Tripower 20 kW three phase grid tied inverter. Each sensor node is programmed to send a set of measurements every minute. The gateway stores each set of measurements in a database located on the cloud server. Data is viewed and analysed off-site with the data analysis GUI application.

6.5.1 Data Analysis GUI Application

6.5.1.1 Layout View

The layout view of the data analysis GUI application displays the entire layout of the PV installation and the PV installations to which the monitoring station is fitted. Each string in the PV plant has a number assigned to it, and PV modules within each string is numbered sequentially. The layout of the PV plant where field tests were carried out as presented in the GUI is shown in Figure 6.25.

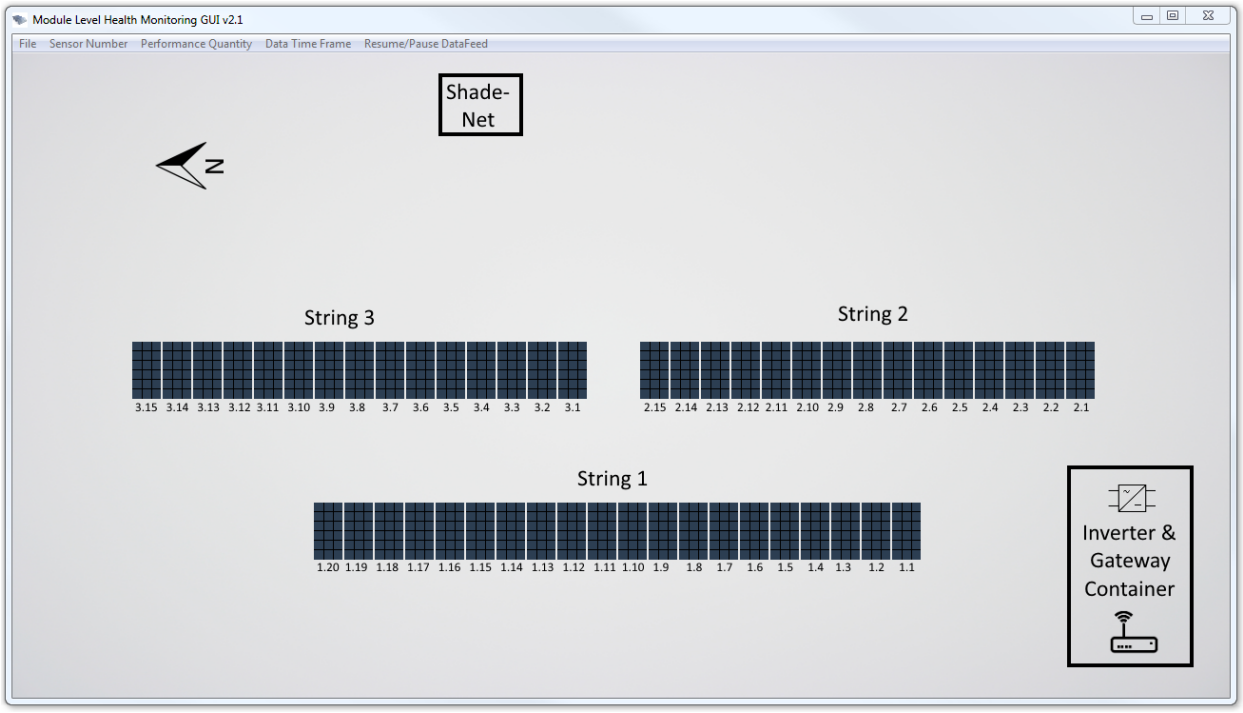

Figure 6.25: PV Plant Layout View Data Analysis GUI

Sensor Nodes were placed on PV modules 1.1 to 1.15 which is the 1st to 15th PV module in String 1. The scaled layout view displays live data of a specific string or part of a specific string. The voltage, power and module backside temperature are shown for each measured PV module. The string current, irradiance, ambient temperature and the latest update time for each string are also presented.

The health status of each PV module is indicated as a colour background on each measured module in the scaled layout view. The health status of each module is calculated by means of the fault detection model that was discussed in Section 3.3. The various health status assignments with the associated colour representations are presented in Table 6.2.

Stellenbosch University https://scholar.sun.ac.za

The efficiency loss is calculated with measured environmental and electrical performance data. The formula for the efficiency loss as discussed in Section 3.3 is:

$$\eta_{Loss} = \eta_{Estimated} - \eta_{Measured} + \kappa_{Th} \tag{6.1}$$

Table 6.2: GUI PV Module Health Status Assignment

Efficiency Loss (η_{Loss})	Health Status	Colour Representation
0 % - 0.9 %	Good	Green
1 % - 2.9 %	Minor Fault	Yellow
3 % - 6.9 %	Fault	Orange
7 % and greater	Critical Fault	Red

The GUI updates and recalculates all of the data shown in the scaled layout view at 10 second intervals. There is a status message window in the scaled layout view where certain messages regarding the status of any given sensor node and/or PV module appear. The status messages include: detected tampering, low battery warning, lost connection and critical faults on PV modules.

The sensor number which corresponds to a specific PV module within the PV plant as well as the status message and a date-time stamp appears in the window to indicate when and where a certain status event occurs. The scaled layout view in a partially shaded string scenario that occurred before sun-set on 20 September 2018 at 17:27:45 pm is shown in Figure 6.26.

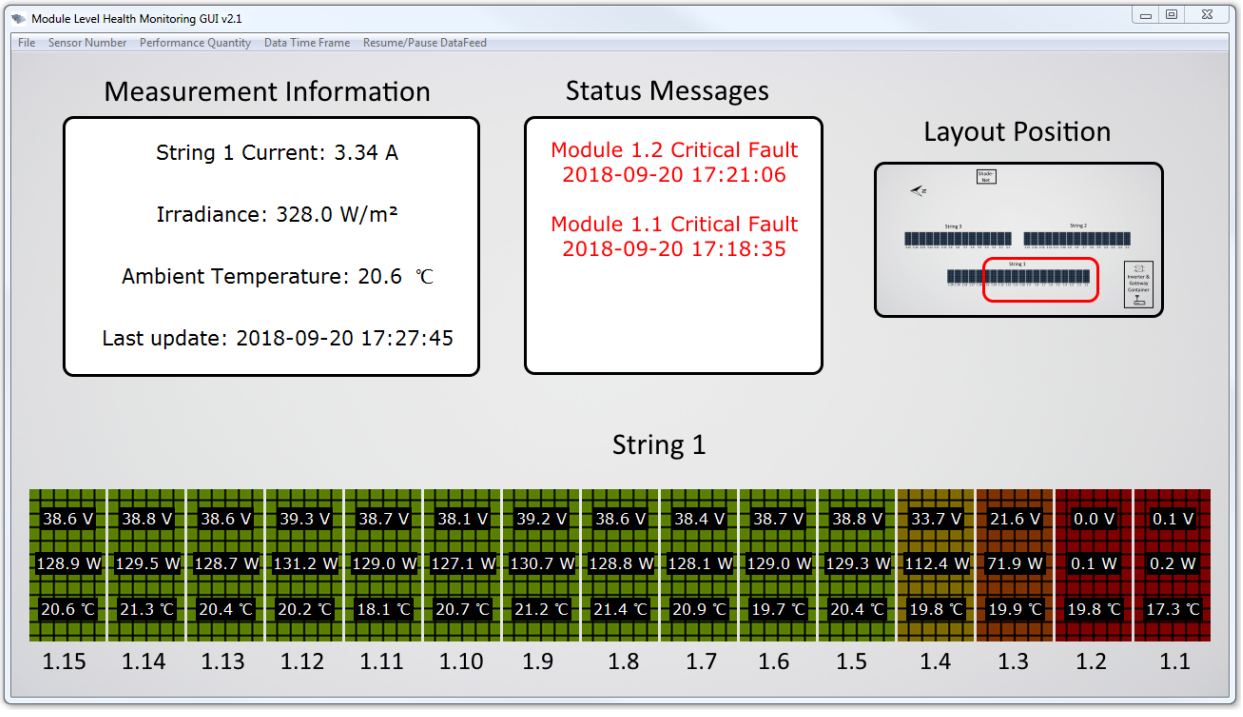

Figure 6.26: PV Plant Scaled Layout View Data Analysis GUI - Partially Shaded String Scenario

6.5.1.2 Graph View

The graph view enables the user to view any historical performance data that was measured and/or calculated by the application. The following data can be viewed in graph form:

Stellenbosch University https://scholar.sun.ac.za

- Voltage
- Current
- Irradiance
- Ambient Temperature
- Module Temperature
- Battery Voltage
- Power
- Efficiency (Estimated and Measured)

A range of different time-frames and the specific sensor node number can be selected. The power measurement graph of sensor node 1.13 for a 1 week interval is shown in Figure 6.27. The interval is from 2018/10/27 to 2018-11-02.

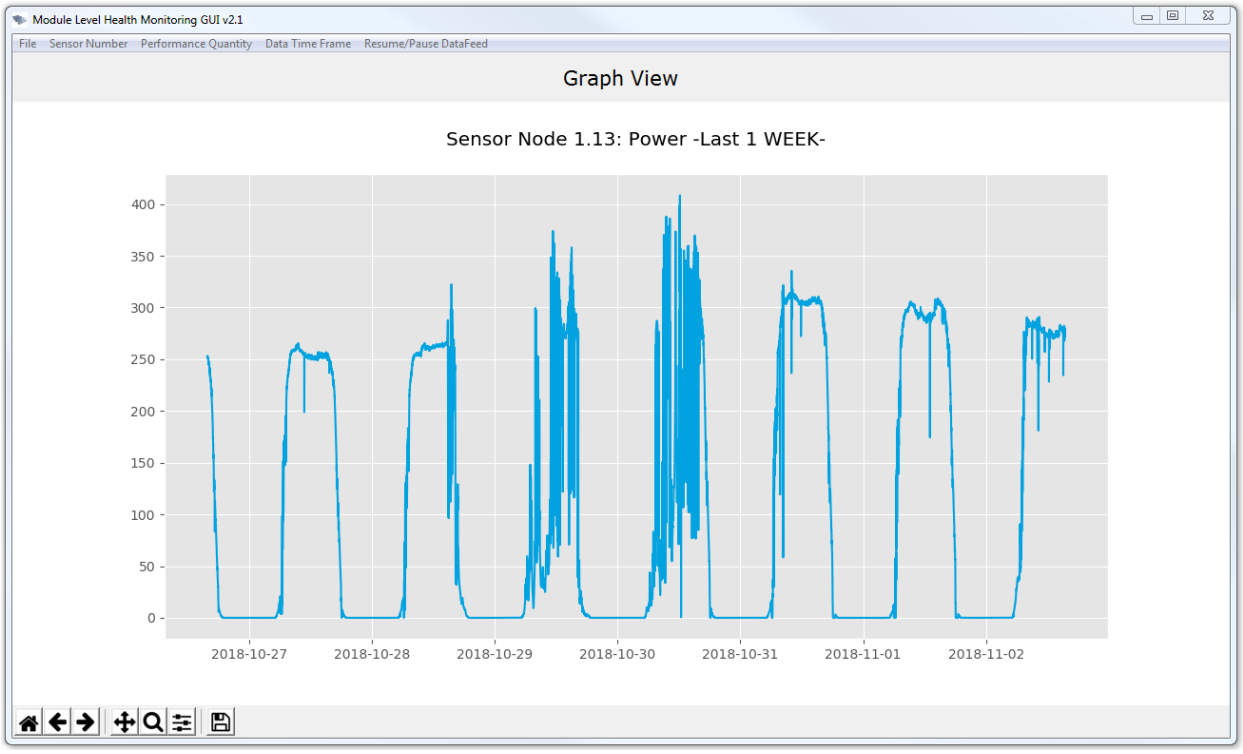

Figure 6.27: PV Plant Graph View Data Analysis GUI - Sensor 1.13 Power 1 Week

Orientation: The orientation of the single-axis tracking system for a 24 hour period is shown in Figure 6.28. The resolution of the accelerometer is 3.5 degrees. Zero degrees is defined as horizontal which is the position of the tracking system on solar noon (12:29 am for Stellenbosch on 15 November 2018). The 24-hour period of recorded data shown in Figure 6.28 is from solar noon on 14 November to solar noon on 15 November. The tracker moves to 18 degrees during the night time (19:40 pm - 05:20 am). This is done to keep the PV modules stable during high winds that might occur during night time, the angle however is not completely flat (zero degrees) which allows water particles that form during the night to roll off, removing dust soiling from the modules.

Stellenbosch University https://scholar.sun.ac.za

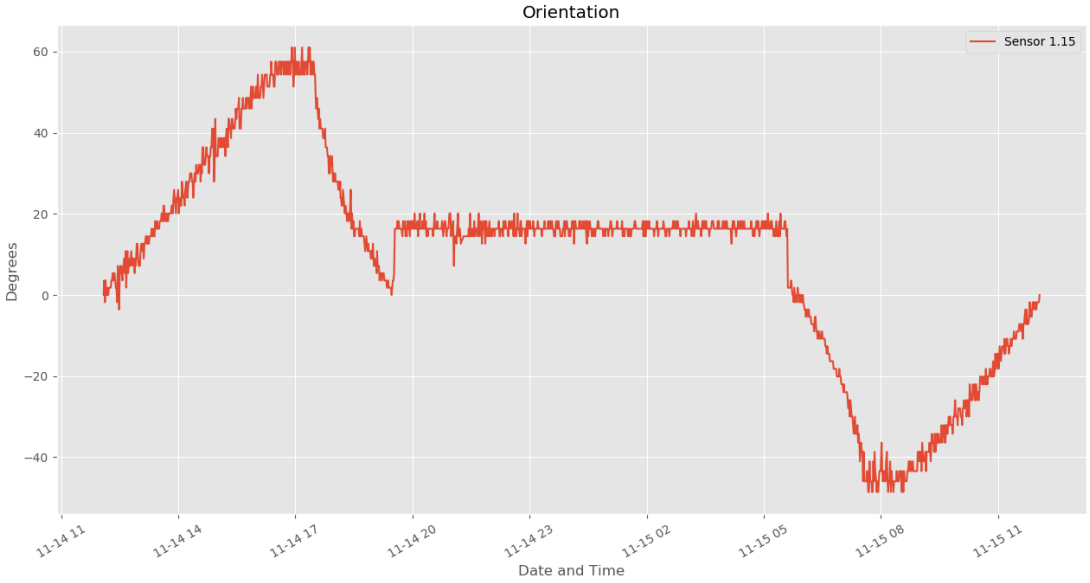

Figure 6.28: PV Plant Shading Experiment - Voltage

Shading Scenario: The voltage graph of the partially shaded string scenario presented in Figure 6.26 is shown for a 40 minute period in Figure 6.29. The voltage drop of PV modules 1.1 to 1.6 can clearly be observed. The voltage drop occurred because of a shadow caused by an obstacle that blocks the sunlight on a few PV modules for a short period at the end of each day. Just before sunset, a sudden and transient rise in voltage from these PV modules occurs after the shadow passes.

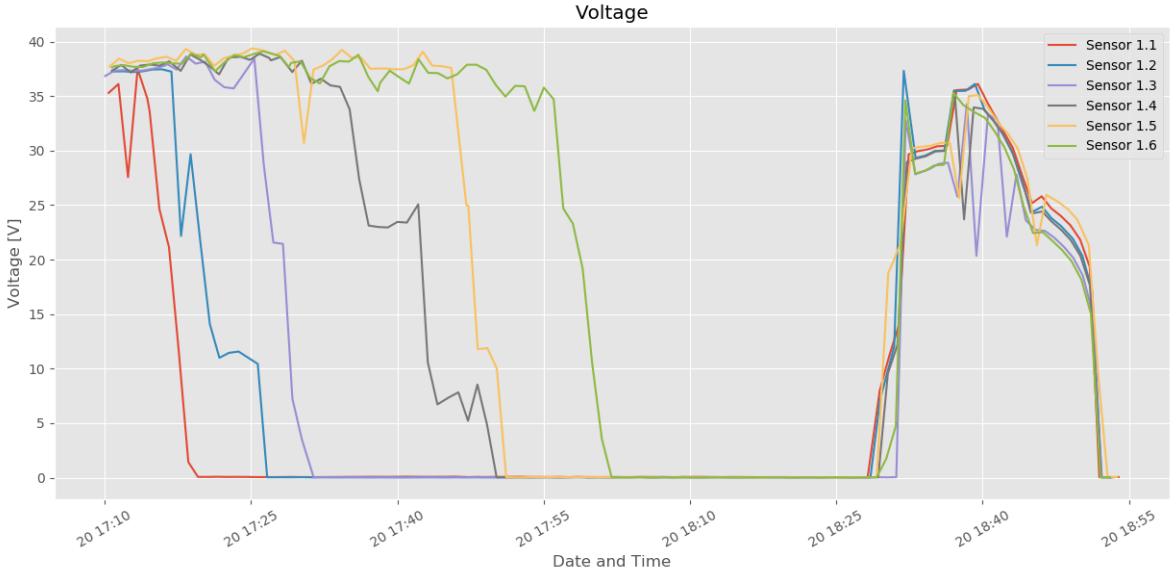

Figure 6.29: PV Plant Graph View Data Analysis GUI - Partially Shaded String Scenario - Voltage

The module temperature graph for the same scenario over the same period is shown in Figure 6.30. The temperature drop can clearly be observed; module temperatures drop in the same order as the voltage; with a short time delay compared to when the voltages dropped.

Stellenbosch University https://scholar.sun.ac.za

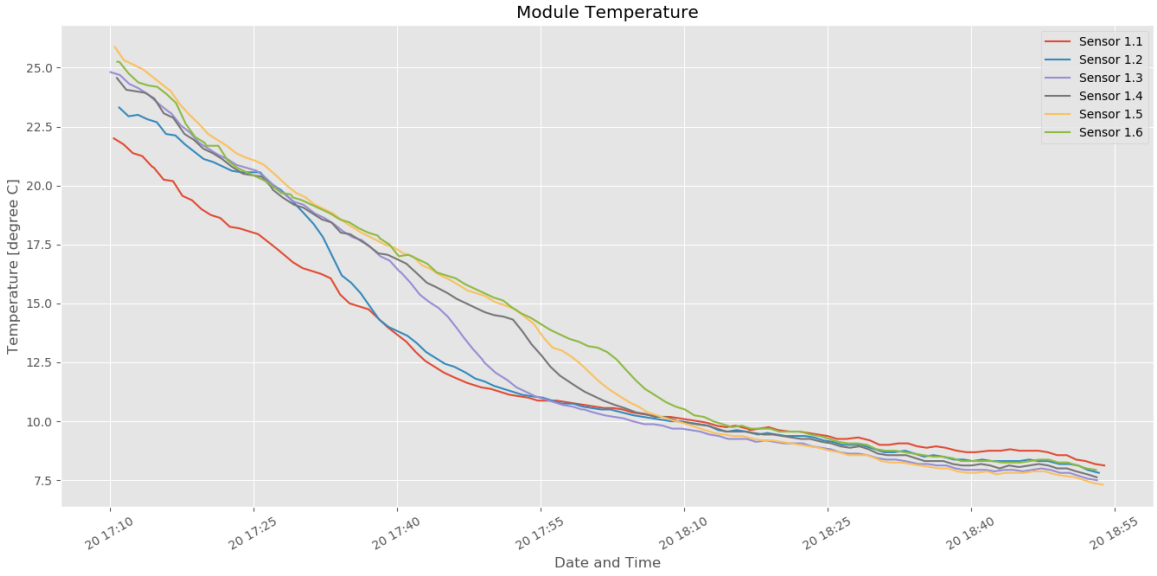

Figure 6.30: PV Plant Graph View Data Analysis GUI - Partially Shaded String Scenario - Module Temperature

The string current graph for the same scenario over the same period is shown in Figure 6.31. The current decreases as the shade moves over the various PV modules.

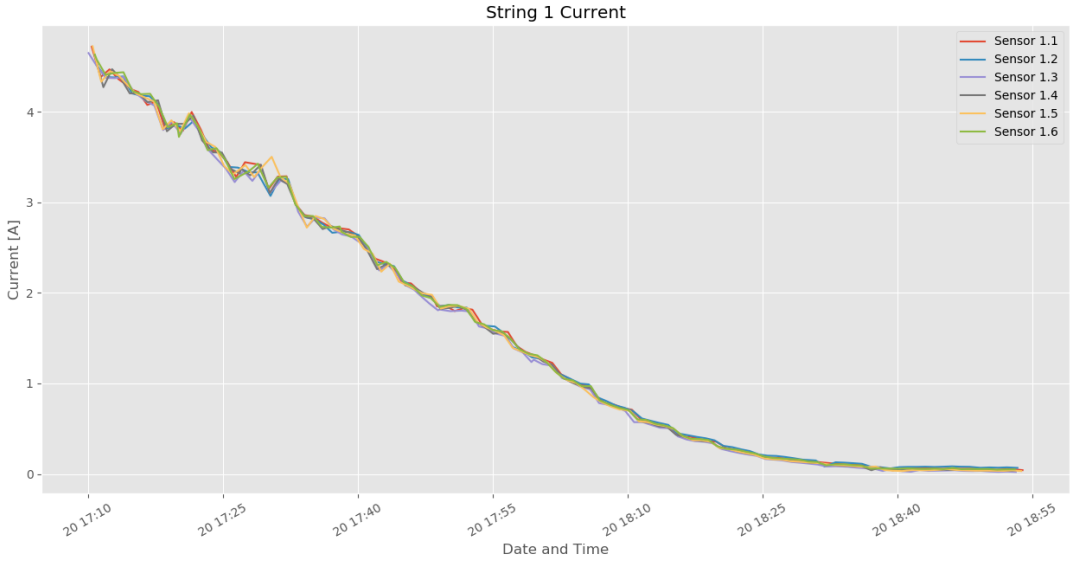

Figure 6.31: PV Plant Graph View Data Analysis GUI - Partially Shaded String Scenario - String 1 Current

Soiling Scenario: A soiling scenario was observed on 24 August 2018. The soiling was caused by bird droppings on PV module 2 within string 1. A side-view photo of string 1 indicating the soiling is shown in Figure 6.32. A front-view photo of PV module 1.1 and 1.2 indicating the relative size of the soiling is shown in Figure 6.33.

Stellenbosch University https://scholar.sun.ac.za

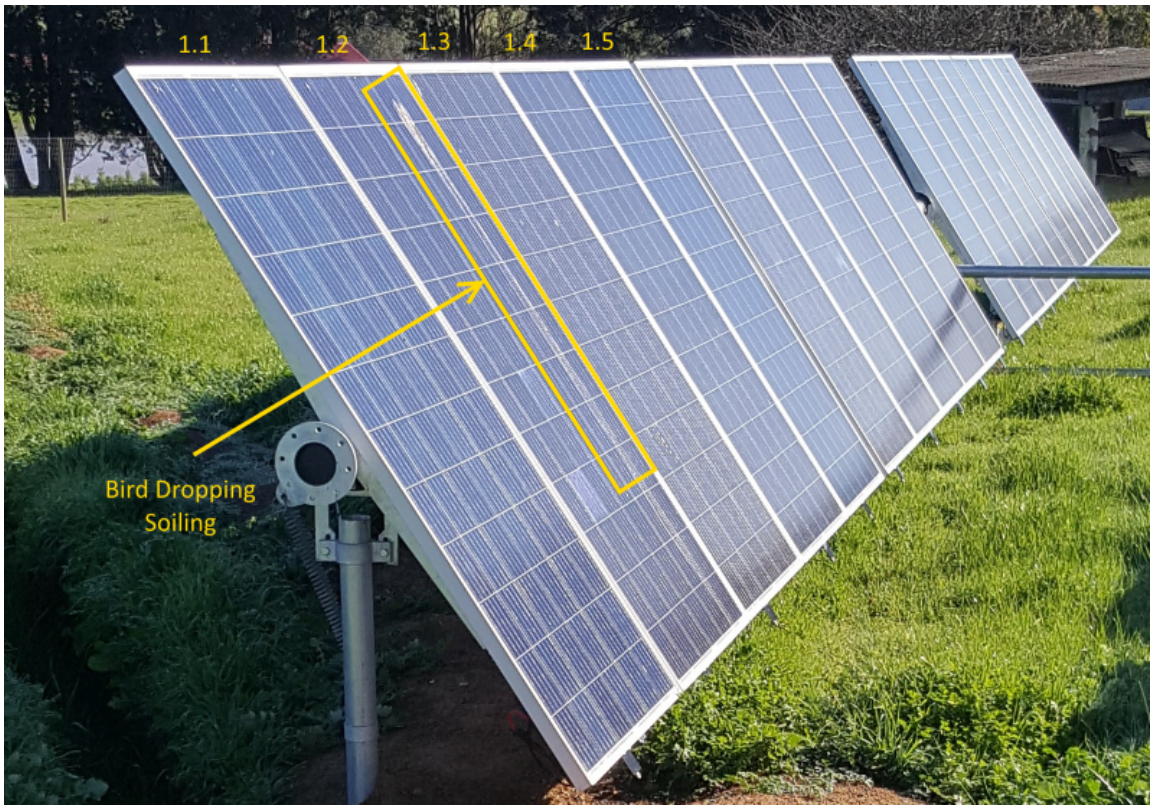

Figure 6.32: String 1 Side-View Photo Indicating Soiling on Module 1.2

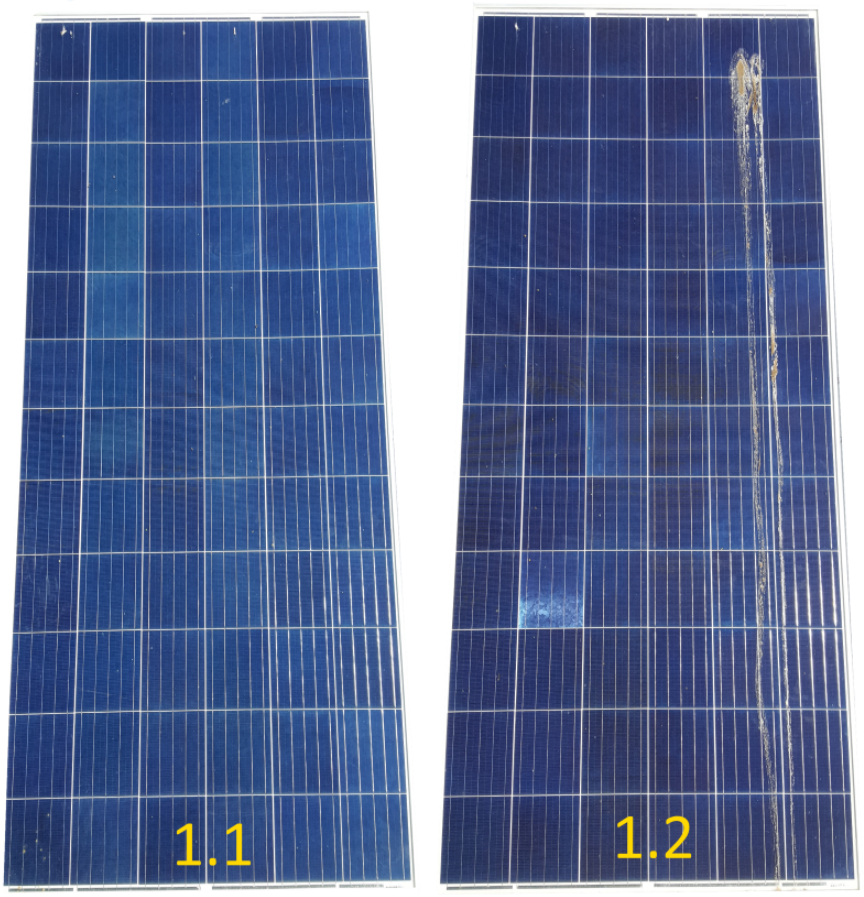

Figure 6.33: String 1 Front-View Photo Indicating Soiling on Module 1.2

Stellenbosch University https://scholar.sun.ac.za

A graph showing the voltage measurement for PV modules 1.1 and 1.2 on 24 August 2018 between 11:00 am and 18:00 pm is shown in Figure 6.34.

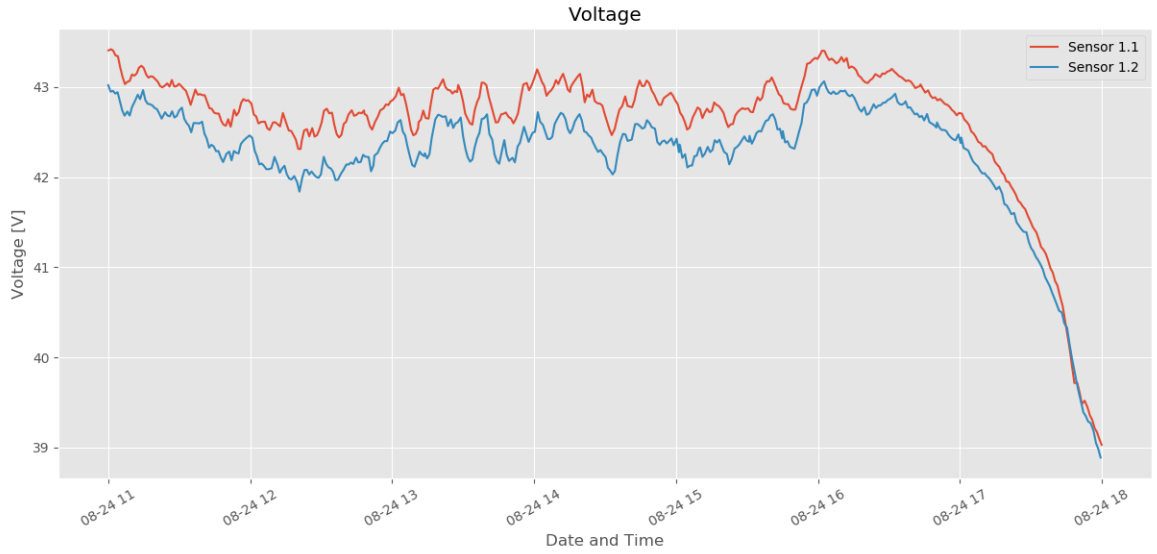

Figure 6.34: PV Plant Graph View Data Analysis GUI - Soiling Scenario - Voltage Graph

PV module 1.2 clearly has a lower voltage than module 1.1, due to soiling. The voltage difference reaches a maximum of 0.5 V. At the time when the voltage difference between the modules was 0.5 V, the string current was 7 A. The instantaneous power for module 1.1 was thus 297.5 Watt and module 1.2 was 294 Watt. This results in a power decrease of approximately 1.2% on module 1.2 due to the soiling.

PV module 1.2 was cleaned, and the soiling removed on 28 August 2018. The voltage graph of PV modules 1.1 and 1.2 on 28 August 2018 between 11:00 am and 18:00 pm is shown in Figure 6.35. There is a clear improvement in the voltage of PV module 1.2 after being cleaned.

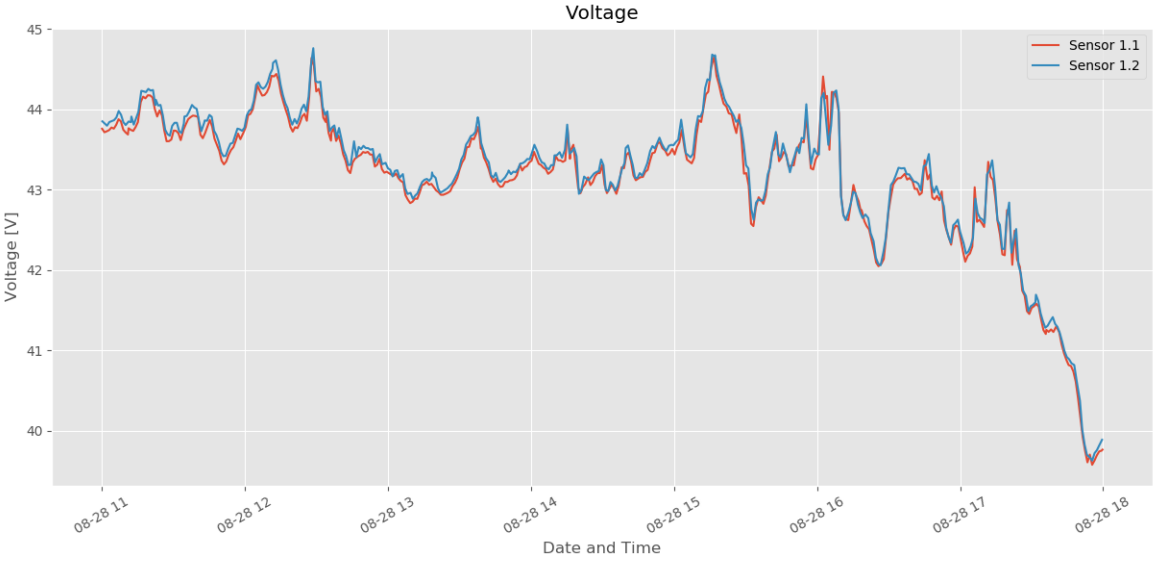

Figure 6.35: PV Plant Graph View Data Analysis GUI - Soiling Scenario - Voltage Graph After Cleaning Module 1.2

Stellenbosch University https://scholar.sun.ac.za

6.5.1.3 Shading Experiment

An experiment was conducted on the PV test site to investigate the influence of shading on PV modules within a string. The shading experiment was conducted on a sunny day between 11 am and 12 am on 14 November 2018. Twelve different scenarios were investigated, a scenario every 5 minutes. The twelve scenarios were as follow:

1. Module 1.1 30% of module shaded 100% - horizontally
2. Module 1.1 50% of module shaded 100% - horizontally
3. Module 1.1 60% of module shaded 100% - horizontally
4. Module 1.1 100% shaded
5. Module 1.1 30% of module shaded 100% - vertically
6. Module 1.1 60% of module shaded 100% - vertically
7. No shade on any module
8. Module 1.1 shaded with 80% shade cloth
9. Module 1.1 - 1.2 shaded with 80% shade cloth
10. Module 1.1 - 1.3 shaded with 80% shade cloth
11. Module 1.1 - 1.4 shaded with 80% shade cloth
12. No shade on any module

The voltage graph for sensor nodes 1.1 to 1.5 for the duration of the shading experiment is shown in Figure 6.36.

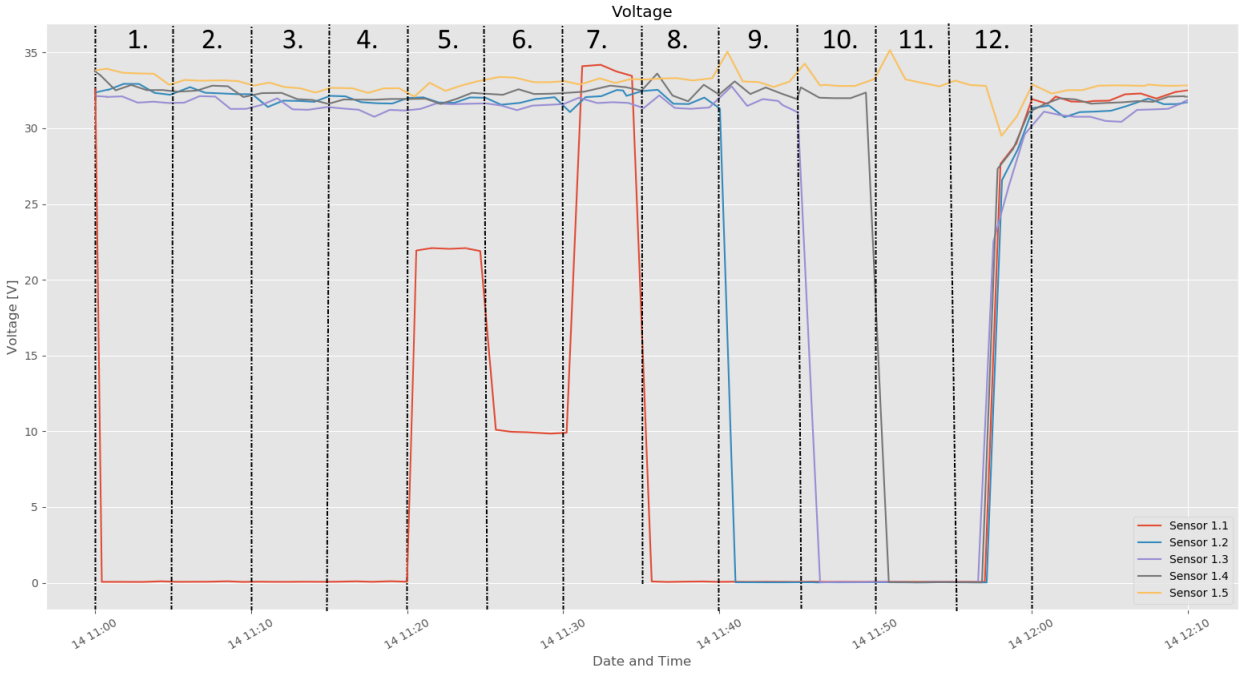

Figure 6.36: PV Plant Shading Experiment - Voltage

Stellenbosch University https://scholar.sun.ac.za

Shading scenarios 1 to 4 is shown in Figure 6.37.

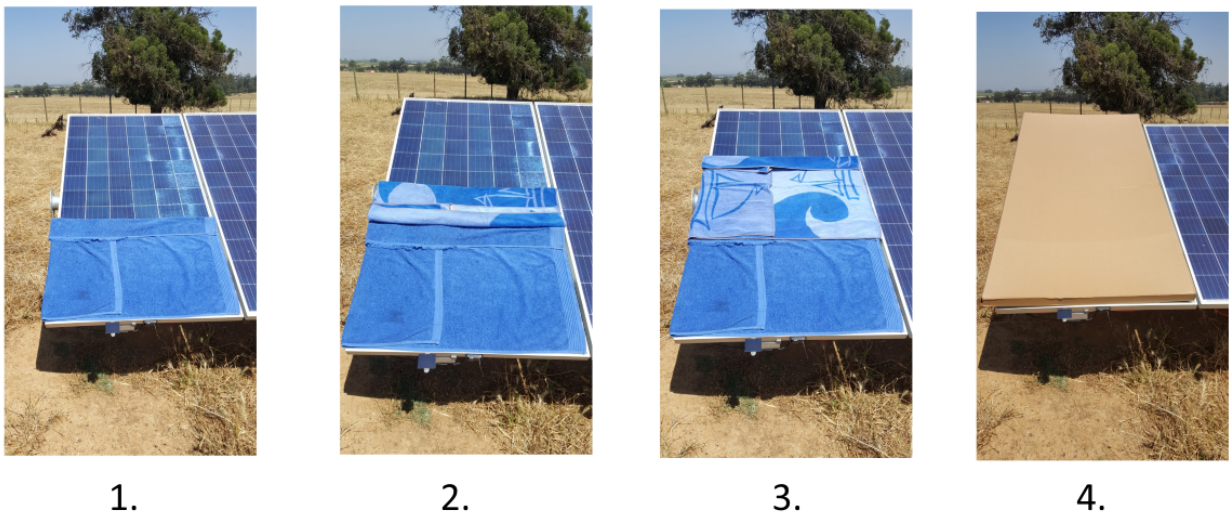

Figure 6.37: Shading Experiment Scenarios 1 - 4

When there is horizontal shading present on PV module 1.1 (scenario 1 - 3) the voltage is almost zero. This is because the bypass diodes on the PV module is activated when shade appears over a certain area covered by the specific diode. Any horizontal shade covers area allocated to all 3 of the bypass diodes resulting in a voltage of almost 0 V.

Shading scenarios 5 and 6 is shown in Figure 6.37.

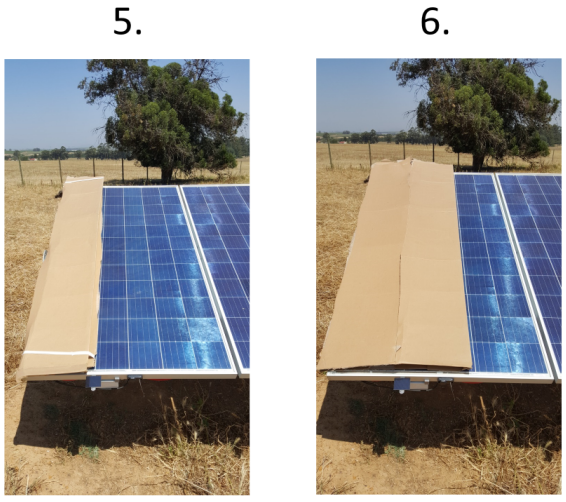

Figure 6.38: Shading Experiment Scenarios 5 - 6

In the case of vertical shading (scenario 5 and 6) the effect of the bypass diode can clearly be observed. The voltage of the PV module around 60% for a 30% shading (scenario 5) and around 30% for a 60% shading. The bypass diode allows the PV module to produce power in the parts where there is no shading present.

Shading scenarios 8 to 11 is shown in Figure 6.37.

Stellenbosch University https://scholar.sun.ac.za

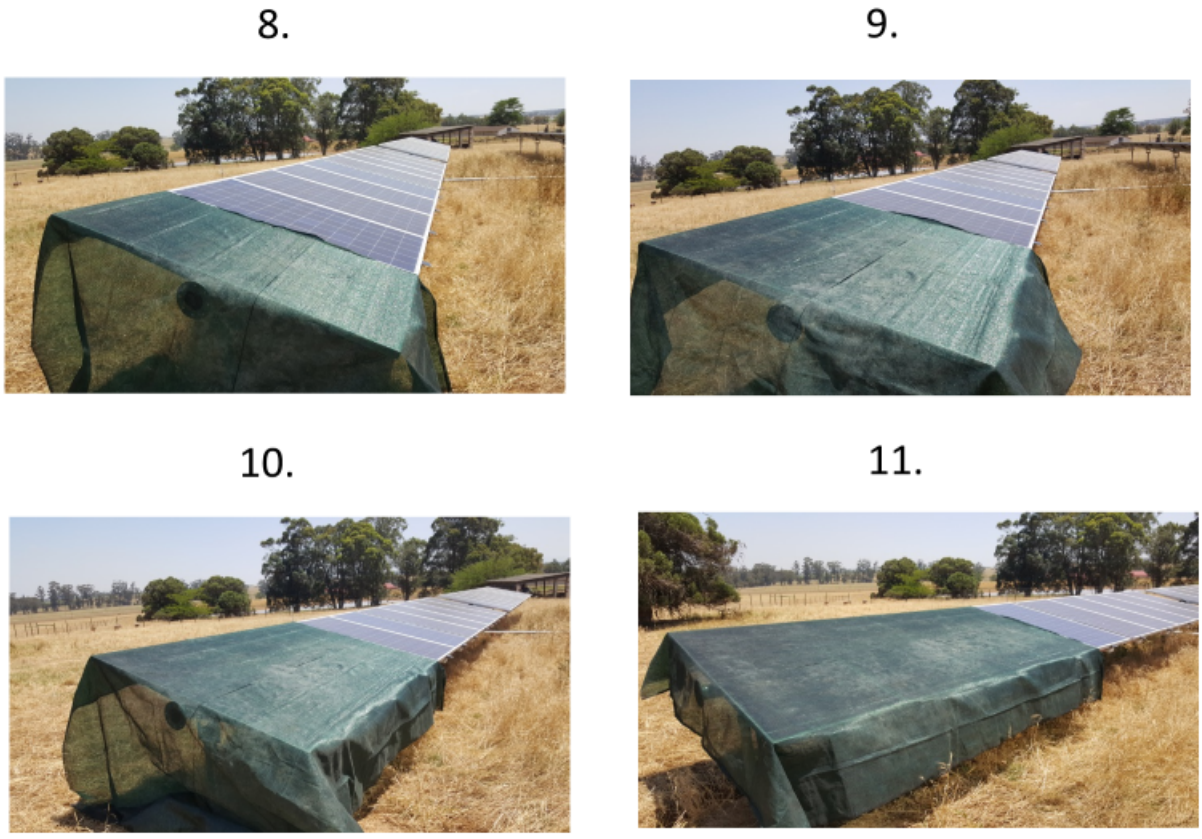

Figure 6.39: Shading Experiment Scenarios 8 - 11

For scenarios 8 to 11 the voltage of the PV modules being covered by the 80% shade cloth is almost 0 V. This is due to the fact that a 80% shade cloth directly on a a PV module blocks more than 80% of the light since no diffuse light is passed through the cloth. When shading is removed (scenario 12) the PV module voltages return to their respective normal operating values.

Stellenbosch University https://scholar.sun.ac.za

Chapter 7

Conclusions and Recommendations

7.1 Chapter overview

In this chapter the objectives that were set out in Section 1.2 are evaluated. The various objectives are evaluated in terms of the functional requirements presented in Section 3.2. Evaluations are based on results presented in Chapter 6. Recommendations for each of the objectives are also presented. Finally, a brief summary of the future work that is planned, based on the results and recommendations of this project, is given.

7.2 Conclusions

The various objectives that were set out in Section 1.2 that were achieved according to requirements set out in Section 3.2 are presented.

7.2.1 Measurement

Three sensor node versions that measure environmental and electrical properties that relate to module performance were developed and tested. The third and final sensor node version, referred to as Version 3, measures voltage, current, irradiance, ambient temperature, module temperature, orientation and tampering detection. The sensor node measures these parameters with adequate accuracy to evaluate module performance in detail as presented with different field trial scenarios in Section 6.3. The sensor node is modular, plug-and-play, self-powered and low maintenance (no need for battery replacements).

7.2.2 Data Collection

A data collection device (gateway) was developed. The gateway receives measurement data from a number of sensor nodes, adds a date and time stamp to each incoming dataset and stores the data into a database located on a cloud server. The data-transport method used between the sensor nodes and the central gateway is a LPWAN LoRa which has a low power usage with adequate data rates and a long range. Range tests presented in Section 6.4 indicate successful packet delivery at a distance of 4.21 km in an urban area. The wireless communication technology thus has an adequate range for operating on a small, medium or large solar installation.

Stellenbosch University https://scholar.sun.ac.za

7.2.3 Modelling

A fault detection model was developed and implemented within a GUI application. The model calculates the estimated and measured efficiency for each set of measurements from the sensor nodes. The model then assigns a health status to each measured PV module accordingly. The health status assignment values are presented in Table 6.2.

7.2.4 Data Visualization

A GUI application was developed to visualise measured and analysed data. The GUI consists of a layout and a graph view. The layout view displays 'live' plant information which is updated every 10 seconds. Information shown include the health, voltage, wattage and temperature of each PV module, general string information and status messages as presented in Figure 6.26. The graph view is used to view historical measurement and analysed data. The sensor node number, performance quantity and time frame of data that need to be displayed in a graph can be selected by the user.

7.2.5 Remote Detection and Reporting

The GUI application retrieves the measurement data that it analyses and displays from the database located on a cloud server. This database can be accessed from any computer with an Internet connection. The GUI application can thus run on any computer that has an Internet connection. The GUI application reports certain events related to module and/or sensor malfunction. These events include: detected tampering, low battery warning, lost connection and critical faults on PV modules. The monitoring system is thus capable of remote fault detection and reporting via the GUI application.

7.3 Recommendations

Observations and recommendations for future work is described in this section. Further, problems that were encountered during the course of the project is described and possible solutions are provided.

7.3.1 Measurement

Each sensor node that was developed measures all of the electrical an environmental quantities related to module performance. This results in a number of quantities that have similar values for certain set-ups which, in turn results in repetitive data being measured and sent. In a string set-up the same current flows through each sensor. There is thus no need to measure the current in a string on more than one sensor. The ideal would be to have one main sensor per string measuring all of the electrical and environmental quantities and to have other sensors in the same string only measuring voltage and module temperature. This sort of configuration will significantly reduce the overall cost of the monitoring-system.

Other scenarios might also be exploited, for instance measuring only voltage and module temperature. These are the two main parameters that differ from module-to-module. Depending on the PV plant other parameters such as string current, irradiance and ambient temperature can then be obtained from the inverters and weather measurement stations present on most big PV installations.

Stellenbosch University https://scholar.sun.ac.za

7.3.2 Data Collection

Although the gateway successfully received and stored measurement data in a database on a cloud server, issues arouse when Internet connectivity was momentarily lost. Methods to mitigate this issue can be investigated to ensure continuous operation of the monitoring system. It is recommended to implement local storage where measurement data can be stored when Internet connectivity is lost. The data can then be published in the cloud database once Internet connectivity is restored.

7.3.3 Modelling

Although the current fault detection model was able to detect faults and inefficiencies accurately other simpler models might be investigated. It was found that the voltage of a faulty module was significantly lower than surrounding, healthy modules. By simply measuring and investigating the voltages of different PV modules in a plant the entire monitoring system might be much simpler and more cost-effective.

7.3.4 Data Visualization

The GUI application that displayed plant data executes in the Python Programming environment. This limits the GUI to run on computers with the environment installed. A web-based application that can run in any browser (be it a PC, tablet or smart phone) could be investigated.

7.3.5 Remote Detection and Reporting

Developing a web-based application would increase the remote detection and reporting capabilities of the monitoring system. A dedicated call and/or response centre that can deal with certain events and faults when they occur can also be considered. When a fault occurs it is important to send the appropriate parties to remedy the situation speedily and effectively.

7.4 Future Work

There are future plans for a large-scale deployment of the sensor nodes developed in this project. The aim of the large-scale deployment focusses on monitoring the module temperatures of a vast amount of PV modules within an utility-scale solar PV plant.

The main purpose of the temperature data is to assist a PHD study which focusses on creating an accurate short-term forecasting model for a PV plant using machine-learning techniques. The study aims to create a temperature map of a PV plant - thus requiring detailed module-level temperature measurements.

There are other future application plans for the monitoring system: for instance a research topic that investigates different PV module technologies. The monitoring system developed can provide detailed module-level measurements in different test scenarios that can be used to evaluate different PV technologies and/or configurations.

The world-wide tendency towards so-called green energy, will lead to the further development of renewable energy sources. The importance of solar energy will continue to grow and expand to become, eventually, the major source of electrical energy for cities and countries. In the future, PV plants (solar farms) will play an increasing role in this scenario. It will be of the utmost importance that these establishments be run in the most cost-effective way.

Stellenbosch University https://scholar.sun.ac.za

Determining the health of individual modules and larger strings will be essential in reaching this goal. Without adequate monitoring, the maintenance of modules, strings and utility-sized plants will be almost impossible, requiring an inordinate amount of man-hours to check individual modules one by one.

The research contained in this paper confirms that remote monitoring is not only possible, but it also follows that this type of monitoring will be absolutely essential in the future of renewable energy. In fact, there is no reason why this monitoring system can not be adapted to other forms of renewable energy. Wind farms and smaller hydro-electrical plants may also be targeted to increase efficiency.

The work contained in this thesis may very well be the first, tentative, steps in an entirely new concept of how solar energy plants will be maintained in the future.

Stellenbosch University https://scholar.sun.ac.za

Appendices

Stellenbosch University https://scholar.sun.ac.za

Appendix A

Sensor Node Version 2 Enclosure Design Drawing

Stellenbosch University https://scholar.sun.ac.za

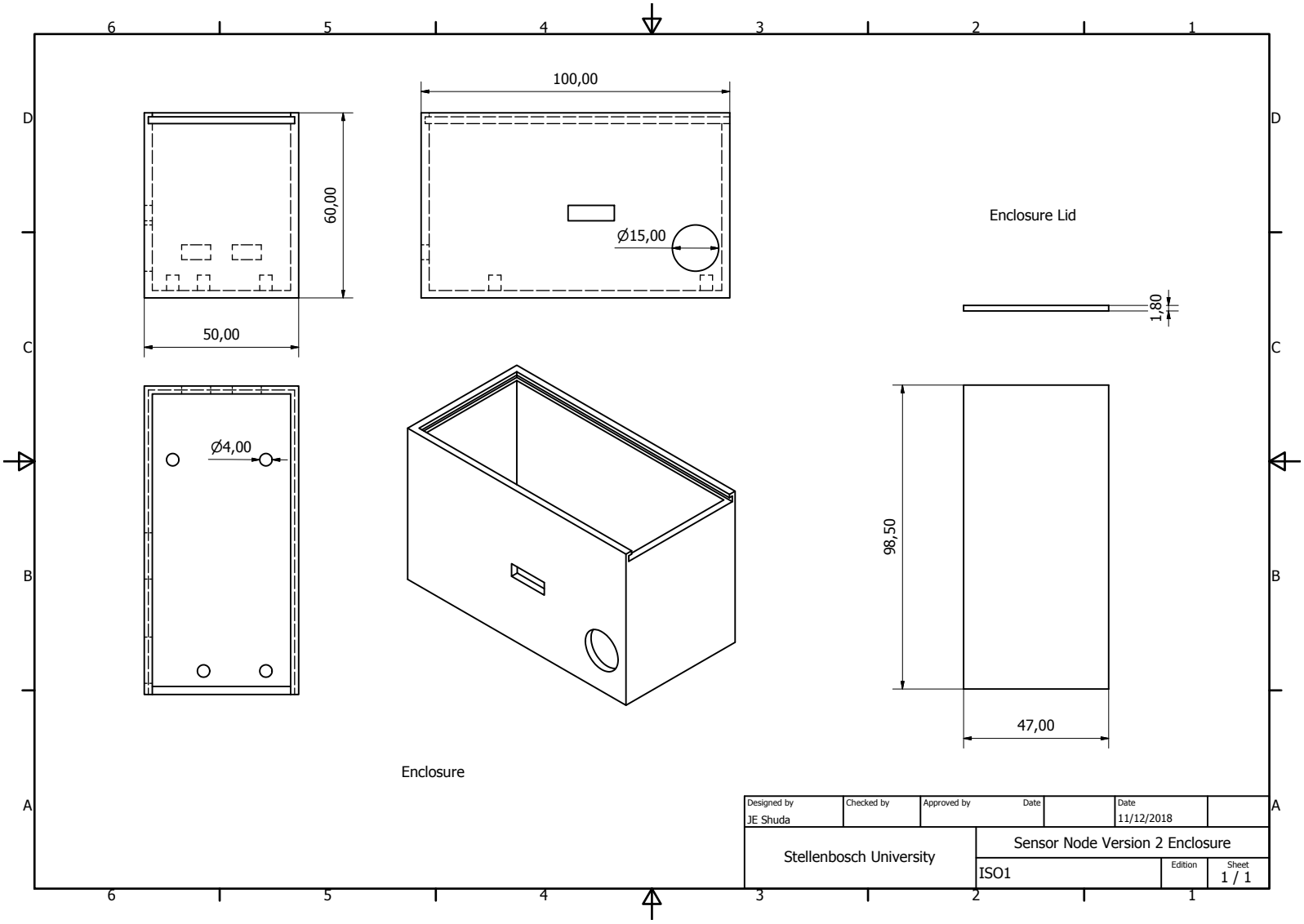

Figure A.1: Sensor Node Version 2 Enclosure Design Drawing

Stellenbosch University https://scholar.sun.ac.za

Appendix B

Sensor Node Version 2 and 3 Enclosure Brackets Design Drawing

Stellenbosch University https://scholar.sun.ac.za

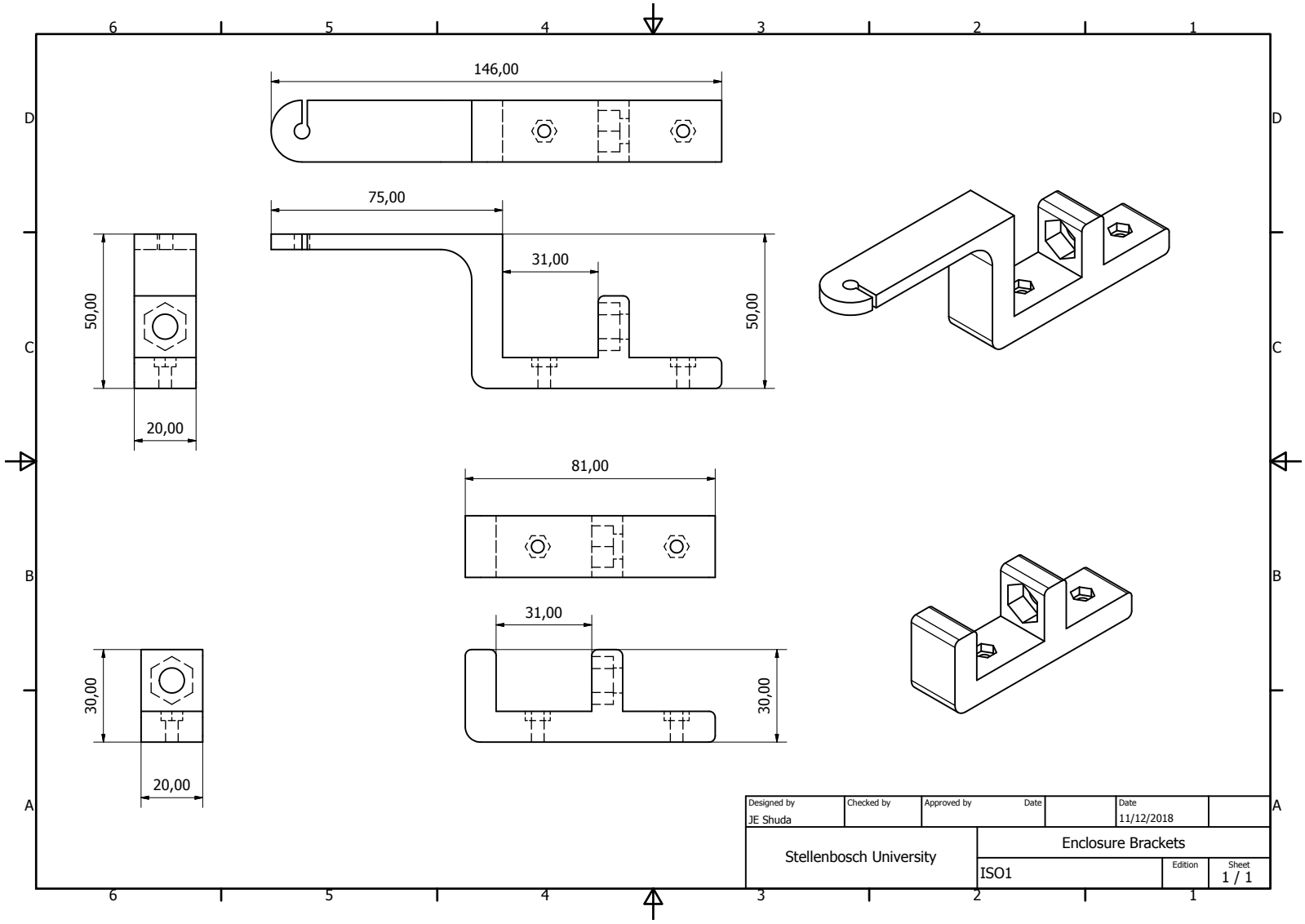

Figure B.1: Sensor Node Version 2 and 3 Enclosure Brackets Design Drawing

Stellenbosch University https://scholar.sun.ac.za

Appendix C

Sensor Node Version 3 Schematic Design

Stellenbosch University https://scholar.sun.ac.za

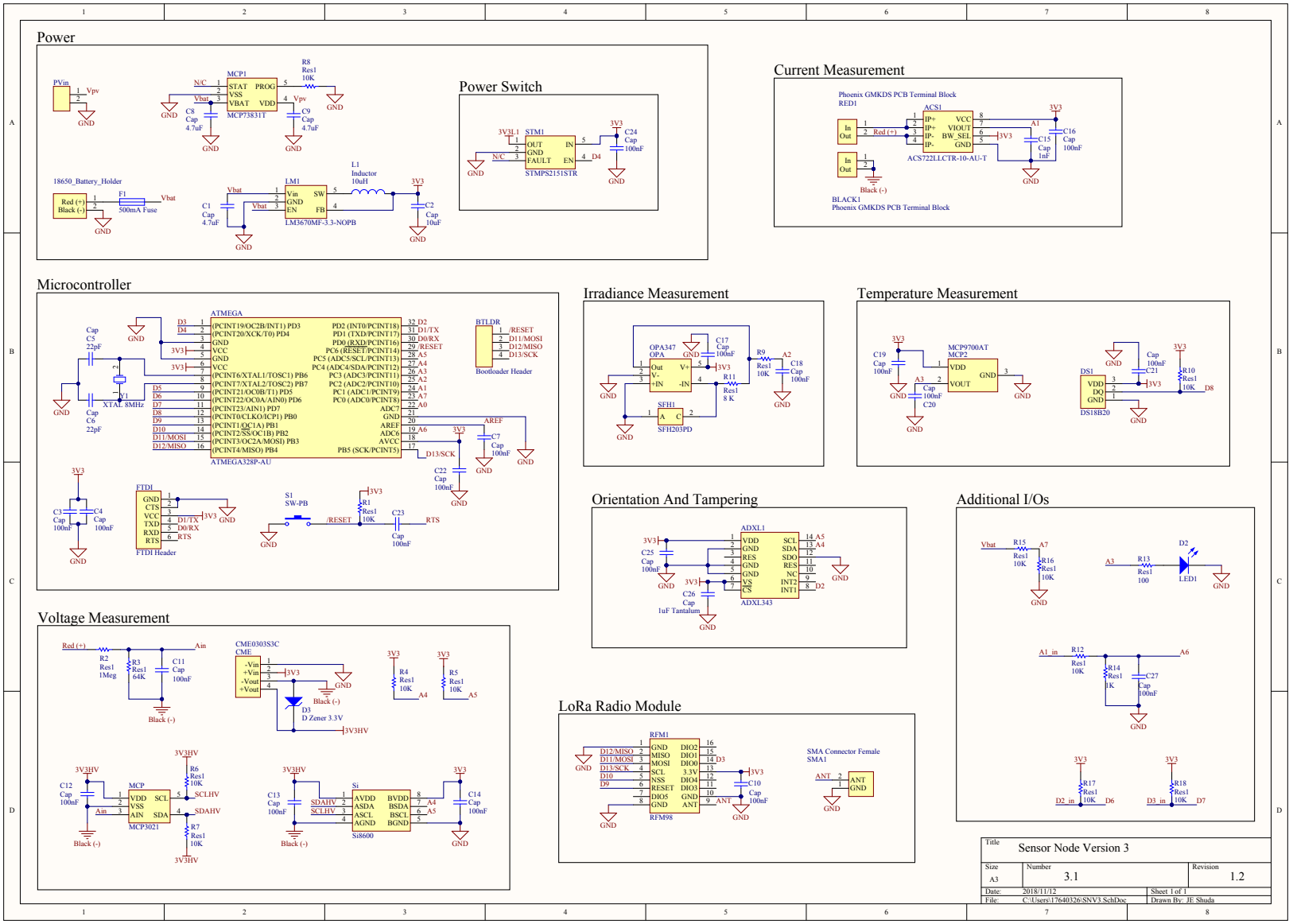

Figure C.1: Sensor Node Version 3 Schematic Design

Stellenbosch University https://scholar.sun.ac.za

Bibliography

[1] "Solar industry growing at a record pace." [Online]. Available: http://www.seia.org/research-resources/solar-industry-data

[2] C. Ranhotigamage and S. C. Mukhopadhyay, "Field trials and performance monitoring of distributed solar panels using a low-cost wireless sensors network for domestic applications," *IEEE Sensors Journal*, vol. 11, no. 10, pp. 2583–2590, Oct 2011.

[3] Syafii, M. I. Rusydi, R. Putra, and M. H. Putra, "Real-time measurement of grid connected solar panels based on wireless sensors network," in *2016 International Conference on Sustainable Energy Engineering and Application (ICSEEA)*, Oct 2016, pp. 95–99.

[4] Y. Rashidi, M. Moallem, and S. Vojdani, "Wireless zigbee system for perormance monitoring of photovoltaic panels," in *2011 37th IEEE Photovoltaic Specialists Conference*, June 2011, pp. 003 205–003 207.

[5] B. Ando, S. Baglio, A. Pistorio, G. M. Tina, and C. Ventura, "Sentinella: Smart monitoring of photovoltaic systems at panel level," *IEEE Transactions on Instrumentation and Measurement*, vol. 64, no. 8, pp. 2188–2199, Aug 2015.

[6] ——, "Sentinella: A wsn for a smart monitoring of pv systems at module level," in *2013 IEEE International Workshop on Measurements Networking (M N)*, Oct 2013, pp. 36–40.

[7] "Enphase microinverters." [Online]. Available: https://enphase.com/en-us/products-and-services/microinverters

[8] M. A. Maehlum. (2018, August) Micro-inverters vs. central inverters. [Online; posted 5-August-2017]. [Online]. Available: http://energyinformative.org/are-solar-micro-inverters-better-than-central-inverters/

[9] "Power optimizer module add-on." [Online]. Available: https://www.solaredge.com/products/power-optimizer/

[10] "Ts4-b (integrated jbox)." [Online]. Available: https://www.tigoenergy.com/products/

[11] N. M. A. A. Shannan, N. Z. Yahaya, and B. Singh, "Single-diode model and two-diode model of pv modules: A comparison," in *2013 IEEE International Conference on Control System, Computing and Engineering*, Nov 2013, pp. 210–214.

[12] S. McFadyen. (2018, August) Photovoltaic (pv) panel - performance modelling. [Online; posted 8-January-2015]. [Online]. Available: https://myelectrical.com/notes/entryid/257/photovoltaic-pv-panel-performance-modelling

[13] "Voltage measurement." [Online]. Available: https://www.re-innovation.co.uk/docs/voltage-measurement/

[14] M. A. Maehlum. (2018, August) Which solar panel type is best? mono- vs. polycrystalline vs. thin film. [Online; posted 16-May-2018]. [Online]. Available: http://energyinformative.org/best-solar-panel-monocrystalline-polycrystalline-thin-film/

Stellenbosch University https://scholar.sun.ac.za

[15] "Hall effect sensor." [Online]. Available: https://www.electronics-tutorials.ws/electromagnetism/hall-effect.html

[16] "Optocoupler tutorial." [Online]. Available: https://www.electronics-tutorials.ws/blog/optocoupler.html

[17] V. Semiconductors, "Linear optocoupler, high gain stability, wide bandwidth," Datasheet, Mar 2018. [Online]. Available: http://www.vishay.com/docs/83622/il300.pdf

[18] "Light sensors." [Online]. Available: https://www.electronics-tutorials.ws/io/io_4.html

[19] D. Brooks. (2018, June) Measuring sunlight at earth's surface: Build your own pyranometer. [Online; posted February-2007]. [Online]. Available: http://www.instesre.org/construction/pyranometer/pyranometer.htm

[20] R. Singh and S. Dewra, "Performance evaluation of star, tree amp; mesh optical network topologies using optimized raman - edfa hybrid optical amplifier," in *2015 International Conference on Trends in Automation, Communications and Computing Technology (I-TACT-15)*, Dec 2015, pp. 1–6.

[21] "Link budget calculation." [Online]. Available: https://www.slideshare.net/sitimunirah88/link-budget-calculation

[22] "Free space path loss: details and calculator." [Online]. Available: https://www.electronics-notes.com/articles/antennas-propagation/propagation-overview/free-space-path-loss.php

[23] J. F. Ensworth and M. S. Reynolds, "Ble-backscatter: Ultralow-power iot nodes compatible with bluetooth 4.0 low energy (ble) smartphones and tablets," *IEEE Transactions on Microwave Theory and Techniques*, vol. 65, no. 9, pp. 3360–3368, Sept 2017.

[24] M. Idoudi, H. Elkhorchani, and K. Grayaa, "Performance evaluation of wireless sensor networks based on zigbee technology in smart home," in *2013 International Conference on Electrical Engineering and Software Applications*, March 2013, pp. 1–4.

[25] R. Ruslan, A. H. M. Nor, R. Saian, M. H. Omar, and M. Manaf, "Performance evaluation of wi-fi and white-fi: Simulation approach," in *2016 UKSim-AMSS 18th International Conference on Computer Modelling and Simulation (UKSim)*, April 2016, pp. 343–346.

[26] M. Lauridsen, H. Nguyen, B. Vejlgaard, I. Z. Kovacs, P. Mogensen, and M. Sorensen, "Coverage comparison of gprs, nb-iot, lora, and sigfox in a 7800 square km area," in *2017 IEEE 85th Vehicular Technology Conference (VTC Spring)*, June 2017, pp. 1–5.

[27] "11 internet of things (iot) protocols." [Online]. Available: https://www.rs-online.com/designspark/eleven-internet-of-things-iot-protocols-you-need-to-know-about

[28] H. Mroue, A. Nasser, S. Hamrioui, B. Parrein, E. Motta-Cruz, and G. Rouyer, "Mac layer-based evaluation of iot technologies: Lora, sigfox and nb-iot," in *2018 IEEE Middle East and North Africa Communications Conference (MENACOMM)*, April 2018, pp. 1–5.

[29] A. J. Wixted, P. Kinnaird, H. Larijani, A. Tait, A. Ahmadinia, and N. Strachan, "Evaluation of lora and lorawan for wireless sensor networks," in *2016 IEEE SENSORS*, Oct 2016, pp. 1–3.

[30] D. Yim, J. Chung, Y. Cho, H. Song, D. Jin, S. Kim, S. Ko, A. Smith, and A. Riegsecker, "An experimental lora performance evaluation in tree farm," in *2018 IEEE Sensors Applications Symposium (SAS)*, March 2018, pp. 1–6.

Stellenbosch University https://scholar.sun.ac.za

[31] H. Lee and K. Ke, "Monitoring of large-area iot sensors using a lora wireless mesh network system: Design and evaluation," *IEEE Transactions on Instrumentation and Measurement*, vol. 67, no. 9, pp. 2177–2187, Sept 2018.

[32] P. Contacct, "Pcb terminal block - gmkds 3/ 2-7,62 - 1731721," Datasheet, Nov 2014. [Online]. Available: https://www.phoenixcontact.com/us/products/1731721

[33] M. P. Solution, "Isolated 3w 4:1 input single output dc-dc converters," Datasheet, 2015. [Online]. Available: https://www.murata-ps.com/datasheet?/data/power/ncl/kdc_ncs3.pdf

[34] Farnell, "Arduino nano," Datasheet, 2014. [Online]. Available: http://www.farnell.com/datasheets/1682238.pdf

[35] D. A. Technologies, "Drf1278f 20dbm lora long range rf front-end module," Datasheet, Aug 2015. [Online]. Available: http://www.dorji.com/docs/data/DRF1278F.pdf

[36] O. Semiconductor, "200 ma, ultra low noise, high psrr, bicmos rf ldo regulator," Datasheet, Apr 2013. [Online]. Available: http://onsemi.com

[37] A. by Linx, "Ant-433-pw-qw-xxx," Datasheet, Jan 2015. [Online]. Available: https://linxtechnologies.com/wp/wp-content/uploads/ant-433-pw-qw.pdf

[38] B.-B. P. from Texas Instruments, "micropower, rail-to-rail operational amplifiers," Datasheet, Jul 2007. [Online]. Available: http://www.ti.com/lit/ds/symlink/opa2347.pdf

[39] M. P. Solution, "Isolated 1w single output isolated dc-dc converters," Datasheet, 2015. [Online]. Available: https://power.murata.com/data/power/ncl/kdc_cre1.pdf

[40] A. MicroSystems, "Fully integrated, hall effect-based linear current sensor ic with 2.1 kvrms isolation and a low-resistance current conductor," Datasheet, Jun 2017. [Online]. Available: http://www.allegromicro.com/~/media/Files/Datasheets/ACS712-Datasheet.ashx

[41] O. O. Semiconductors, "Silicon pin photodiode," Datasheet, Dec 2015. [Online]. Available: https://dammedia.osram.info/media/resource/hires/osram-dam-2496046/SFH%20203%20P.pdf

[42] T. Instruments, "Lm35 precision centigrade temperature sensors," Datasheet, Dec 2017. [Online]. Available: http://www.ti.com/lit/ds/symlink/lm35.pdf

[43] M. Integrated, "Programmable resolution 1-wire digital thermometer," Datasheet, Jan 2015. [Online]. Available: https://datasheets.maximintegrated.com/en/ds/DS18B20.pdf

[44] F. Semiconductor, "3-axis orientation/motion detection sensor," Datasheet, Mar 2012. [Online]. Available: https://media.digikey.com/pdf/Data%20Sheets/NXP%20PDFs/MMA7660FC.pdf

[45] Kipp and Zonen, "Cmp11 pyranometer," Datasheet, 2018. [Online]. Available: http://www.kippzonen.com/Product/13/CMP11-Pyranometer

[46] T. Instruments, "Lm3670 miniature step-down dc-dc converter for ultralow voltage circuits," Datasheet, Feb 2016. [Online]. Available: http://www.ti.com/lit/ds/symlink/lm3670.pdf

[47] S. T. Co, "0.5w solar panel 55*70," Datasheet, Mar 2014. [Online]. Available: https://media.digikey.com/pdf/Data%20Sheets/Seeed%20Technology/0.5w_Solar_Panel_55_70_Web.pdf

[48] Bourns, "Srr0745a series - shielded power inductors," Datasheet, May 2017. [Online]. Available: https://www.bourns.com/docs/Product-Datasheets/SRR0745A.pdf

[49] M. Technology, "8-bit avr microcontrollers, atmega328/p," Datasheet, Nov 2016. [Online]. Available: http://ww1.microchip.com/downloads/en/DeviceDoc/Atmel-42735-8-bit-AVR-Microcontroller-ATmega328-328P_Datasheet.pdf

Stellenbosch University https://scholar.sun.ac.za

[50] H. Electronic, "Rfm95/96/97/98 - low power long range tranceiver module v1.0," Datasheet, 2016. [Online]. Available: https://github.com/SeeedDocument/RFM95-98_LoRa_Module/blob/master/RFM95_96_97_98_DataSheet.pdf

[51] M. P. Solutions, "Cme series, isolated 0.75w single output isolated dc-dc converters," Datasheet, 2015. [Online]. Available: https://power.murata.com/data/power/ncl/kdc_cme.pdf

[52] M. Technology, "Low-power 10-bit a/d converter with i2c interface," Datasheet, 2017. [Online]. Available: http://ww1.microchip.com/downloads/en/DeviceDoc/20001805C.pdf

[53] S. Labs, "Bidirectional i2c isolators with unidirectional digital channels," Datasheet, Jan 2018. [Online]. Available: https://www.silabs.com/documents/public/data-sheets/Si860x.pdf

[54] A. MicroSystems, "High accuracy, galvanically isolated current sensor ic with small footprint soic8 package," Datasheet, Apr 2015. [Online]. Available: http://www.allegromicro.com/~/media/Files/Datasheets/ACS722-Datasheet.pdf

[55] M. Technology, "Low-power linear active thermistor ics," Datasheet, Jun 2016. [Online]. Available: http://ww1.microchip.com/downloads/en/DeviceDoc/20001942G.pdf

[56] ——, "Miniature single-cell, fully integrated li-ion, li-polymer charge management controllers," Datasheet, Jul 2014. [Online]. Available: http://ww1.microchip.com/downloads/en/DeviceDoc/20001984g.pdf

[57] STMicroelectronics, "Enhanced single channel power switches," Datasheet, Jan 2013. [Online]. Available: https://www.st.com/content/ccc/resource/technical/document/datasheet/e8/d7/48/25/eb/87/45/b3/CD00167470.pdf/files/CD00167470.pdf/jcr:content/translations/en.CD00167470.pdf

[58] A. Devices, "Digital mems accelerometer," Datasheet, Apr 2012. [Online]. Available: http://www.analog.com/media/en/technical-documentation/data-sheets/ADXL343.pdf

[59] I. C. A. of South Africa, "The radio frequency spectrum regulations 2015," Government Gazette, Mar 2015.